scientific reports

Check for updates

OPEN

Data-driven optimisation of sustainable high-performance concrete incorporating SCMs, biomass ash, and graphene nanoplatelets

Pradyut Anand[1,2], Surya Dev Singh[3], Suresh Pratap[4]✉, Perumal Asaithambi[5] & Firomsa Bidira[6]✉

The current study outlines an integrated experimental and data-driven methodology of the development of sustainable high-performance concrete, using a hybrid low-carbon binder, which includes fly ash (FA), ground granulated blast-furnace slag (GGBS), thermally treated coir biomass (TTCB) and graphene nanoplatelets (GNPs). M40 grade concrete mixtures were prepared by systematic variation of supplementary cementitious materials (SCMs, 30% of the total binder), TTCB (5% to 10%) and GNPs dosage (0.08% to 0.12%). Mechanical properties were evaluated at 7 and 28 days, rapid chloride permeability (RCPT), water uptake and residual strength after exposure to 300 °C. The optimised mix delivered a compressive strength of 55 MPa at 28 days, which is approximately 23% greater than the control mix (44–45 MPa at 28 days), and chloride permeability 505 C (42% lower) and water absorption 2.8% (40% lower), respectively. Retention of strength following exposure to 300 °C was above 80%, which means that the thermal stability was improved. Microstructural examinations confirmed refined pore structure, lower content of portlandite and enhanced interfacial bonding. The 60 experimental observations based on replicated specimens in 10 mix designs were trained on Random Forest, XGBoost and CNN LSTM models. XGBoost had the best predictive accuracy ($R^2 > 0.95$ to predict strength), and the permutation-importance analysis revealed TTCB content and SCMs balance to be the most important predictors. Multi-objective optimisation (NSGA-II and MOEA/D) was used to produce trade-offs between strength, durability, embodied CO_2 and cost within the constrained experimental space. The suggested surrogate-assisted optimisation model offers a repeatable approach to eco-efficient concrete mix design at limited laboratory conditions.

Keywords Sustainable concrete, Flyash, GGBS, Thermally treated coir biomass, Graphene nanoplatelets, Machine learning

Concrete remains an essential element of the world's infrastructure, but it has a significant negative impact on the environment. Ordinary Portland cement (OPC), the dominant binder in concrete, is a major contributor to CO_2 emissions in the world due to the energy-intensive process of clinker production[1,2]. In order to reduce this effect, the use of supplementary cementitious materials (SCMs) like fly ash (FA) and ground granulated blast-furnace slag (GGBS) has become widely used[3–5]. The embodied carbon is minimised by partial replacement of OPC by SCMs, and in most cases, the long-term durability is enhanced. However, the use of single-SCM systems

[1]Department of Civil Engineering, School of Engineering and Technology, Noida International University, Greater Noida, Uttar Pradesh, India 201312. [2]Department of Civil Engineering, Graphic Era (Deemed to be University), Dehradun 248002, India. [3]School of Construction, National Institute of Construction Management and Research (NICMAR) University, Balewadi, Pune, Maharashtra 411045, India. [4]Department of Mechanical Engineering, G.L. Bajaj Institute of Technology and Management, Greater Noida, UP 201306, India. [5]Department of Biotechnology and Chemical Engineering, School of Engineering, Faculty of Science, Technology and Architecture, Manipal University Jaipur, Jaipur, Rajasthan 303007, India. [6]Faculty of Civil and Environmental Engineering, Jimma Institute of Technology, Jimma University, Po Box - 378, Jimma, Ethiopia. ✉email: sureshpratap@yahoo.com; firomsa.bidira@ju.edu.et

presents intrinsic constraints; high fly-ash levels may slow down the initial development of strength, and the effects of single additives are likely to level off at high dosage levels[5–7]. Binary and ternary blends have driven the innovations in sustainable concrete technology, but it is still difficult to achieve a substantial decrease in clinker and maintain the mechanical integrity and durability[6,8–10]. A promising strategy is the use of multi-component systems that combine materials on the nano-, micro-, and meso-scales[11–13]. At the same time, the traditional mix design approaches are predominantly empirical and trial and error, which highlights the need to develop data-driven approaches that would help accelerate sustainable binder optimisation.

The current work suggests a hybrid binder, which incorporates industrial by-products (FA and GGBS), thermally treated coir biomass (TTCB), and graphene nanoplatelets (GNPs)[14–18] in accordance with the carbon–neutral and circular economy principles[14–16]. Introduced in low doses (0.05–0.30 wt%), GNPs may facilitate nucleation, crack-bridging, and densification of the matrix, depending on good dispersion[19,20]; but agglomeration often inhibits these effects. The underutilised resources include agricultural residues, such as coconut coir. Thermal treatment of coir under controlled conditions converts coir to silica-containing ash with pozzolanic potential[21–23]. Besides acting as a reactive SCM, TTCB can be used as a micro-scale filler and a dispersive matrix of nanoparticles[24–26]; the porous, carbonaceous biomass can help reduce the restacking of graphene and enhance nanoscale dispersion. The FA-GGBS-TTCB-GNP system thus operates at various length scales. FA and GGBS improve the pore structure and increase long-term hydration[27,28]. TTCB provides reactive silica and micro-filling effects, which may be useful in dispersing nanoparticles[26,29,30]. GNPs enhance the matrix on a nanoscale level through nucleation enhancement and crack-bridging processes. Even though the research on nanomaterials, bio-ashes, or SCM blends was done in the past, the combination of all four elements in a single optimisation strategy has not been examined thoroughly[6,31,32]. In the materials science field, the coupled hydration kinetics, secondary pozzolanic reactions, and development of interfacial nanostructures determine the performance of the FA, GGBS, TTCB, and GNPs composite system. The aluminosilicate precursors provided by FA and GGBS react with calcium hydroxide to produce additional C–S–H and C–A–S–H phases, which refine the capillary pore network and reduce ionic transportation pathways. High-content amorphous silica TTCB also takes part in pozzolanic reactions and serves as a micro-filler, which enhances the packing density of particles. On a nanoscale, GNPs serve as heterogeneous nucleation sites, which increase early hydration kinetics and promote the development of denser C–S–H structures. Well-dispersed GNPs may fill microcracks and increase stress transfer across the interfacial transition zone (ITZ). Thus, the synergistic performance is not only due to the substitution by supplementary cementitious material (SCM), but also multiscale couplings between hydration chemistry, pore refinement, nanoparticle dispersion stability, and crack-bridging mechanics. The methodological advances of artificial intelligence use in construction materials in the recent past have highlighted the growing opportunities of machine learning in predicting and optimising concrete performance. Empirical studies with waste glass powder (GGP/WGP)-based concretes have found that the ensemble learning methods, such as support vector regression, gradient boosting, XGBoost, LightGBM, and CatBoost, can achieve high predictive accuracy ($R^2 > 0.94$) when trained on carefully curated experimental data, with curing age and water-cement ratio reliably coming up as the most important predictors using SHAP-based interpretability analyses[33–36]. Similar studies on graphene nanoplatelet-modified cementitious systems have applied decision-tree algorithms, CatBoost, adaptive neuro-fuzzy inference systems (ANFIS), and LightGBM, and the results have shown that nano-scale geometric descriptors and curing age have a strong effect on the prediction of compressive strength[37]. All of these studies support the effectiveness of ensemble and boosting algorithms in the process of non-linear interactions within sustainable composite systems. The significance of curing regimes and microstructural evolution to the achievement of optimum performance has been stressed by parallel experimental studies of fly ash -ground-granulated blast-furnace slag (FA -GGBS)-based geopolymer recycled aggregate concretes, and the importance of time-dependent pore refinement and shrinkage behaviour as important determinants of durability has been highlighted by analyses of supplementary cementitious material-blended systems[38,39].

However, the research that is available is mostly focused on single waste streams (e.g. glass or graphene), single performance measures (mostly compressive strength), or single predictive modelling, commonly lacking a multi-objective sustainability optimisation framework. Moreover, few studies have simultaneously used bio-derived pozzolans, industrial SCMs, and nanomaterials in a single experimental-modelling-optimisation paradigm. The current study aims at filling this gap by experimentally demonstrating a multi-component FA-GGBS-TTCB-GNP system and integrating interpretable surrogate modelling in a constrained multi-objective optimisation approach.

Research gap and motivation

Although there has been an advancement in low-carbon concrete technologies, there are still a number of gaps in knowledge. To begin with, bio-derived ashes have been rarely explored as both reactive SCMs and nano-dispersion facilitators[40–45]. Second, most of the optimisation tools used are empirical in nature and therefore offer little information on how to trade off competing goals, such as compressive strength, durability, cost of production, and embodied carbon[46–49]. Third, sustainable concrete research has not yet applied machine-learning methods to address the issue of predictive modelling, without directly considering the limitations of datasets, model interpretability, and experimental validation[50–56]. This necessitates an overall framework that combines experimental verification, mechanistic understanding, interpretable machine-learning methods, and multi-objective optimisation in a strictly defined design space. In the current study, multi-scale refers to the interactions that are coordinated at the nano-, micro-, and meso-levels, and the system exhibits coupled physicochemical interactions linking nanoscale nucleation effects, microscale pore refinement, and mesoscale transport resistance. GNPs impact the nucleation and crack-bridging processes on the nanoscale. TTCB provides reactive silica and supports micro-structural refinement as well as dispersion. FA and GGBS regulate hydration

kinetics and long-term transport resistance. The resulting performance improvements are experimentally assessed and analysed using surrogate-modelling and optimisation methods.

Scientific hypothesis

The main hypothesis of the current study is that a multicomponent binder that includes fly ash -granular ground granulated blast furnace slag (FA -GGBS), thermally treated coir biomass (TTCB), and graphene nanoplatelets (GNPs) will provide synergistic improvements in performance at nanometric, micrometric, and mesoscopic levels, thus, resulting in a high mechanical strength, reduced chloride permeability, and enhanced thermal stability in comparison to both conventional ordinary Portland cement (OPC) and individual supplementary cementitious. In addition, it is hypothesised that the synergistic effect between the reactive bio-derived ash (TTCB) and the uniformly dispersed GNPs will enhance nucleation enhancement, refinement of pores, and crack-bridging effects, which are beyond the additive behaviour, and therefore, instill measurable non-linear relationships between the formulation and functional behaviour of the composite. Lastly, it is hypothesised that these nonlinear interdependencies can be formally summarised into interpretable ensemble-based machine learning models and then utilised in a limited multi-objective optimisation schema to discover environmentally efficient mix designs that balance mechanical strength, durability, embodied carbon dioxide emissions and economic cost.

Novelty and research significance

This investigation is important and can be summarised in four contributions that are related to one another.

- First, the research designs and experimentally confirms a multi-component hybrid binder that incorporates FA, GGBS, TTCB, and GNPs in a single system, which contributes to the development of material design paradigms.
- Second, it illustrates the manipulated thermal treatment of coir waste to produce a functional, bio-derived pozzolan, which shows possible dispersion-enhancing properties, as a part of sustainable building materials.
- Third, it uses interpretable machine-learning models, such as Random Forest, XGBoost, and a CNN-LM hybrid, as surrogate tools to query nonlinear relationships between compositional variables and performance results in the experimentally studied design space.
- Fourth, it combines surrogate modelling with multi-objective evolutionary optimisation (NSGA-II and MOEA/D) to query the trade-offs between mechanical strength, durability (RCPT), embodied CO_2 emissions and cost under realistic constraints.

Notably, the modelling framework is framed as a data-aided exploration device, which exists in the tested experimental space, and not a predictor that is generally applicable.

Objectives and scope

The research is designed based on four interrelated objectives:

- *Material development and characterisation* FTIR, XRD, and SEM methods were used to carry out the production and characterisation of TTCB. A stable dispersion of GNPs was prepared using surfactant-assisted ultrasonication. Hybrid binders were developed with systematically different concentrations of GNP (0.05–0.30 wt%), TTCB (5–15 wt%), and FA–GGBS proportions (20–30 wt%).
- *Experimental performance evaluation* Fresh properties, mechanical strength, durability, such as rapid chloride permeability test (RCPT) and residual strength following exposure to 300 °C were evaluated. Microstructural analysis was conducted to match the hydration mechanisms and interfacial behaviour to the macroscopic performance.
- *Surrogate modelling and interpretability* Random Forest, XGBoost and CNN-LSTM models were trained and validated to predict compressive strength, tensile strength and RCPT. SHAP analysis was used to measure the contribution of features in the dataset.
- *Multi-objective optimisation and sustainability benchmarking* Surrogate models were incorporated in NSGA-II and MOEA/D. Concurrent optimisation of strength, durability, embodied CO_2 (cradle-to-gate) and cost index had been undertaken. Experimental benchmarks were used to evaluate consistency between optimised solutions and experimental benchmarks.

The suggested workflow will integrate experimental validation, interpretable modelling, and constrained optimisation to assist in informed exploration of eco-efficient high-performance concrete in a specific laboratory-scale design space.

Materials and methods—experimental programme

The main node, which is called Hybrid Concrete Mix Design, consists of three major parts: materials, mix design, and testing. All the major constituents of the cement include FA, GGBS, TTCB, and GNPs, which are selected herein to form an alternative and sustainable hybrid matrix of high performance. The Mix Design branch specifies the experimental matrix, consisting of a control mix and a large number of combinations of additional cementitious materials, further extended by the systematic changes in TTCB content and GNP dosages to discuss the synergistic effects. Testing branch categorises the performance test into mechanical (compressive, tensile, and flexural strengths), durability (RCPT, sorptivity, water absorption, and CO_2 permeability), and thermal test (residual strength and mass loss). Together, these interdependent modules form the methodological basis of designing, optimising and validating hybrid concrete mixes to show improved performance in terms

of mechanical integrity and durability. Figure 1a schematic demonstrates the general workflow that should be followed in the experimental programme.

Materials

All the materials that were used in this research were obtained locally to make the research representative and economically viable. Ordinary Portland Cement of 53 grade (OPC 53 grade) that meets the requirements of the IS 12269:2013 was the principal binder. FA, or a thermal power plant on the same premises, also satisfied the requirements of IS 3812 (Part 1):2013 (Type F): GGBS was found to meet the requirements of IS 16714:2018.

Agricultural coir waste used in the production of TTCB was processed, and the biomass was obtained as the resultant product. GNPs of commercial grade (xGnP-C300, purity 99.6%) were purchased from a certified nanomaterials supplier, Platonic Nanotech Pvt. Ltd., Greater Noida, Uttar Pradesh, India, as a research-grade

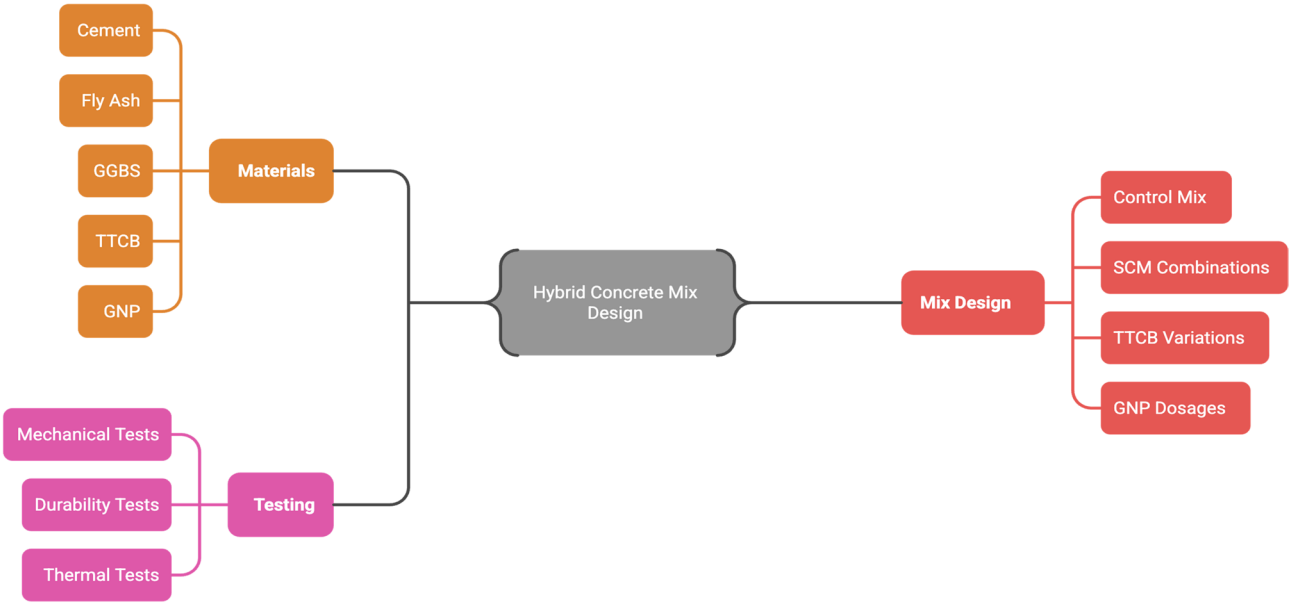

a

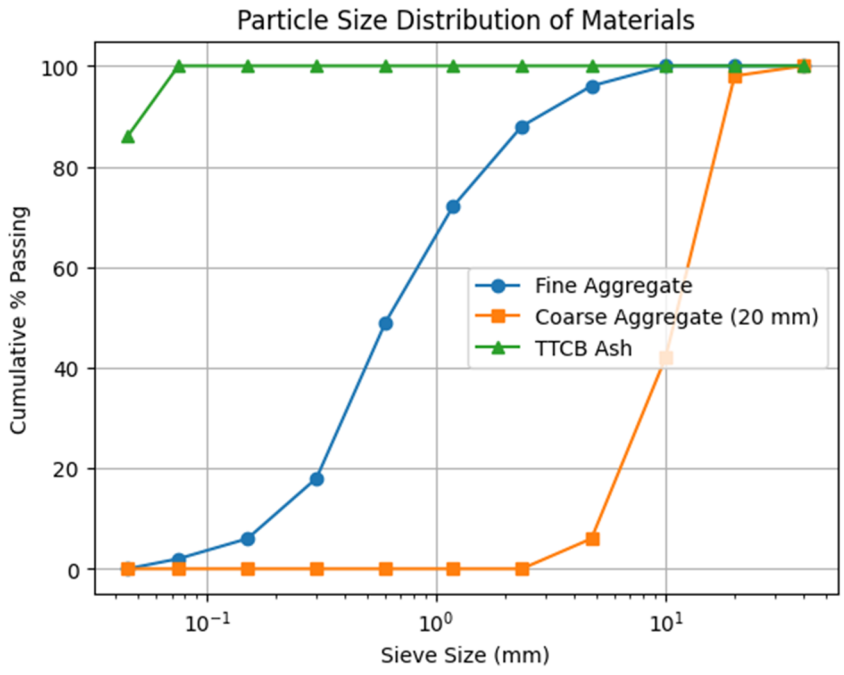

b

Fig. 1. (**a**) Hybrid Concrete Mix Design and Testing framework. (**b**) Particle size distribution curves of fine aggregate, coarse aggregate, and TTCB ash.

Oxide	OPC 53	(FA)	GGBS	TTCB
SiO_2	23.5	50.5	33.0	11.2
Al_2O_3	5.3	23.8	12.6	3.2
Fe_2O_3	2.8	9.5	1.3	0.9
CaO	60.8	8.6	42.5	16.1
MgO	2.3	3.2	7.4	2.1
K_2O	1.1	1.2	0.4	19.0
Na_2O	0.3	0.3	0.2	1.9
SO_3	3.2	0.6	1.9	0.5
LOI	1.0	2.3	0.9	5.4

Table 1. Chemical composition (wt %) of OPC 53, FA, GGBS, and TTCB.

Property	Cement	FA	GGBS	TTCB	GNP (xGnP-C300)
Specific gravity (g/cm^3)	3.13	2.25	2.92	1.98	0.32
Blaine fineness (m^2/kg)	355	315	410	165	–
Bulk density (kg/m^3)	1120	780	1180	420	45
Avg. particle dia. (μm)	14.5	19.0	11.0	9.5	≈ 2
Specific surface area (m^2/g)	0.34	0.31	0.46	0.12	305
GNP thickness (nm)	–	–	–	–	2
GNP lateral size (μm)	–	–	–	–	2.2
Carbon content (%)	–	–	–	–	99.6

Table 2. Physical properties of binder materials.

multilayer graphene nanoplatelet product. The material was supplied in dry powder form and used as received without additional chemical functionalisation, which is characterised by a specific surface area of roughly $305m^2/g$, a thickness of about 2 nm and a lateral dimension of about 2.2 μm. Fine aggregates (crushed coarse aggregates 20mm nominal size) and river sand were used as crushed fine aggregates to meet the requirements of the IS 383: 2016 grades.

Workability was maintained using a polycarboxylate ether-based superplasticiser (PCE) that meets the requirements of IS 9103:2019. Depending on GNP dosage and TTCB content, the dosage of superplasticiser was varied between 2 and 4 kg/m^3.

Table 1 summarises the chemical composition of the cementitious materials as determined through X-ray fluorescence (XRF) and energy dispersive spectroscopy (EDS). The table shows that the cement had about 60.8 per cent CaO, with the FA and the GGBS being high in SiO_2 and Al_2O_3. TTCB was also calcined at 650 0 C and had moderate content of CaO (16.1%) and SiO_2 (11.2%), thus giving rise to its latent pozzolanic properties. Table 2 shows that TTCB had a lower density (1.98 g/cm^3) and it had a coarser texture than GGBS, whereas GNP had a large specific surface area characteristic of nano-platelet morphology. Physical characteristics of the binder materials (Table 2) point to the fineness of the GGBS (11 μm), moderate fineness of FA, and relatively low density of TTCB. GNPs have the greatest surface area, and therefore allow easy nano-scale reinforcement.

Fine aggregate, coarse aggregate (20mm nominal size) and TTCB ash particle size distribution were determined through sieve analysis and the resultant grading curves are shown in Fig. 1b. Fine aggregate meets the Zone II of IS383: 2016 requirements of the IS383: 2016, and coarse aggregate meets the requirements of the stipulated grading envelope. The TTCB ash has ultrafine characteristics with 100% passing rate through 75 μm sieve, thus supporting its application as a SCMs.

Processing and characterisation of thermally treated coir biomass (TTCB)

TTCB was produced using coir fibres that were sourced locally from coconut-processing units in Ranchi, Jharkhand, India. First, the raw fibres were washed properly to eliminate dust, oil and surface impurities. They were then dried in the oven at 105 ± 5 °C for 24 h to dry. After drying, the fibres were milled to a fine powder with a particle size smaller than 150 μm and then dried in a programmable muffle furnace at a heating rate of 10 °C/min at a heating temperature of 650 °C. This temperature was chosen to allow total lignocellulosic breakdown without compromising the presence of amorphous silica phases that are useful in pozzolanic activity. The resulting calcined ash was sieved using a 75 μm sieve and then kept in airtight containers to avoid carbonation or absorption of moisture. The entire characterisation processes were carefully done in the Central Instrumentation Facility, Department of Civil and Environmental Engineering, BIT Mesra, Ranchi and Graphic Era (Deemed to be) University, Dehradun.

The FTIR spectrum of TTCB (Fig. 2a) indicates that three major absorption peaks, namely related to OH, C=O, and C H, are present, which are all indicative of partial organic degradation and silicate formation. The wide OH stretching band at approximately 3400 cm^{-1} indicates the existence of the surface hydroxyl groups

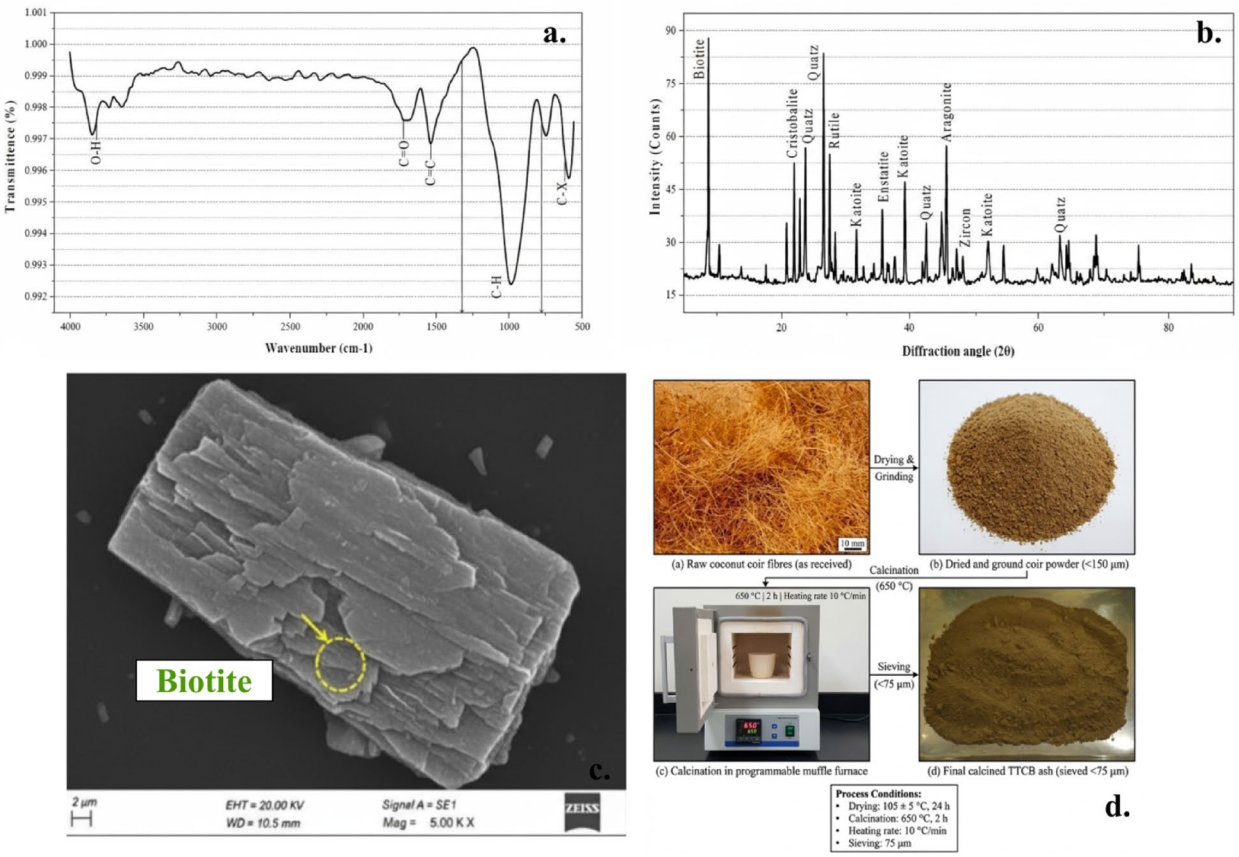

Fig. 2. Characterisation and Processing of TTCB.

and adsorbed water molecules on the silica matrix. As anticipated, this effect is widespread in biomass-derived ash and is beneficial in cementitious uses, since surface hydroxyls increase reactivity with Ca^{2+} ions during hydration[49–60]. Moreover, the C=O stretching vibration of about 1700 cm^{-1} indicates the remaining carbonyl compounds or small lignin fragments that were not changed in the process of calcination; however, their weak intensity proves the close-to-100% organic decay[53–58]. This conclusion is further supported by a weaker C–H stretching band at 2850–2950 cm^{-1}. Together, these few organic signatures, along with the high OH content, conclusively prove that TTCB has a reactive, silanol-covered surface and is mostly mineralised, a most desirable condition in pozzolanic ash.

Notable in the X-ray diffraction pattern (Fig. 2b) are the crystalline phases, which are identified as Quartz, Cristobalite and Biotite, as well as minor traces of Kaolinite, Rutile, Enstatite, Aragonite and Zircon. In particular, the Quartz peaks at $2\theta \approx 26.6°$ and the Cristobalite reflection at 21–22° prove that silica is the major crystalline constituent, which is also supported by a high percentage of SiO_2 in Table 1[59]. These silica polymorphs imply partial crystallinity of an otherwise amorphous matrix, thus providing strength and reactivity[60–65]. The low-angle Biotite reflection indicates a K–Mg aluminosilicate phase that either formed or was retained during the calcination process and is directly proportional to the high K_2O in Table 1. Besides, the lamellar structure of Biotite adds alkali ions capable of increasing pore-solution alkalinity, which promotes secondary C–S–H formation when TTCB is incorporated with cement, FA or GGBS[6263]. As a result, the diffractogram indicates that calcination at 650°C produces a semi-crystalline, silica-based ash with a disordered structure that is both pozzolanic in nature and, at the same time, retains mineral stability.

As shown in Fig. 2c, the scanning electron micrograph clearly shows the distinctive microstructural characteristics of TTCB, which include lamellar, sheet-like particles, which support the XRD results on Biotite. The typical features of this morphology of particles are several layers and stepped edges, which, together, allow increasing the surface area and significant micro-roughness. Consequently, this structural feature has a considerable implication in cementitious systems since it operates in a multifaceted manner. The natural layered silicate texture is a strong nucleating agent, which greatly enhances the development of the critical hydration product, including calcium-silicate-hydrate and calcium-aluminate-silicate-hydrate and subsequently results in a more sophisticated and robust microstructure[64]. Besides, the unique surface irregularities and plate-like geometry contribute to the increased packing density of the particles and optimised pore structure in case TTCB is used wisely with the additional cementitious materials like FA or GGBS[65–70]. Moreover, the intrinsic lamellar structure offers the best anchoring sites, which promote homogeneous nano-scale dispersion of GNPs and successfully address their undesirable agglomeration in the composite binder matrix. Thus, the SEM evidence

shows clearly the dual functional efficacy of TTCB: it is a highly reactive pozzolanic ash, and it is also a bio-adsorptive and dispersive agent, which is essential to the incorporation of GNPs into the composite binder system[71–78].

A combination of all three FTIR, XRD, and SEM analyses confirms that TTCB manufactured at 650 °C consists of silica-rich, potassium-bearing aluminosilicates containing some residual organics. The FTIR bands show hydroxylation of the surface that is favourable to reactions with hydration, whereas the XRD phases give stability and reactive SiO_2[76–82]. Also, the biotite lamellae that are identified by the SEM provide surface area and dispersive potential. These properties, combined with other reasons, make TTCB suitable for incorporation into the hybrid binder as a pozzolanic SCM, as well as a bio-functional additive to promote interfacial bonding and dispersibility of nanomaterials. This behaviour is consistent with the compositional values given in Table 1 and the physical parameters given in Table 2. Based on this, TTCB was used at 5–15% replacement rates in the following mix designs, which guaranteed balanced reactivity, strength contribution, and sustainability in the multi-scale binder system. Photographic documentation of each processing stage is provided in Fig. 2d to enhance methodological transparency and reproducibility. The preparation stages of Thermally Treated Coir Biomass include: (a) raw coconut coir fibres (as received); (b) dried and ground coir powder (< 150 μm); (c) calcination at 650 °C in a programmable muffle furnace (2 h, heating rate 10 °C/min); and (d) final calcined TTCB ash after sieving (< 75 μm).

The basic response of thermal treatment on the surface chemistry and structure of coir biomass is the conversion of fibrous organic substrate into fine, angular ash typified by greater surface hydroxylation and enhanced wettability. This means that it can be mixed without any additional chemical pre-treatment. The equilibrium distribution of the TTCB was reached through dry mixing with cement and additional cementitious materials (SCMs) before water was added according to the standard protocol of fine pozzolanic constituents.

Dispersion and morphological characterisation of graphene nanoplatelets (GNPs)

To achieve the maximum mechanical, electrical, and durability-enhancing properties of GNPs in cementitious systems, uniform dispersion of the nanoplatelets is necessary. However, due to their very high surface energy and a strong van der Waals force, pure GNPs are likely to form dense clusters and hence limit their interaction with the binder. To eliminate this challenge, a surfactant-aided ultrasonic dispersion technique was used to stabilise exfoliation and uniform distribution of the nanomaterial before it was combined with the cementitious binder.

To disperse them, GNPs were added to deionised water with 0.5 wt% of sodium dodecyl sulfate, an anionic surfactant which is known to stabilise carbon-based nanostructures through electrostatic repulsion and hydrophilic forces. The suspension was then ultrasonicated using a 20 kHz probe sonicator at 60% amplitude in pulse mode after 45 min under ambient conditions. The pulsed mode also reduced local heating and eliminated fragmentation or oxidation of the graphene layers[79–83]. The SDS molecules were adsorbed to the graphene surface, and therefore, the surface tension decreased, making the surface wettable and enhancing the exfoliation process and uniform distribution of the nanoplatelets in the aqueous medium. The well-dispersed GNP suspension was immediately mixed with gauging water that is used in the concrete mix to maintain colloidal stability and avoid restacking before mixing. This incorporation measure guaranteed that the GNPs were uniformly distributed all over the binder matrix, thus making it possible to reinforce uniformly at the nano-scale during hydration[25,81,83].

Scanning Electron Microscopy done at the Central Instrumentation Facility, BIT Mesra, Ranchi, validated the quality of the dispersion. The high-resolution SEM micrograph, taken at the 25,000 × magnification, shows that well-exfoliated sheets of graphene are thin with smooth and intact surfaces and sharp edges. Distribution of the nanoplatelets is uniform, with no significant indications of aggregation or stacking-indications of effective exfoliation and stabilisation[77–85]. The platelets are morphologically sub-micron in size and have a high aspect ratio in nature, which gives them a large surface area to bond in the cementitious matrix. The fact that no wrinkled or folded aggregates were observed under non-sonication or mechanical stirrer dispersion is an indication that the combination of ultrasonication and surfactant used was effective at reducing the natural agglomeration tendency of GNPs[81,84].

This quality dispersion will have a strong effect on composite performance. Monolayers of graphene serve as the nucleation sites of the initial stages of hydrated products and thus increase the rate of formation of calcium silicate hydrate gel. Their bi-dimensional geometry enables them to transfer loads across microcracks to enhance tensile and flexural strength, and the interconnected nanosheets enhance electrical conductivity and ion-transport resistance, hence durability[17,79]. Thus, the dispersion protocol adopted transforms GNPs of inert fillers into active nano-reinforcements, which allows the multi-scale hybrid concrete system to perform well in terms of mechanical performance and permeability. Figure 3 shows the SEM micrograph of ultrasonically dispersed (GNPs) with the addition of 0.5 wt% SDS surfactant (EHT = 10.00 kV, Mag = 25.00 kX), and it is observed that well-exfoliated sheets of graphene have been obtained with uniform distribution and smooth surfaces; this proves that there is good dispersion with no agglomeration properties, and hence, good reinforcement capabilities in the hybrid binder.

Structural and morphological verification of the GNPs was conducted using X-ray diffraction (XRD), Fourier Transform Infrared Spectroscopy (FTIR), Raman spectroscopy, and scanning electron microscopy (SEM). The XRD pattern (Fig. 3a) exhibits a dominant diffraction peak at approximately $2\theta \approx 26°$, corresponding to the characteristic (002) plane of graphitic carbon, confirming layered crystalline ordering. Minor peaks corresponding to higher-order reflections ((100), (101), (004), and (110)) further support the graphitic structure. The FTIR spectrum (Fig. 3b) shows characteristic absorption bands associated with O–H stretching (~ 3400 cm^{-1}), C=C stretching (~ 1600 cm^{-1}), and C–O functional groups (~ 1100 cm^{-1}), indicating the presence of surface oxygen-containing groups that may enhance interfacial bonding within the cementitious matrix. Raman spectroscopy (Fig. 3c) reveals the prominent D band (~ 1350 cm^{-1}) and G band (~ 1580 cm^{-1}), characteristic of sp^2-bonded carbon structures, along with the 2D band (~ 2700 cm^{-1}), confirming the multilayer graphene

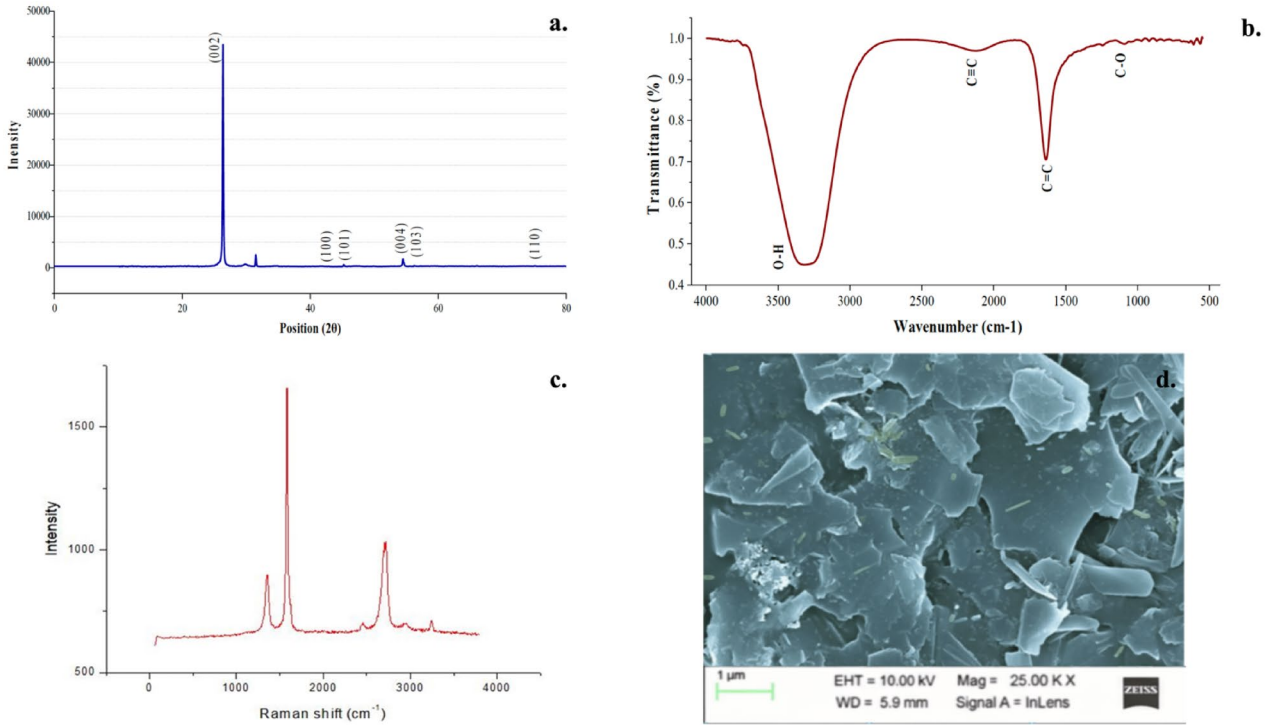

Fig. 3. Structural and morphological characterisation of graphene nanoplatelets (GNPs): (**a**) XRD pattern showing characteristic (002) graphitic peak; (**b**) FTIR spectrum indicating surface functional groups; (**c**) Raman spectrum displaying D, G, and 2D bands; (**d**) SEM micrograph showing multilayer platelet morphology.

morphology. The intensity ratio between the D and G bands indicates the presence of structural defects typical of graphene nanoplatelets intended for composite reinforcement applications. SEM micrographs (Fig. 3d) show thin, platelet-like layered structures with lateral dimensions in the micron range, consistent with multilayer graphene nanoplatelet morphology.

Mix design and batch designations

The mixtures of concrete were designed with the specifications of IS10262: 2019 to guarantee that the concrete mixtures reached M40-grade strength and also cross-tested with ACI211.1 (2018) to guarantee global consistency. The batches were all prepared with a total binder content of 450 kg/m^3 and a constant water-binder ratio of 0.35, thus giving all the specimens an equal hydration and similar performance. The ratio of the fine to coarse aggregates was kept at 0.8:1.0, thus guaranteeing balance in the grading, cohesiveness and workability of the mixes.

The experimental programme involved ten different batches (M1–M10) that were developed to explore the effects of FA, GGBS, TTCB, and GNPs on mechanical and durability properties in a systematic manner. FA + GGBS and TTCB were adjusted between 20 and 40%, and the GNPs level was raised between 0.05% and 0.30% by binder weight. A superplasticiser based on polycarboxylate ether (PCE) was added in the dosage of 2.0–4.0 kg/m^3 to ensure the same slump and flow behaviour with the same consistency of the nano- and micro-additive content.

The batches were coded based on replacement proportions and levels of additives in each batch. The control mix (M1) was 100% OPC with no additional cementitious materials or nanomaterials; thus, it was the reference to the control. Sub-batches of increasing amounts of SCMs, TTCB, and GNPs were then added to investigate possible synergies between them over a spectrum of reinforcement scales. Batches M2, M3 added blended systems with 30% SCMs (FA + GGBS) and relatively small amounts of TTCB (5–10%) and GNP (0.08–0.12%), thus reflecting the shift towards traditional and partially hybrid binders. Batches M4-M6 gradually added TTCB (10–20%). Batches M7–M9 further increased TTCB to 25% with varying ratios of FA-GGBS and nano-dispersion with higher GNP levels (0.22–0.25%) to determine the extent of hybridisation and the nano-dispersion effects. Lastly, the highest substitution rates of SCM (40% in batch M10) and GNP (0.30% in batch M10) were used to measure the highest substitution levels and their effects on composite integrity.

The mix proportions were selected based on literature evidence, initial dispersion limits and the performance workability balance. The level of additional SCM replacement of 30%was chosen according to previous research, which showed that FA–GGBS blended systems between 25 and 35% produce significant clinker content reduction without affecting the performance of mechanical integrity and durability. Replacement levels above 35% often lead to retarded strength development or reduced early-age stiffness in conventional curing regimes, but lower replacement levels offer limited carbon-reduction advantages[86–100]. In the overall SCM fraction, TTCB

was adjusted to 5–10% to determine its dual role as a reactive pozzolan and a nano-dispersion agent. According to the literature on biomass-derived ashes, incorporation rates of more than 10–12% could contribute to higher water demand and negatively affect workability because of high surface area and porosity. Therefore, the range of 5–10% was chosen to be controlled to balance between reactivity and rheological stability. The GNPs were added at 0.08%-0.12% by weight of binder, which is comparable to the optimum nano-reinforcement dosage of cementitious composites. Agglomeration, dispersion instability and strength loss are common with higher GNP contents (> 0.15%), whereas marginal reinforcement effects are common with lower dosages (< 0.05%)[101–120]. The selected range thus represents the expected optimum without causing too much trouble in terms of viscosity and dispersion. The combined proportioning approach allowed for evaluating multiscale interactions systematically, without losing the practical workability and compatibility with traditional mixing protocols. Trial batches were done initially to determine acceptable workability and dispersion stability before finalising the reported mix proportions. Although the ultrasonication was effective at the laboratory level, a high-shear or continuous dispersion system would be required on an industrial scale; the current study reveals evidence of dispersion in the proof-of-concept in the controlled laboratory scenario. Casting and averaging of three specimens per mix per test age were done. As a result, the chosen ranges are a narrow optimisation window, which is characterised by mechanistic evidence, dispersion feasibility, and sustainability factors, as opposed to arbitrary experimental choice.

Table 3 gives the entire percentages of all batches, including the constituents of the binder, the total amounts, the water, and the dosages of the superplasticiser. All batches were mixed in the same conditions to provide a consistent comparative evaluation during the next mechanical, durability, and microstructural tests.

Basis for selection of FA, GGBS, TTCB, and GNP dosages

The dosages of FA, GGBS, TTCB and GNPs have been selected by considering previous research, potential structural constraints of the mixture and experimentation to establish where modifications occur. The 20–40% range of FA and GGBS was employed since it is one of the typical ranges that would enhance the durability without losing excessive early strength. TTCB was experimented with 5 to 25%, with the aim of it being both a reactive pozzolan and a fine filler, whilst avoiding the cement matrix becoming too diluted as well. GNP dosages (0.05–0.30 wt%) of cement weight were selected due to this being the range over which they spread and become sufficient in the number of networks to cause reinforcement. The doses were kept up slowly, to allow the observation of the relations between materials when they assist each other, and when they injure one another, instead of merely endeavouring to produce the greatest possible effect on a given property.

Casting, curing, and testing of specimens

Mixing and specimen preparation were conducted according to the Indian and international standards so as to achieve consistency and reproducibility of all the batches of the experiment. A 60-L capacity pan mixer was used to prepare concrete mixing in line with IS 516 (Part 1):2023, thus ensuring a uniform dispersion of GNPs, TTCB and other components of the binder. The dry constituents (cement, SCMs, TTCB, and aggregates) were mixed first for two minutes so that uniformity is achieved; next, the pre-dispersed GNP suspension was introduced gradually, followed by the addition of the superplasticiser solution. The new mix was then weighed in standard moulds that matched the test specimens required.

The compressive, tensile and flexural properties were evaluated by casting cubes, cylinders, and prisms, respectively, with sizes of 100 × 100 × 100 mm, 100 × 200 mm and 100 × 100 × 500 mm, respectively. A vibrating table was used to compact the material to remove trapped air as well as to achieve uniform density. Wet burlap was applied to the specimens right after casting and demoulded with great care after 24 h. All samples were post-demoulded and cured at 27 ± 2 °C at an IS 9013: 2018, curing ages of 7, 28 and 56 days. This curing regime was sufficient to guarantee proper hydration and strength gain, especially when using the SCMs and nanomaterials in mixes.

To conduct all the experimental testing, a Concrete and Materials Laboratory, Department of Civil Engineering, Noida International University, was used under controlled temperature and humidity. The testing program involved an overall testing of the concrete on mechanical, durability and thermal performance

Mix ID	Cement ((kg/m^3))	FA (kg/m^3)	GGBS (kg/m^3)	TTCB (kg/m^3)	GNP (%)	Water (kg/m^3)	SP (%)	Fine aggregate (kg/m^3)	Coarse aggregate (kg/m^3)
M1 (Control)	450	0	0	0	0.00	157.5	2.0	800	1000
M2	320	65	65	0	0.08	157.5	2.2	800	1000
M3	295	65	65	25	0.12	157.5	2.4	800	1000
M4	275	50	85	40	0.15	157.5	2.6	800	1000
M5	250	55	80	65	0.18	157.5	2.9	800	1000
M6	230	45	90	85	0.20	157.5	3.2	800	1000
M7	220	35	100	95	0.22	157.5	3.3	800	1000
M8	240	70	70	70	0.22	157.5	3.4	800	1000
M9	205	55	85	105	0.25	157.5	3.7	800	1000
M10	215	90	90	55	0.30	157.5	4.0	800	1000

Table 3. Mix proportions for 1 m^3 of M40 concrete (constant w/b = 0.35; total binder = 450 kg/m^3).

in compliance with the applicable IS, ASTM, and ASCE standards. Cube test: The compressive strength test followed IS 516 (Part 1): 2023 and ASTM C39, split tensile strength test followed IS 5816. Third-point loading was performed according to IS 516 to measure flexural strength, and it is a method of determining the bending resistance of the material.

Durability performance was also tested by Rapid Chloride Penetration Test (RCPT) using a 100 × 200 mm cylindrical specimen in accordance with the ASTM C1202, in which a constant potential of 60 V DC was used over 6 h, and the total charge passed was measured in coulombs to measure the chloride permeability. The water absorption and sorptivity properties were evaluated according to ASTM C642, and this gave an insight into the porosity and the surface permeability of the hybrid concretes. Also, thermal resistance and post-heating residual strength were tested, whereby cube specimens were subjected to 300 °C for 2 h, then compressive testing was conducted as per ASTM C177. The given process enabled the indirect evaluation of the thermal conductivity of the material and its structural integrity after exposure to high temperatures.

Triple specimens were done in each mix in order to determine the reliability of the data, and the average was taken to derive representative figures. Therefore, the testing program gave a strict and standardised framework within which the effect of integrating GNPs, TTCB and SCMs individually on the mechanical strength, durability and thermal resilience of the developed M40-grade hybrid concrete system can be studied.

CO_2 emissions quantification

To measure the embodied carbon per tonne of every concrete batch (M1-M10), a cradle-to-gate life cycle assessment (LCA) methodology was performed in the compliance with ISO 14040/44, the GHG Protocol India (Cement Sector Guidance), and data sets were in line with Cement Sustainability Initiative (CSI) and the Alliance for an Energy Efficient Economy (AEEE)[1,3,5,14,16]. This approach takes into consideration all the direct emissions that occur during the production of the raw materials, transportation to the batching venue, and mix preparation. The CO_2 emission per cubic metre of concrete was computed as the expression of all constituents mix elements, namely cement, SCMs, aggregates, fibre, admixtures, and water[1,3,5,14,16]. The contribution of the emission of each constituent was calculated as:

$$E_i = Q_i \times F_i \tag{1}$$

Where E_i = CO_2 emission contribution of ingredient *i* (kg/m^3), Q_i = quantity of ingredient *i* used per cubic meter of concrete (kg/m^3), F_i = emission factor for ingredient *i* (kg CO_2 per kg material).

n is used to indicate the number of components in the mix. The Indian datasets were used to obtain emission factors, which are related to local manufacturing and energy bases. The representative values used were around 0.85–0.95 kg CO_2/kg for cement, 0.05–0.09 kg CO_2/kg FA and GGBS, and less than 0.02 kg CO_2/kg aggregates and fibre. The emissions of transportation and batching were included based on the Indian grid emission factor (≈ 0.82 kg CO_2/kWh) and the average fuel consumption figures that were obtained through the Indian GHG Protocol database.

The total embodied CO_2 for the mix is then given by:

$$E_{\text{total}} = \sum_{i=1}^{n} E_i \tag{2}$$

Cradle-to-gate boundary was selected due to the fact that downstream processes (transport to the site, placement, and service life) are the same in all mixes and therefore have no impact on comparative trends. The calculated CO^2 intensity (kg/m^3) of each batch was based on the material inventory used in the mix design according to the IS 10,262:2019, so that the results of the emissions are directly related to the formulations in the laboratory.

Cost analysis (control-normalised index method)

Economic analysis of the identical concrete batches was done simultaneously to find the effect of the additional cementitious materials (SCMs) and coir-based nano-carbon (TTCB) addition on the material cost. The overall material price per cubic metre (C_{total}) was calculated as:

$$C_{\text{total}} = \sum_{i=1}^{n} (Q_i \times P_i) \tag{3}$$

where Q_i = quantity of ingredient i (kg/m^3), P_i = prevailing market rate of ingredient i (₹/kg or ₹/L), and n = number of components per mix.

Unit rates were calculated based on schedules of CPWD/DSR 2024 and cross-verified with quotes received from regional suppliers in the Delhi-NCR region to depict the real conditions in the Indian market. Normalisation was on the baseline mix (M1, OPC control) with a Cost Index of 1.00. The normalised cost index of any batch was calculated as:

$$CI_j = \frac{C_{\text{total},j}}{C_{\text{total, control}}} \tag{4}$$

This normalisation makes a relative comparison of the cost-effectiveness of all sustainable alternatives possible. The integrated approach guarantees the clear evaluation of environmental and economic performance, with the mix composition being directly connected to sustainability performance. The boundary of the cradle-to-

gate system suits the stage the most vulnerable to replacement of the binder and utilisation of the additives, i.e., raw-material production and concrete batching, and does not consider the confounding influences of the construction or service-life factors[1,3,5,14,16].

The mix proportioning and structural-grade specifications using IS 10262:2019 and IS 456:2000, respectively, will provide a consistent procedure with Indian concrete design practice. The implementation of the GHG Protocol India Cement Tool has the effect of equating the CO_2 quantification with the country reporting frameworks, whereas market-rate normalisation under CPWD /DSR 2024 ensures applicability to price-sensitive Indian construction projects. In general, this process produces two vital sustainability measures (embodied CO_2 (kg/m^3) and normalised cost index) of concrete that jointly guide the multi-objective optimisation process outlined[1,3,5,14,16].

The factors of emissions in the instance of TTCB are considered as the energy of collection, drying, and calcination, and are alleviated by the fact that it is classified as agricultural waste, thus not bearing the production overhead of its upstream. The distance of transportation was also assumed to be equal to regional SCM sourcing, and as such it would not distort conservative estimates. Based on this, TTCB produces a significantly lower embodied CO_2 compared to OPC even after thermal treatment.

Machine learning models and optimisation

An orderly experimental dataset was assembled that included hybrid concretes with partial cement substitution by FA and GGBS, as well as TTCB and GNPs. Each record contained full mix proportions, fresh properties (slump, compaction factor, fresh density), hardened properties at 7 and 28 days (compressive and split-tensile strength), as well as 28-day rapid chloride penetration test (RCPT). Rescaling of continuous variables to similar ranges was done, which eliminates the necessity of categorical encodings. k-fold cross-validation was used to divide the data into training, validation and test subsets. Though it was expected that considerable amounts of collinearity would exist between cement and supplementary cementitious material (SCM) contents, all physically significant variables were included; the model families selected are resistant to multicollinearity.

The modelling data consisted of ten different mix designs tested on various performance outputs (compressive strength, tensile strength, and RCPT). A three-stage data partitioning strategy was adopted to make sure that systematic model assessment is given despite the small sample size. The data was separated into training (70%) and validation (15%) and testing (15%) samples. The model was fitted to the training set, the hyperparameters were tuned and early stopped (where applicable) using the validation set, and the independent performance was evaluated using the test set. Since the dataset size is rather small, k-fold cross-validation ($k = 5$) was also applied during the training step to mitigate variance related to single random splits. The reported final performance measures (R^2, RMSE) in the Results section are related to the held-out test set to guarantee the separation of training and evaluation data.

Each target was trained with three trained regressors: a hybrid CNNLSTM (1-D convolutions over the feature vector followed by an LSTM block to capture age/sequence effects), Random Forest, and XGBoost. In cross-validation, hyperparameters were optimised using grid or Bayesian search. The hyperparameter optimisation was performed with the help of various strategies based on the complexity of the model and the dimensionality of the parameters. In the case of tree-based ensemble models (Random Forest and XGBoost), a systematic grid search with k-fold cross-validation was used, which can be explained by the fact that the hyperparameters of these models are relatively discrete and bounded (e.g. the number of estimators, maximum depth, learning rate). This approach guaranteed a comprehensive analysis in a controlled parameter space, which made it easy to replicate and be rigorous. Bayesian optimisation was used instead of an exhaustive grid search in the CNNLSTM architecture. The dimensionality and continuous nature of the hyperparameters of the neural network (e.g., the number of filters, learning rate, dropout rate, and hidden units) required a more computationally efficient method. Bayesian search provided the possibility to find near-optimal settings and reduce the infeasibility of an exhaustive grid. As a result, different optimisation strategies were chosen based on the considerations of model structure and computational efficiency, all the time without compromising the integrity of performance evaluation by maintaining the same cross-validation protocols. In all cases, identical k-fold cross-validation was applied to ensure fair comparison across models. The evaluation of performance was done on held-out folds based on the R^2, RMSE, and MAE, making sure that the models selected were able to generalise to the training data.

SHAP (SHapley Additive exPlanations) was used to deal with model interpretability. SHAP values measured the contribution of each input to the prediction against a baseline for each trained model and sample. Mean absolute SHAP values were used to give global scores of the feature influence, and the distribution of the signed values was used to show the directionality of the effects of each factor on the targets.

To explore the design, the trained models were used as surrogate evaluators within a multi-objective optimisation problem. The decision variables consisted of the binder fractions and additive dosages, which were limited to realistic limits and a constant water-to-binder ratio $w/b = 0.35$. There were four goals to be optimised at the same time: maximise 28-day compressive strength; minimise RCPT; minimise a normalised cost index; and minimise mix-level CO_2 footprint. Two evolutionary algorithms, NSGA-II (Pareto-based) and MOEA/D (decomposition-based), were used, which produced sets of non-dominated solutions, which provided a data-driven Pareto front of viable mixes, allowing performance and sustainability to be balanced.

Even though the sample of different mix designs that were experimentally studied was small (ten formulations), each mix was described in a variety of performance indicators and test conditions, which produced an organised dataset that could be used in surrogate modelling. The machine-learning part was not aimed at producing a predictive model that would be generalisable, but instead to build constrained surrogate regressors that would be able to represent nonlinear trends in the experimentally validated design space. Since the dataset size is quite small, the model complexity was kept under tight control by using cross-validation and hyperparameter

optimisation to reduce the risk of overfitting. The CNNLSTM architecture was used in a regression context to investigate nonlinear interactions between compositional variables, but its implementation is to be viewed as a functional approximator over the range of interest studied and not as a large-scale deep-learning model. This means that optimisation solutions can only be interpolated within the constrained experimental space and cannot be extrapolated to other parameter spaces. Future research with larger datasets and external validation groups would enhance the overall model generalisability and strength.

In order to determine the most sustainable and high-performing concrete mix systematically, a hybrid multi-objective optimisation framework was created, as shown in Fig. 4. The algorithm combines machine-learned surrogate modelling with evolutionary optimisation algorithms to search the large compositional design space efficiently and find Pareto-optimal trade-offs between conflicting goals.

The workflow starts with the loading of the experimentally obtained dataset, which is the input mix parameters (cement, fly ash, ground granulated blast-furnace slag, TTCB, fibres, superplasticiser, etc.) and the output responses (compressive strength, rapid chloride penetration, embodied CO_2, and cost). An independent random forest (RF) regressor is used to model each output, and it represents a surrogate model, which approximates experimental behaviour without having to run the experiment to exhaustive laboratory experiments. RF model is especially appropriate to utilise this study due to its capability to obtain nonlinear interactions between mix components and performance variables, despite having limited datasets.

Once the model has been trained, we establish constraints on the input values. These limits are based on tested-in-experiment ranges, to make the optimisation remain within realistic physical limits. The limits are also provided in accordance with the practical design guidelines in the Indian Standards, such as IS 10262: 2019 and IS 456: 2000. These optimisation objectives are then expressed in the form of equations.:

$$\text{Minimize}\left[-f_1\left(\text{Compressive Strength}\right), f_2\left(\text{RCPT}\right), f_3\left(\text{CO}_2\right), f_4\left(\text{Cost}\right)\right] \tag{5}$$

In this case, compressive strength was taken as a negative value such that all objectives may be minimised simultaneously, according to the general principles of evolutionary optimization.

Then, further execution of multiple multi-objective evolutionary algorithms, namely NSGA-II and MOEA/D. They were selected as they complement each other. NSGA-II retains the best solutions and ensures diversity through the crowding distance. MOEA/D decomposes the problem into a large number of single-objective problems, a fact that contributes to the formation of a more homogeneous Pareto front.

The algorithm generates a set of the best trade-off solutions of the four goals, known as a Pareto front. Each front presents solutions, in which the improvement of one goal will worsen another. By pooling all the fronts to a single Union Pareto front, which has all possible good candidates. Out of that, selecting one compromising solution. Thus, selecting it by considering its normalised Euclidean distance to the ideal point, thus it trades off strength, durability, cost and carbon footprint.

$$d_i = \sqrt{\sum_{j=1}^{n}\left(\frac{f_{ij} - f_j^*}{f_j^{\max} - f_j^{\min}}\right)^2} \tag{6}$$

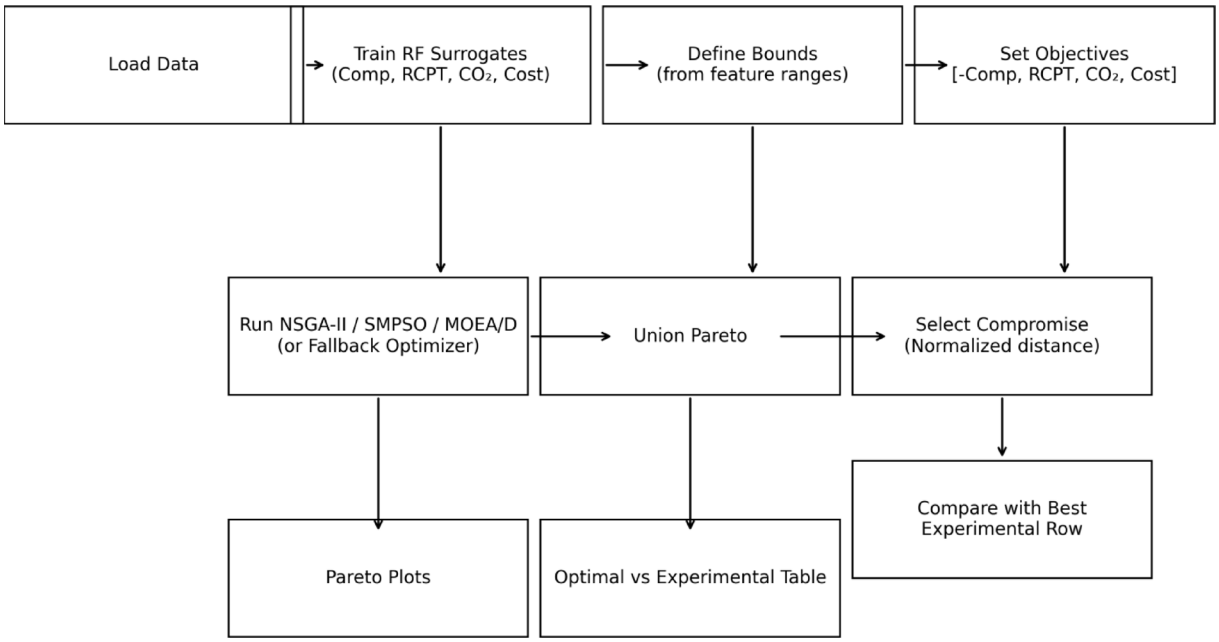

Fig. 4. A hybrid multi-objective optimisation framework.

Where f_{ij} is the value of the jth objective for the ith solution, f_j^* is the ideal (best) value, and $f_j^{\max}$, $f_j^{\min}$ are the respective bounds for normalisation.

Lastly, the study compared the optimal mix of the model computer with the optimal mix of the experiment of M8 or M9 to determine whether the computer model predictions are correct and can be applied in real life. This comparison ensures that the computer-optimised mix is the same as we observe in experiments in terms of strength and durability, and this proves that the hybrid data-driven method is effective.

All in all, this technique allows for consideration of a large number of possible mixes in a short amount of time with minimal lab effort. Through the integration of shortcut models and evolutionary search, the research discovers tangible formulas that are information-founded, satisfy the performance objectives, and are sustainable, between the findings of the experiment and intelligent prediction.

Three machine learning models, including Random Forest (RF), XGBoost, and CNN-LM, were compared. Even though XGBoost and CNN-LSTM proved to be competitive in terms of predictive accuracy, RF was chosen as the surrogate model to be used in the multi-objective optimisation. This choice was informed by the fact that RF performed better in comparison with other alternatives, was more stable in cross-validation folds, and more robust due to the small size of the dataset. In addition, RF was less affected by folds and less prone to over-fitting compared to the other algorithms. With the small size of experimental samples, tree-based ensemble models like RF can offer an accurate nonlinear approximation without the large-scale parameter optimisation of more complex neural networks. RF was, therefore, chosen as the main surrogate in order to guarantee numerical stability and interpretability in the limited experimental design space. The consistency in prediction that is evident in the various models also serves as an added assurance to the trends that have been identified. Given the small amount of data that is characteristic of controlled laboratory experiments, the machine-learning models to be used in this circumstance must be framed as exploratory surrogate models, but not predictors that are universal. They are meant to find nonlinear tendencies in the experimentally valid design space as well as enable informed multi-objective exploration rather than to replace empirical testing or to provide decision-grade predictions.

Results and discussion

Experimental results

Fresh concrete properties

Figure 5 illustrates the fresh concrete properties, which include slump, compaction factor and fresh density; averaged per batch (M1 to M10), therefore, provided comparable information on the effects of different binder compositions and additional additions on workability and density. Figure 5 demonstrates the systematic decrease in the workability parameters with the content of the TTCB and the GNP, and an increase in the replacement levels of FA and the GGBS.

The control batch, M1 (Plain OPC), has the best slump (92 mm), compaction factor (0.96), and fresh density (2470 kg/m^3), which are indicative of the best plasticity and compactness that pure OPC should have without the presence of any supplementary cementitious material (SCM) or nano-additive interference. All three parameters are significantly reduced as the mixes are continued to M2 to M7, with increasing cement content

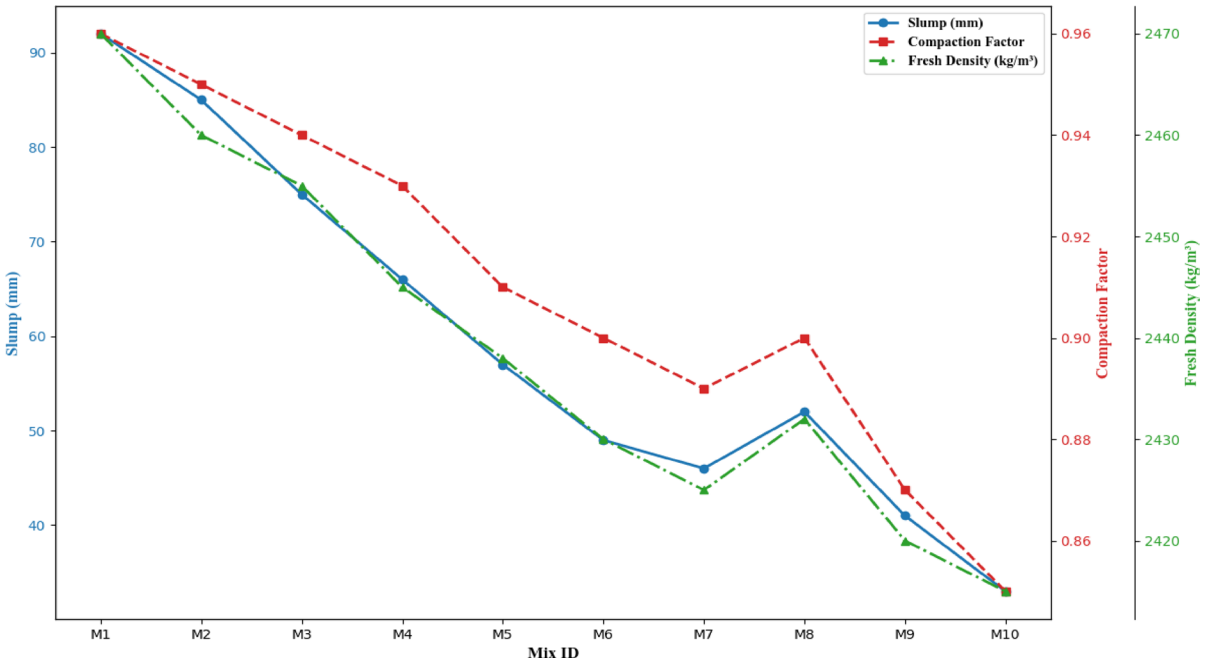

Fig. 5. Fresh concrete properties for Mix IDs M1 to M10, illustrating the effect of varying binder and nano-additive compositions on slump, compaction factor, and fresh density.

being substituted by FA, GGBS, and the proportion of TTCB. The decrease in slump (92mm in M1 to 46mm in M7) is due to the cumulative effect of FA, slower reactivity, angular and irregular morphology of the GGBS particles, along with the hygroscopic and porous characteristics of TTCB. All these properties add to the overall water demand and to the constraint of the cementitious matrix flow, but a stable water-to-binder ratio (0.35) and a small dosage of superplasticiser (2–3.3 kg/m^3) put an upper limit on the attainable fluidity. This decrease is reflected in the compaction factor, which dropped to 0.89 in the identical range, indicating the presence of growing internal friction and decreasing consolidation ease. The use of fibrous and nano-sized materials breaks the continuity of the paste, limits the mobility of the aggregates and entraps air voids, thus encouraging slight increments of porosity. This conclusion is further substantiated by the coinciding decrease in fresh density (kg/m^3 of M1) to (2425 kg/m^3 of M7), since a partial replacement of fresh material with lighter SCMs and biomass materials in combination with entrapped air will produce a less compact fresh matrix.

It is important to note that mix M8 does not follow the monotonic decrease, having a small increase in slump (52 mm), a flat compaction factor (0.90), and a small increase in density (2432 kg/m^3). This blend was a well-thought-out formulation of equal parts FA and GGBS (70 kg each) and a middle range TTCB replacement of 15% and 0.22 kg/m^3 GNP, and an optimal dosage of superplasticiser of 3.4 kg/m^3. The resulting enhancement is the significance of proportion synergy: the spherical structure of FA provides a high lubricity, and packing content of the paste, and the latent hydraulic reactivity of GGBS leads to formative gel properties, both of which reduce the water absorption propensity of TTCB[82,109]. At the same time, moderate GNP content does not overly enrich the microstructure and does not affect viscosity significantly. All these complementary effects combine to provide a mix with enhanced flow and stabilised density that justifies M8 as the optimised formulation with the ability to balance sustainability with desirable fresh-state performance[110,111].

In addition to this balance, M9 and M10 indicate the negative impact of overloading with other binders and nano-additives. As the TTCB contents reach over 20% and GNP reaches about 0.30, the values of slump decrease sharply to 41mm, 33mm, the compaction factor becomes 0.87, 0.85 and the value of density, respectively, becomes 2420 kg/m^3, 2415 kg/m^3. These decreases indicate the reduced dispersion of GNPs in higher concentrations, the increased absorption and surface roughness of water TTCB, and the overextension of the content of SCM, which all contribute to the deterioration of paste cohesion and heightened viscosity of the mix[27,109,112]. Even increasing the dosage of superplasticiser, internal friction, and the low volume of the paste do not allow efficient compaction, as can be seen by the steep fall of all three curves in Fig. 5.

The general behaviour is consistent with the available literature on fibre-modified and nano-enhanced cementitious composites, in which materials with large surface area and porosity increase water demand, break rheological homogenisation, and reduce workability[27,87–91]. Although superplasticisers are effective to some extent in restoring flowability, they cannot work effectively at very high concentrations because of steric hindrance and saturation effects. As a result, it is the optimised balance of FA, GGBS, TTCB, and GNP as realised in M8 which can result in a stable rheological and densification profile[97–104]. The constant decrease in density throughout the series also proves the substitution of dense cement particles with low-specific-gravity SCMs and fibrous materials, but the range of (2415–2470 kg/m^3) is within the acceptable high-performance concrete range[116–118].

Together, the findings of Fig. 5 and Table 5 indicate the negative trade-off that exists between workability and sustainability in hybrid concrete systems. Replacement with TTCB and GNP will improve the ecological and possibly micro-structural performance of the binder matrix but inevitably will deteriorate early-age flow and compactness. However, with the moderate proportions of hybrids, such as M8, there is a synergistic effect between the pozzolanic reactivity, the packing of particles, and the micro-reinforcement that results in balanced fresh-state behaviour. This analysis therefore, verifies that regulated addition of TTCB and GNPs with the aid of well-graded FA-GGBS blends can maintain sufficient workability and density without compromising the densification capabilities and performance uniformity that are the foundation of sustainable high-performance concrete.

Mechanical properties

Determining the mechanical properties of ten hybrid concrete mixes (M1-M10) is presented in Fig. 6, which shows how compressive, flexural and tensile strength changes with binder composition, SCM proportions, TTCB substitution and GNP dosage. The trend observed is unique and internally consistent with mix design (Table 3) and fresh-state behaviour (Fig. 6). All mechanical properties grow steadily to the optimal mix M8, and then decrease when the contents of the additives are above their effective threshold (M9–M10).

During the initial period of curing (Fig. 6a), the compressive strength of the seven days is steadily increasing, beginning with 29.7 MPa in the control mix M1 up to about 39.3 MPa in M8. This steady increase is an indication of the positive synergy of FA and GGBS, which serves as micro-fillers and nucleation sites of early hydration and TTCB supplements, amorphous silica that reacts with calcium hydroxide to produce secondary C–S–H gel[121]. Additional refinement of the pore structure and the increase of skeleton strength are attained by the incorporation of well-distributed GNPs, which further increase the densification of the matrix and interfacial bonding[122,123]. Moderate changes in superplasticiser in this range ensure that there is adequate flow to ensure that dispersion is adequate. The seven-day findings also indicate that appropriately balanced SCMs and nano-additives are capable of increasing early reactivity without adding more clinker[124,125]. With time elapsing (Fig. 6b) to 28 days, the differences between mixes are even more pronounced. The compressive strength is raised in M1 to a high of 44.1 MPa, which is improved to a maximum of 55.2 MPa in M8, which is almost 25%. The increase between M2 and M8 is caused by the long-term pozzolanic and latent hydraulic action of FA and GGBS, which constantly dissolves $Ca(OH)_2$ and forms stable C–(A)–S–H gel, and TTCB and GNPs jointly filler the pack and allow crack-bridging at the nanoscale[126,127,128]. M8, which balances FA–GGBS (70 kg each), moderate TTCB (15%), and 0.22% GNPs, is the most efficient hydrating and microstructurally refined material, with its fresh

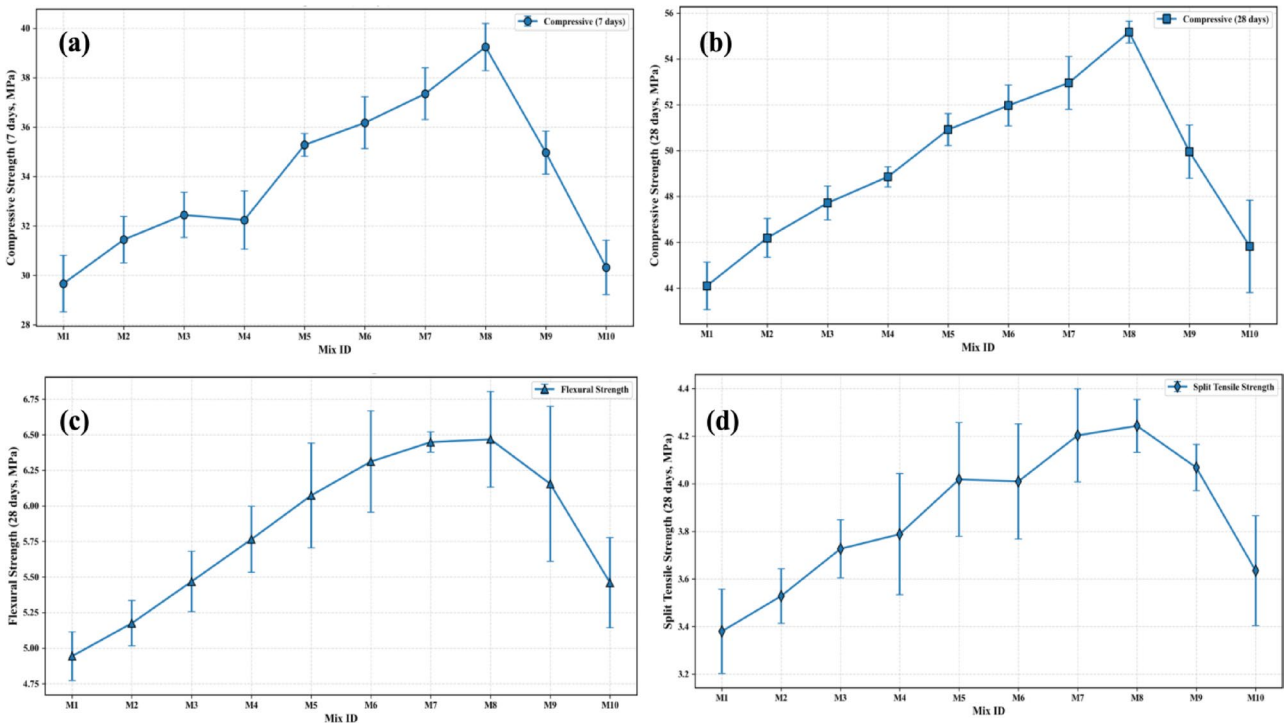

Fig. 6 . Mechanical properties of all concrete batches (M1–M10): (**a**) compressive strength at 7 days, (**b**) compressive strength at 28 days, (**c**) flexural strength at 28 days, (**d**) split tensile strength at 28 days.

density and compaction factor also optimised in Fig. 4. But at M8, compressive strength decreases drastically: the M9 and M10 levels have too much TTCB (>20⁻) and increased GNP dosage, lowering the useful binder fraction, increasing water demand, and agglomerating the particles. These impacts inhibit dispersion, favour the formation of micro-voids, and weaken the interfacial transition zone (ITZ)[27,91,129–131]. Figure 6c shows that the flexural strength outcomes at 28 days behave in parallel to each other. The values begin at 4.9 MPa at M1 and are almost linear up to 6.5- 6.6 MPa at M8. The enhancement is attributed to the micro-crack bridging through homogeneous dispensation of biomass fines and GNP platelets and the increased density of packing through the ternary binder system. The spherical morphology of FA increases the paste mobility, GGBS provides reactivity and roughness at the ITZ, which results in the enhanced fibre-matrix bond and increased energy intake[91,109,129]. M9 and M10 also show significant flexural capacity loss even at high additive content, illustrating the adverse impact of clustering and loss of workability at very high dosage. Nanoparticles and excess fibres form discontinuities instead of reinforcement, which proves the sensitivity of flexural performance to the quality of dispersion and mix rheology[29,83,132]. These findings are reaffirmed by the results of the 28-day split-tensile strength (Fig. 6d). Strength values increase between 3.4 MPa (M1) and 4.3 MPa (M8), which are the effects of an increase in the homogeneity of the matrix and controlled crack-propagation routes. The ensuing decrease in M9 and M10 is similar to the compressive and flexural test, since as porosity and poor compaction increase, tensile integrity is reduced. The increasing error bar in these two mixes proves the existence of more microstructural inconsistency, which is probably due to the agglomeration of TTCB particles and GNP clusters that disrupt bonding networks[133–140].

The two-age compressive strength assessment (7 and 28 days) is diagnostic and performance-based. Early-age strength measures the hydration kinetics and early binder efficiency that are vital in determining the setting behaviour, removal of formwork and structural safety of the construction[94,106,112]. The 28-day strength, conversely, is the normal reference point of long-term structural dependability and maturity of the pozzolanic and secondary hydration reactions. The progressive increases in compressive strength of all mixes between 7- and 28-day in the present study (≈40–52%) underscore the successful application of SCMs and reactive fillers in hydrating the mixes past the initial curing phases[136–138]. In general, Fig. 6 shows that the mechanical improvement of the samples to M8 is the direct result of the optimal combination of the SCMs (FA and GGBS), moderate TTCB introduction, and controlled GNP content- each of which leads to the refinement of pores, enhanced packing, and increased development of ITZ. Outside this limit, the benefits are counter-optimal because overly large fines and nano-additives reduce workability, cause uneven distribution, and reduce compaction efficiency, as already shown in Fig. 4. The synergistic interpretation of the fresh and hardened performance, hence, makes M8 the most-performing hybrid mix, which can provide high early-age strength, improved flexural and tensile behaviour, and long-term sustainability of the material due to synergies in material design. The strength improvement at an early age can be explained by the synergistic effect of nucleation and filler effects. GNPs serve as high-energy nucleation centres, and thus speed up the precipitation of C–S–H, whereas fine TTCB particles

increase the packing density and local alkalinity. At the same time, GGBS displays latent hydraulic reactivity at high pore-solution pH, and, in general, increases the pace of hydration without raising the quantity of clinker.

Durability properties

Figure 7 shows the development of durability and thermal stability of all ten hybrid concrete batches (M1-M10), at twenty-eight days, to determine the complex effect of pozzolanic reactions, microstructural refinement, and hybrid fibre-nanoplatelet modification. The assessed properties are RCPT, compressive strength after being subjected to 300 °C, water absorption, and sorptivity, and a combination of them gives a comprehensive view of the pore structure, permeability, and heat degradation in the hybrid binder system developed. The overall tendency is similar to those of mechanical properties (Fig. 6) the durability and stability increase steadily up to the control mix up to M8, and then decrease, which proves the clear existence of the optimum range of dosages of the ternary and nano components.

Starting with the control batch, M1, it can be stated that the system shows the best performance in all indicators: RCPT = 870 C, water absorption = 4.8%, sorptivity = 0.22 mm/√min, and after 300 °C the residual strength = 78%. These values are characteristic of the behaviour of a dense yet conventionally porous OPC matrix, in which massive connected capillaries and unreacted calcium hydroxide promotes both the migration of chloride and the thermal cracking[141–147]. A lack of pozzolanic refinement leads to coarser network of pores and is more prone to ionic and thermal attack[148–150].

The transport properties are changed drastically with the addition of FA and GGBS, and the gradual addition of low to moderate amounts of TTCB and GNP in M2-M4. The values of RCPT decrease (to 770, 690, and 620 C), water absorption and sorptivity decrease to 4.4%–3.8% and 0.20 mm/√min—0.18 mm/√min, respectively. Simultaneously, the residual strength increases by 81% to 86%[151–155]. The $Ca(OH)_2$ reacts with FA/GGBS to produce secondary C–(A)–S–H gel, which fills micro-voids and enhances the connection of pores. Major additions of TTCB and graphene also increase this densification. TTCB fine, reactive silica acts as a micro-filler and the dispersed nanoplatelets of graphene lead to nucleation of products associated with hydration and block ion transport pathways[27,84,122–124]. The effect of the combination is a tighter and less permeable structure without reduced cohesion or workability[84,102,122,156–160].

Further moving to M5-M8, all indicators are at their most favourable values, which forms the range of optimum hybrid synergy. RCPT has continued to decrease, with a minimum of approximately 505 C in M8; water absorption is 2.8%, and sorptivity equals 0.15 mm/√min with residual strength of approximately 94%. These advancements are signs of a highly developed pore structure and high quality chloride and moisture resistance. The proportion of FA and GGBS will maintain the pozzolanic reactive and the long-term C–S–H gel formation, and TTCB will provide reactive silica as well as the carbonaceous phases, which are thermally stable to provide the heat resistance. In turn, GNPs form an extremely tortuous micro-pathway and reinforce the ITZ, with the help of nanoscale bridging and interfacial bonding[161–166]. The outcome is a small, moist, and thermally

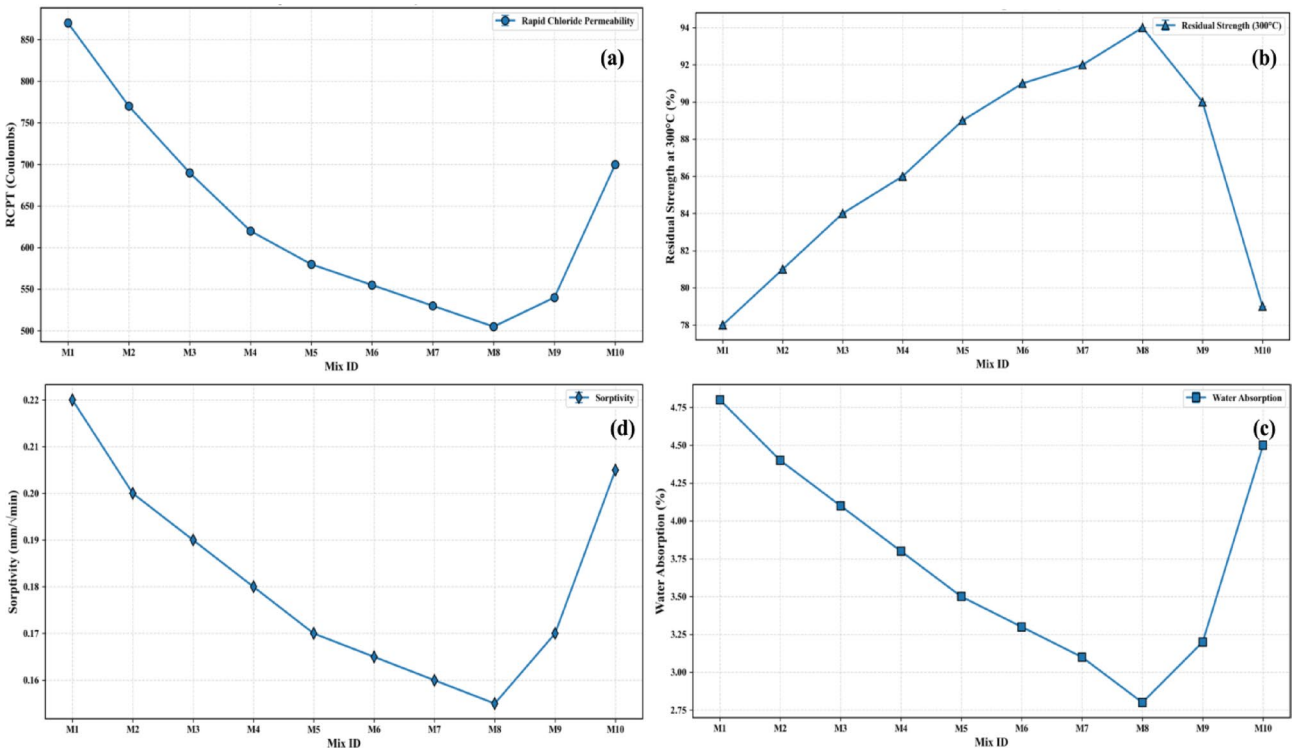

Fig. 7. Durability and thermal resistance characteristics of hybrid concretes (M1–M10): (**a**) Rapid Chloride Permeability (RCPT), (**b**) Residual Compressive Strength at 300 °C, (**c**) Water Absorption, and (**d**) Sorptivity.

stable matrix, which supports the fresh-state compaction and stability of density that was previously noticed (Fig. 5). Mix M8 therefore is the formulation that is optimised in that micro- and nano-scale interactions are considered to give the highest degree of densification without compromised uniformity[163–170].

At levels M9 and M10 performance deterioration is apparent beyond the optimum. RCPT goes up (to 540 and 700 C), absorption of water goes up (3.2% and 4.5%), sorptivity is back (0.17 and 0.205 mm/√min), and residual strength plummets (90% and 79%). Such changes are due to excessive dosing of TTCB and GNP, which increases the water demand, increases the thickness of the paste, and makes it difficult to compact the paste[37,101]. In such concentrations, TTCB particles and graphene sheets are more likely to form clumps and create weak points and partially bridged pores that negate previous gains in the densification. The resultant discontinuities in microstructure propagate localised porosity and permeability, lessening the resistance to chloride and thermal integrity. The greater variability of experimental data in M9–M10 is also a testament to the heterogeneity which is brought about by poor additive dispersion[171–176].

The improvements explained by changes between M1 and M8 can be mechanistically related to three processes that occur simultaneously. First, the chemical refinement by the use of prolonged pozzolanic and latent hydraulic reactions: FA and GGBS react with $Ca(OH)_2$ to form more C–(A)–S–H gel, reducing the pore connectivity[82,132]. Secondly, physical refinement through filler effects: TTCB fine ash particles fill micro-voids, and GNPs fill micro-cracks with their high aspect ratio, which serves as ion transport barriers[76,124,133]. Third, interfacial strengthening: the hybrid binder forms a dense ITZ that contains micro-fibres and nano-platelets that strengthen the bond and enhance the moisture resistance and residual thermal strength[134,135]. The net effect is the decrease in the level of diffusivity and capillary suction, which is indicated by the sudden decrease in the level of RCPT, sorptivity, and water absorption.

The threshold phenomenon, which is characteristic of highly filled hybrid concretes, is confirmed by the subsequent losses in M9 and M10. Beyond a critical level of total non-cementitious content, the dispersion and hydration of the matrix is no longer maintained and clustering and unreacted pores form, which establish connected porosity and do not seal it out. Positive tortuosity of the pore network is replaced by the irregular pathways that ease the water uptake and chloride movement[129,136–138]. At the same time, higher internal stresses during a heating process due to uneven distribution of additives decrease the power of the matrix to maintain the strength at higher temperatures[139,140].

All in all, the results presented in Fig. 7 regarding the durability are in perfect agreement with the mechanical behaviour of Fig. 6. The closer the binder composition is to M8, the more the microstructure becomes compact, the permeability barrier becomes stronger, and the better the resilience of the matrix to ionic diffusion and heat degradation will be. More than this composition, excessive addition of hybrid components compromises the workability and structural uniformity at the expense of previous benefits. The results confirm that a reasonably balanced mixture of SCMs, thermally treated, biomass filler, and GNPs results in a concrete matrix with low permeability, low capillary suction, and high post-fire strength retention, which are the typical characteristics of a stable and sustainable high-performance concrete system.

This selection of 300°C is a moderate thermal exposure which is relevant to real-life fire and post fire service scenarios, where dehydration of hydration products and microcracking initiation takes place without a total collapse of the matrix. This temperature aids to make a comparative analysis of residual strength retention compared to ultimate fire resistance and in this manner serves to act as a screening heat of durability.

Microstructural evolution and correlation with macro-performance

The microstructural characterisation using scanning electron microscopy, Fourier-transform infrared spectroscopy and X-ray diffraction was essential in developing mechanistic correlations between mix composition and macroscopic performance. Indicators of transport durability, including recycled concrete penetrating test, sorptivity and water absorption, are controlled by the pore connectivity, hydration morphology, and the quality of the interfacial transition zone, none of which can be deduced based on the mechanical data alone. In that way, these methods will cause the proposed interactions between additional cementitious materials, titanium-tetracycline binders, and GNPs.

Figure 8a–e shows the gradual change of the cementitious matrix through a control (M1), a porous, highly refined hybrid gel (M8), and an overdose, porous structure (M10), shown in the sequence of the SEM. The progression reflects directly the fresh, mechanical, and durability tendencies, which were mentioned previously (Figs. 5, 6 and 7), providing the morphological confirmation of the presence of the macroscopic results.

Figure 8 represents the SEM micrographs at 28 days which illustrates the development of the binder microstructure of the representative mixes, whereby (a) represents the batch M1—control OPC with plate-like portlandite (CH) in a relatively open C–S–H matrix; (b) represents the batch M4—needle-like hydrates and nucleation features of early pozzolanic refinement; (c) represents the batch M7—dense C–S–H with minimal CH remains, early densification; (d) represents the batch M8 On each panel, the scale bars and magnifications are recorded.

The baseline OPC control matrix is in Fig. 8a of batch (M1). The structure is mainly dominated by large, plate-like crystals of portlandite, which are incorporated in the loosely bonded C–S–H structure. This morphology is characteristic of low pozzolanic contribution, and hydration is restricted to the primary C–S–H formation and some secondary gel development[177–180]. This microstructure is the reason for poor transport resistance (RCPT = 870 C, water uptake = 4.8%) and low compressive strength (44 MPa) of the control. Interconnected pores and unreacted CH are poor planes of transport and channels of ion transport[181,182].

Figure 8b of batch (M4) identifies the initial impact of FA + GGBS addition and low TTCB level. The micrograph indicates partial densification, with slender needle-like ettringite, C-S–H filaments that are loosely interwoven. The presence of visible voids is less than that in M1. Free CH loss in this instance is evidence of secondary hydration by SCM reactions[95,145]. These morphological changes are accompanied by quantifiable

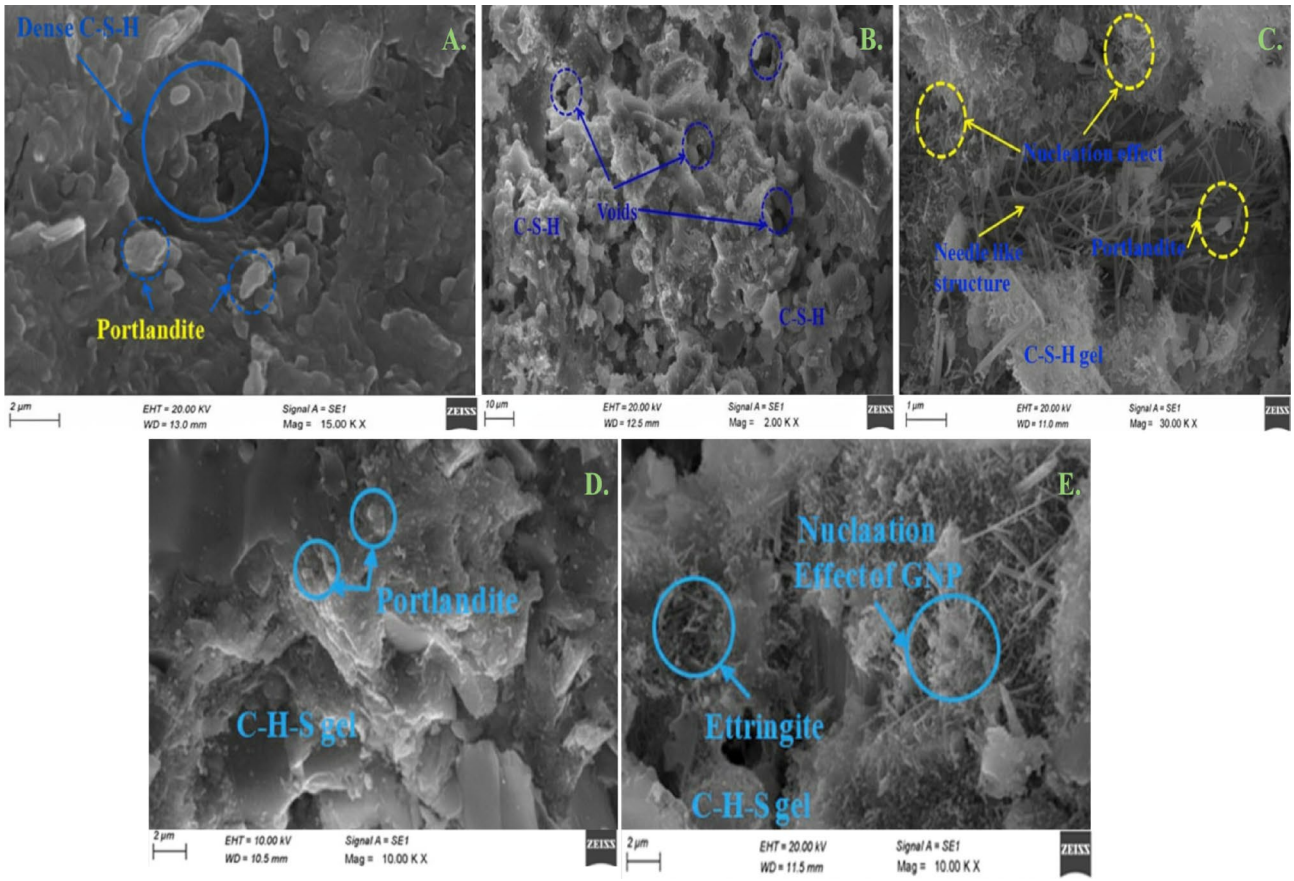

Fig. 8. SEM micrographs.

increases in—RCPT reduces to 620 C, absorption decreases to 3.8%, and compressive strength at 28 days increases to 49 MPa, indicating the beginning of pore refinement and enhancement of bonding[146–148].

A fine, pre-optimum microstructure is depicted in Fig. 8c of batch (M7). C–S–H seems continuous and compact; CH residues and the number of open pores are very small. The gel structure is less disordered compared to M4, which indicates that it is highly hydrated and that fillers interact well[149–151]. This quantitatively translates to high mechanical performance (compressive strength = 53MPa, flexural strength = 6.4MPa, split tensile strength = 4.2MPa) and high durability (RCPT = 530 C, absorption = 3.1%). The thick texture means that SCMs, TTCB, and a moderate dose of GNP all refine the ITZ and produce a compact and low-permeable matrix[6,17,132].

Figure 8d of batch (M8) represents the optimised microstructure. The C–S–H gel is very dense, smooth, and interlaced with fine ettringite needles and clear clusters of the GNP-induced nucleation. Portlandite is nearly completely exhausted, which proves the full conversion of pozzolans and maturity of binders[144,152]. This microstructure represents the mechanical and durability extremes: compressive strength = 55.2MPa, RCPT = 505 C, absorption = 2%, sorptivity = 0.155 mm/√min, and remaining compressive strength at 300 °C = 94%. The GNPs generate nucleation sites that enhance the kinetics of hydration and optimise pore connectivity, whereas TTCB micro-ash and SCMs provide reactive silica and filler effects, which are multiplied to form a multi-scale dense network[26,102,123].

The post-optimum degradation is caught in Fig. 8e of batch (M10). The gel looks fractured, has bigger voids, cracks, and discontinuous C-S–H clusters. The high level of TTCB and GNP leads to the heightened water demand and viscosity, lessening the efficiency of compaction and agglomeration of additives. This is why the deterioration has been observed: RCPT = 700 C, absorption = 4.5%, and compressive strength has decreased to = 45MPa. The loss of homogeneity and reconnected pore pathways at high additive loading are supported by the SEM evidence of micro-voids and CH reappearance[140,153].

The C-H-to-C-S–H conversion pathway (M1 → M4 → M7 → M8) perfectly correlates with the decreasing permeability data and the increasing strength data. RCPT and water uptake decrease by almost 40–45%, compressive strength rises by more than 25%, and residual thermal retention rises by 78%-94%. In the meantime, porosity and density of microcracks observed in M10 are associated with the recovery of performance observed in mechanical and durability tests[129,154,155]. The microstructural densification index, which is estimated based on the CH content and gel continuity, exhibits a close linear relationship with RCPT and sorptivity. This confirms that morphological refinement witnessed in SEM is directly controlling the transport behaviour and the performance in general[130,153,156].

Figure 8a–e illustrate the entire progression of the hybrid system as shown by its SEM evidence. M1 is defined as CH-dominated and permeable; M4 is defined as the start of pozzolanic pore refinement; M7 is defined as the start of practically sealed pores with synergistic SCM-TTCB interaction; M8 is defined as the maximum microstructural compactness with nucleation by GNP; and M10 is defined as the reintroduction of porosity and weak zones by over-dosage. Such images therefore furnish morphological evidence of the same balance that is expressed in all the macroscopic observations, that optimal synergy between FA, GGBS, TTCB, and GNP results in a dense, durable and thermally stable matrix, and that a loss of that synergy results in the loss of the benefits through structural heterogeneity.

3D response surface analysis and literature comparison of compressive strength

The response surfaces in Fig. 9 all suggest that compressive strength is largely controlled by the chemistry of the binder and the presence of nanoscale modifiers as opposed to differences in the type of aggregate in the range considered. The replacement of OPC by FA and GGBS proves a gradual reduction of strength, but the addition of TTCB and GNPs induces stronger nonlinear changes, thus indicating nucleation-controlled densification processes. The fact that the gradients that can be seen on the majority of the surfaces are rather smooth, and that there are no sudden instability areas, supports the fact that the experimental domain is well-defined, and that there are no sudden instability areas, which in turn supports the appropriateness of surrogate modelling in this parameter space. Lastly, the interaction plots that show the GNP-TTCB interactions also highlight the existence of an optimum intermediate nanoscale dosage regime where marginal gains diminish in concert with dispersion-regulated reinforcement behaviour.

Figure 9a–i represent 28 days compressive strength versus combinations in pairs of cement (FA), ground GGBS), (TTCB), and (GNP). At constant other variables kept close to the middle levels, the cement-FA and cement-GGBS surfaces (Fig. 9a,b) approach a peak in the middle of the replacement and drop. At 1020% FA enhances later-age strength through the pozzolanic use of $Ca(OH)_2$ and refinement of pores; however, above a specific dilution threshold (about 20% FA) the dilution penalty takes over and the strength decreases after 28 days[141,142]. This is a similar shoulder case to that of GGBS: anything up to about 30% enhances strength by latent hydraulic reactivity; anything above 30–40% slows down hydration to the extent that strength decreases after 28 days[141]. Present data adhere to such ridges: M8 (balanced FA + GGBS) reaches a top of 55 MPa, 25 per cent higher than the all-cement M1 (44 MPa), and M10 (high FA and GGBS) drops to about 46 MPa—clear evidence of a replacement threshold beyond which strength suffers (Fig. 9).

In (Fig. 9e) plateau of the FA-GGBS surface at about 10–20% FA with about 20–30% GGBS is higher than either of the SCMs alone. GGBS strengthens faster; FA strengthens later, and both achieve maximum effects in packing and micro-filler[141,142]. This is the reason the second-highest (M7, which is around 53MPa) has a balanced FA + GGBS ratio, as opposed to the single-SCMs approach.

The optimum is evident in TTCB surfaces in (Fig. 9c, f and h). Minor additions (about 1–2% by binder) raise strength—in line with micro-filler and nucleation actions that densify paste and the ITZ, but where 3- 4% and above agglomeration, increased water requirement, and effective binder dilution occur, diminishing strength is observed[143]. At high FA, TTCB partially restores strength (Fig. 8f), suggesting that TTCB can be used to fulfill the pozzolanic potential of FA by seeding hydrates. The same moderation is observed with GGBS (Fig. 8h), a thin layer of about 1–2% TTCB reinforces slag-bearing mixes ; beyond this level TTCB turns the profit against the gain[143].

Even the lowest GNP dosages (0.05%) generate a sharp increase in strength as observed in (Fig. 9d, 9g and 9i) due to the characteristic of 2D nucleation templates and nano-reinforcement that hasten the formation of hydrates and seal microcracks[144]. After around 0.1% the benefit levels off or hits a plateau[144]. Figure 8g–i indicate GNP moves the optimum to higher SCM content and extends the high-performance plateau: in the presence of 30–40% GGBS or perhaps 15–20% FA, mixes with 0.05% GNP give high strengths otherwise dropping at 28 days[145]. This corresponds to the matrix where present batches of GNP-free or GNP-overdosed perform worse than M8 at around 0.05%GNP.

On all nine surfaces, the sweet spot is moderate SCM replacement and low nano/micro dosage, just enough clinker to provide primary hydration; just enough FA + GGBS to provide secondary C–(A)–S–H. Beyond these points, 30% total SCM by 28days, 1% TTCB, 0.05% GNP -introduces dilution, agglomeration and compaction penalties, which decrease strength (Fig. 9)[141,143–145].

Mechanistic links and FA and GGBS thicken by absorbing portlandite and creating more C–(A)–S–H; TTCB contributes to micro-filler/nucleation sites that narrow the ITZ; GNP is also a source of nucleation and nano-bridging. They all contribute to increased hydration efficiency and impede transport pathways, and present measures of durability also support this (Fig. 7). Prior optimisation and response surface work on multi-component binders reproduce the same mechanisms—and limits—as in prior optimisation and response-surface work[146]. Overall the response surfaces in Fig. 9 graphically depict why M8 performs better (55.2 MPa) and why M10 slides back, balance gains; overshoot loses.

Table 4 compares the present study's best mixes with representative reports on binary/ternary/quaternary systems with FA, GGBS, carbon black analogues and graphene-family nano-additives. The batch M8 (OPC + 15% FA + 15% GGBS + about 1% TTCB + about 0.05% GNP) has 55.2 MPa at 28 days of standard curing- competitive with most mixes in the literature with its lower clinker. The literature of 20–30% procurement increases with 0.04%-10% graphene derivatives or about 4% fine carbon black proves the enhancement and the presence of narrow optimal nano/micro ranges[143–145].

Taken together, Figs. 8 and 9 and Table 4 indicate that a quaternary, dual-scale carbon strategy (micro TTCB + nano GNP) may be used to open the door to high strength with reduced cement, but it is important to maintain dispersion and dosages[146].

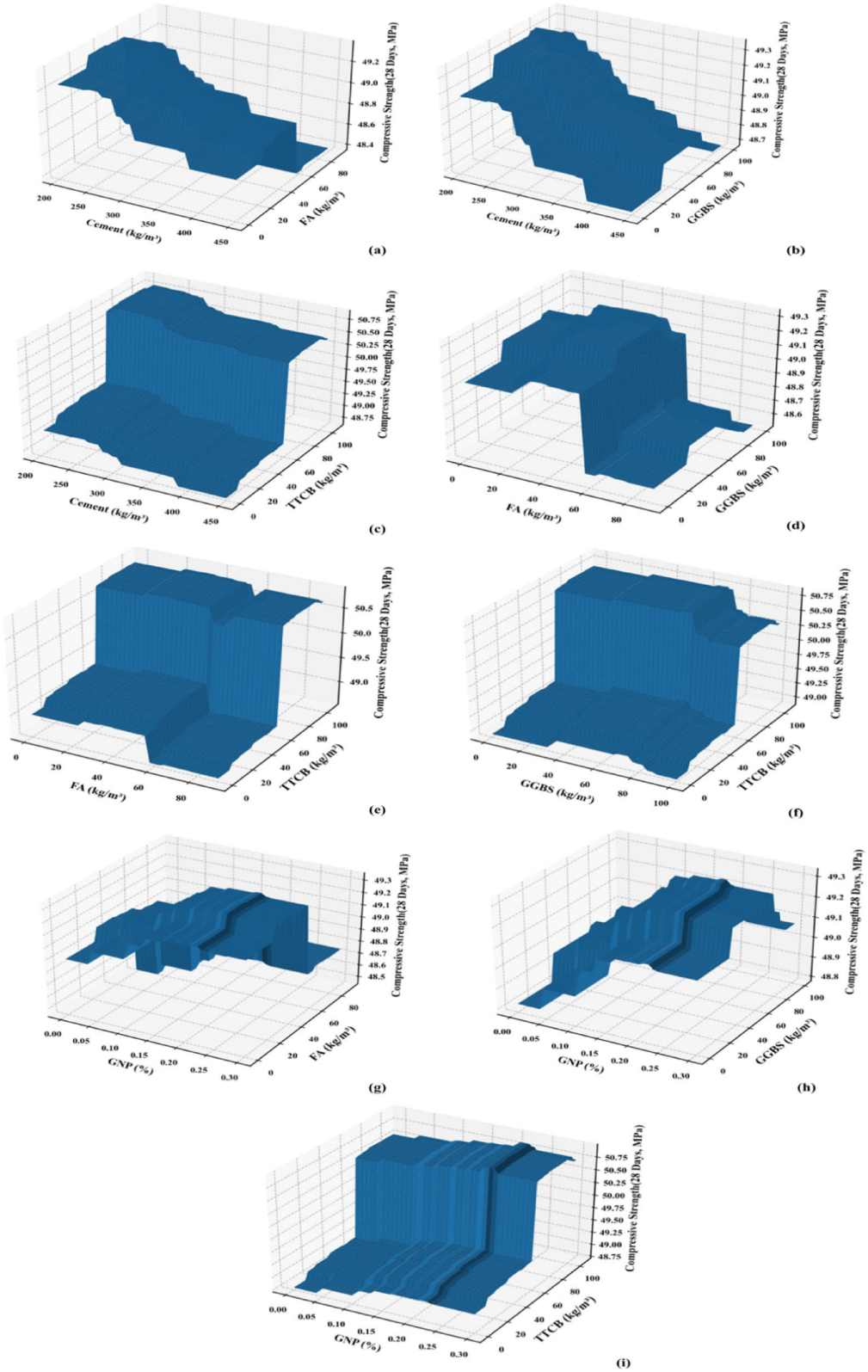

Fig. 9. 3D response surface plots (**a**–**i**) of 28-day compressive strength versus pairwise combinations of cement, FA, GGBS, TTCB, and GNPs. Ridges mark optimal zones at moderate FA/GGBS and low TTCB/GNP; strength declines beyond those optima due to dilution, agglomeration, and compaction effects discussed in text.

Mix/source	Binder composition (OPC + additives)	28-day compressive strength (MPa)	Curing condition	References
M8 (Present study)	OPC + 15% FA + 15% GGBS + ~1% TTCB + ~0.05% GNP	**55.2 ± 0.5**	28 days, moist (23 °C)	Present study
M7 (Present study)	OPC + 10% FA + 20% GGBS + ~1% TTCB + ~0.05% GNP	**53.0 ± 1.2**	28 days, moist (23 °C)	Present study
FA 10% + GO 0.05%	OPC + 10% FA + 0.05% graphene oxide	62.0 (± 2.5)	28 days, water	[183]
Tire-derived graphene	OPC + ~0.10% graphene (from tire pyrolysis)	~40 (≈ + 30% vs. ~30 MPa control)	28 days, moist	[184]
Pyrolytic carbon black	OPC + 4% carbon black (waste-tire derived)	~37 (≈ + 26% vs. ~29 MPa control)	28 days, standard	[185]
FA-geopolymer + GNP	FA-based geopolymer + 1.0% GNP	44.0 (1.44 × control 30.6 MPa)	28 days, ambient	[186]
GGBS 30% + GO 0.04%	OPC + 30% GGBS + 0.04% graphene oxide	51.5 (≈ + 15% vs. control)	28 days, moist	[186]

Table 4. Comparison of 28-day compressive strength with previous studies.

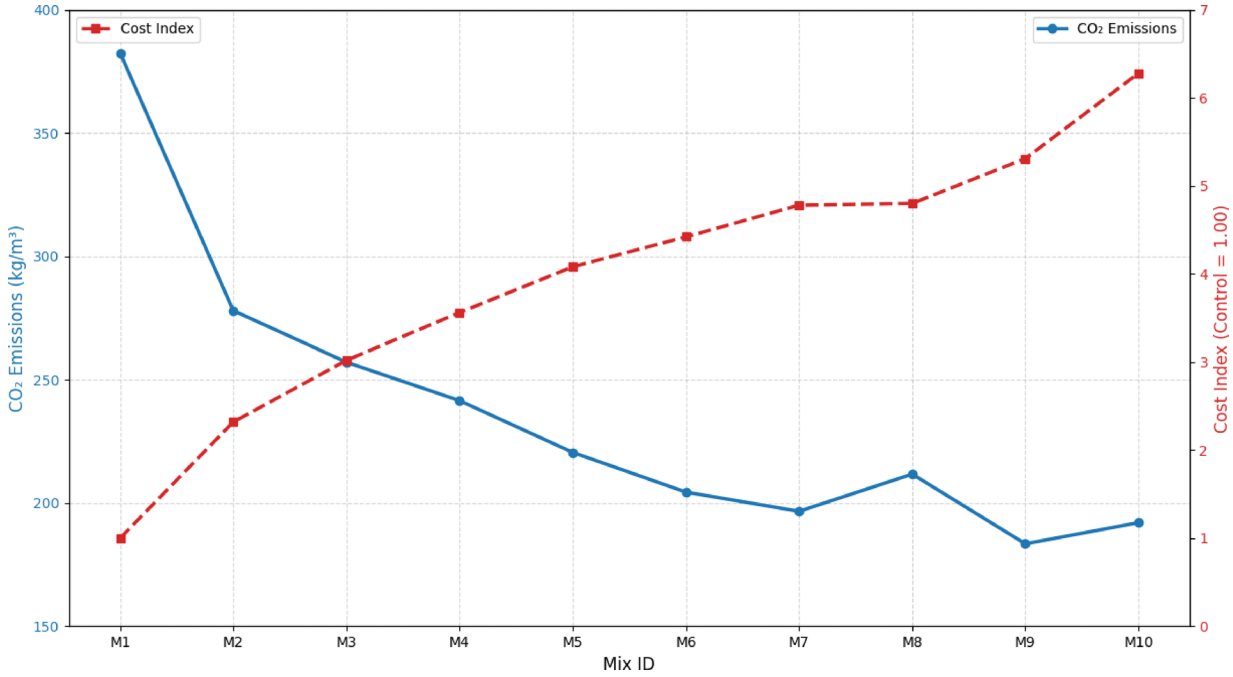

Fig. 10. Variation of CO_2 emissions (kg/m^3) and cost index (normalised to OPC control) for all concrete mixes (M1–M10), highlighting the inverse trend between embodied carbon reduction and incremental material cost as sustainable materials replace conventional cementitious content.

CO_2 footprint and cost evaluation of different concrete mixes

Figure 10 gives a detailed evaluation of embodied carbon dioxide (CO_2) emissions and a normalised cost index of all the experimented concrete batches (M1-M10). The data are proportional to the effects of cradle-to-gate, proportional to cubic metres of concrete, based on the inventory and emission factors that are outlined in the methodology section. The presented graphical synthesis shows that a step-by-step replacement of cement and the integration of high-quality carbonaceous additives can alter the amount of environmental footprint and material cost-effectiveness. As shown in Fig. 10, although the addition of SCMs has a significant impact on reducing CO_2 (up to 52%), the cost also grows in proportion to the advanced admixtures, fibre, and nano-additives. The best designs as M8, have balanced performances with a carbon footprint 45% lower and reasonable cost levels.

The most embodied CO_2 of the reference mix, M1 (100% OPC), is 382.5 kg/m^3 cement, which is expected given the established preponderance of clinker in the carbon profile of cement (0.85–0.95 kg CO_2 per kg cement). With the substitution of cement with FA and GGBS during later mixes, the emissions are reduced significantly. Between M2 and M7, CO_2 footprint drops to 277.9 kg/m^3 to 196.6 kg/m^3, which is almost half compared to the control. This tendency is due to the fact that FA and GGBS have one-tenth to one-twentieth of the emission factors of cement, and their application also alleviates CO_2 in the process of calcinations. There were earlier results of 40–60% carbon cuts in embodied concretes with high-volume SCM.

The deep, subtle reversals occur at M8, which rises to 211.7 kg/m^{3}and M9, which records the lowest footprint, 183.4 kg/m^3 and a slight recovery to 192 kg/m^3 of M10. These differences are in line with mix design modifications. M8 had been designed to have a balanced mechanical and durability property, and so it retained a little higher cementitious content of material to maintain strength and workability. M10, which was richer in natural fibre and GNPs, needed even more superplasticiser and cement to be uniform, which eventually caused a slight increment in embodied CO2. The trends confirm that, even though the SCM substitution remains the

main driver in the reduction of emissions, secondary factors, like admixtures dosage, fibre absorption and nano-additive processing, can affect the overall footprint moderately. However, each of the other blends performs well in terms of high carbon savings over traditional OPC concrete.

Unlike the decreasing CO_2 curve, the cost index remains an increasing curve along the same sequence of mix. The baseline (M1) was scaled at 1.00, and all the other mixes show gradual increments based on the cost increment of specialised materials and admixtures. M2 and M3 are 2.32 and 3.02, respectively, which are moderate SCM replacement, moderate additive usage. M4-M7 further increase this upward trend with a peak at around 4.78, and this is mostly attributed to the addition of TTCB, nano-graphene and a higher content of superplasticiser needed to restore workability that was lost due to the reduction of cement. The greatest cost values are found in M8-M10 and range from 4.80 to 6.28 because the mixes will be high-performance and high-sustainability constituents.

This increase in cost is an indication of the market reality of producing concrete sustainably. Although FA and GGBS are commonly industrial by-products and cheap, the synthesis, treatment, and distribution of graphene-based materials and treated fibres are still costly assets. In addition, high-range water reducers are associated with high-per-unit costs despite low dosages. Research proves that, although life-cycle costs can be balanced by long life and low maintenance, the initial costs of materials in such innovative blends can be three to six times higher than the traditional blends.

The plot mixture in Fig. 10 indicates that the relationship between the embodied CO_2 emission and the cost index is obviously negative: the lower the carbon emission, the higher the cost index. This non-linear trade-off is the primary focus of the sustainability framework of the study. High SCM and additive incorporation would technically make a deep decarbonisation feasible, but the economic feasibility is a limiting factor. The results indicate that M8 is the most balanced structure, the one that had a CO_2 reduction of about 45% of M1 (211.7 kg/m^3 vs. 382.5 kg/m^3) and still had a high compression strength and low permeability (RCPT). Comparatively, M9 optimises the CO_2 reduction (183.4 kg/m^3) at the cost of marginal strength and workability whereas M10 stretches the limit at unrealistic cost yet without quantifiable environmental benefit.

As the balance of performance and sustainability is common to the larger patterns in sustainable construction scholarship, optimum instead of maximum solutions are offered by optimisation. In the case of cement-intensive infrastructure, in India, the results of such studies highlight the necessity to encourage performance-constrained decarbonisation, that is, stimulate the replacement of SCM with the use of industrial by-products sourced locally and the moderate use of high-value applications of advanced carbonaceous materials.

These tendencies in Fig. 10 are consistent with life-cycle assessment (LCA) of blended concretes done worldwide, which highlights that 70–90% of the embodied CO_2 in concrete is attributed to the cement component. FA and GGBS bring about exponential sustainability return by reducing this dependency. Simultaneously, economic calculations in India and Southeast Asia demonstrate the same cost increases in using fibre and nano-modified concretes, which are caused by material and processing costs. Therefore, the cost-carbon relationship herein is reflective of the scaling impediments towards the attainment of sustainable construction materials in the real world.

When these results are combined with the mechanical and durability performance information, it is found that M8 and M9 not only lead to significant emission reductions but also show much higher levels of resistance to chloride ingress over time, which translates into extended service life. Policy and design choices that require embodied carbon limits to be taken into account, such as durability and lifecycle costs metrics, are especially dependent on such integrated outcomes.

Mechanistic interpretation and model–experiment integration

Experimental evidence suggests that synergistic hydration chemistry, pore refinement, and nanoscale reinforcement are the factors that have led to the observed performance enhancement in the FA-GGBS-TTCB-GNP blend rather than simple additive substitution. The incorporation of FA and GGBS reacts to secondary pozzolanic reactions, whereby calcium hydroxide is utilized and extra C–S–H and C–A–S–H phases are created; this is supported by the decreased peaks of attenuated portlandite in XRD spectra and denser microstructure as shown by SEM images. The resulting densification of the microstructure explains the observed increase in 28-day compressive strength and the simultaneous reduction in the values of RCPT.

TTCB, which is rich in amorphous silica, has reactive and filler effects. The small particle size facilitates high packing density, and the pozzolanic reactivity of the fine particle enhances the synthesis of gels and refines the capillary porosity. SEM indicates reduced pore connectivity and enhanced interfacial adhesion in formulations with moderate TTCB inclusion, which is accompanied by lower water uptake and chloride permeability. The reduction in permeability was therefore attributed to the shortening of diffusion pathways and a decrease in effective pore diameter, and not just the decrease in total porosity.

When properly dispersed, GNPs can serve as heterogeneous nucleation sites and microcrack-bridging reinforcements. Their inclusion accelerates the early hydration and enhances the transfer of stress within the interfacial transition zone (ITZ). However, the supra-optimal doses may produce agglomeration, hence explaining the plateau in the performance at high concentrations. The resultant increase in strength and the residual strength after being exposed to 300 °C indicate an increase in crack resistance and matrix cohesion.

The assessment of feature-importance based on the ensemble models (permutation and SHAP) identifies TTCB and binder composition as the most significant predictors. This finding is consistent with the known hydration theory, in which binder chemistry determines the kinetics of C–S–H formation, pore refinement, and transport resistance, which in turn are the main determinants of mechanical strength and durability. The relative devaluation of water content and aggregate proportions is due to the restricted ranges of the experimental values of these variables, and not to any physical insignificance.

Durability indices such as RCPT, water absorption, and sorptivity have a good correlation with microstructural refinement. Reduced chloride permeability is linked to increased gel matrix, increased chloride binding through alumina-containing phases added by GGBS, and reduced ionic mobility due to narrowed diffusion channels. As a result, the mechanical performance and impermeability are interconnected via shared microstructural pathways.

Finally, the machine-learning framework is a proxy mapping tool within the boundaries of the experimentally defined domain, and is not a replacement for mechanistic understanding. The nonlinear interactions represented by XGBoost and Random Forest are associated with the multifactorial interactions between binder chemistry, nanoscale reinforcement, and transport behaviour. The optimisation process is therefore informed by empirically supported mechanisms as opposed to mere statistical abstractions.

Machine learning models results and comparative analysis

Correlation analysis of experimental and derived variables

The correlation matrix will offer a background insight into the nature of the relationship between mix composition variables, fresh concrete parameters, and performance indicators. The cells are the Pearson correlation coefficients that are colour-coded between − 1 and + 1.

There is a strong negative relationship between the cement content and the other cementitious materials, FA and GGBS, meaning that there is deliberate substitution of binders in the dataset. Both FA and GGBS show a corresponding increase as the cement percentage reduces. The percentages of FA and GGBS in the binder show weak positive correlations with 28-day compressive strength, indicating that a partial cement replacement leads to an increase in strength in later ages and not the decrease that is expected. This activity is in line with pozzolanic and latent-hydraulic activation, which is involved in further calcium-silicate-hydraulic gel formation at 28 days[133,163,164].

On the other hand, there exists a positive relationship between cement content and CO_2 emission and cost index, which proves that the high-clinker mix is more ecological and economical. Both cost and carbon footprint have negative correlations with FA and GGBS, which makes them both environmentally and financially friendly as an alternative[133,166,167].

The values of the Rapid Chloride Penetration Test are negatively related to FA and GGBS and positively related to cement and slump. This trend reveals that the incorporation of SCM greatly hones the pore structure, thus lowering the ionic conductivity and excess cement content or the presence of too much mixing water increases the permeability. There is a low but consistent negative relationship between the compaction factor and RCPT that indicates a higher packing and lower content of void in denser mixes. The addition of natural fibres (percentage of coir as a part of binder) has a positive correlation with split-tensile strength, which is a contributing factor to its crack-bridging property[168–170]. Nevertheless, it has a negative correlation with compressive strength, where the addition of fibre after a certain optimal level may cause the discontinuity of the matrix and the appearance of an air pore. The negative relationship between the same fibre parameter and slump is also a confirmation of the lower workability associated with the absorption and entanglement of fibres[37,171,172].

The content in GNPs has a consistent positive relationship with compressive strength and tensile strength and a negative relationship with RCPT. This indicates that GNP plays a simultaneous role in mechanical improvement, as well as microstructural densification. A similar synergistic effect of it with SCMs and fibre additives can be visually observed in the clustered yellow-green areas that connect these variables and strength parameters[173,174]. Correlation magnitudes above $|0.60|$ were considered strong, while values between 0.30 and 0.60 indicate moderate association. No perfect multicollinearity ($|r| \approx 1$) was observed among predictor variables, confirming that the feature set remains suitable for tree-based ensemble modelling without dimensional reduction. The correlation trends also justify retaining binder-related variables (TTCB, SCM fraction, GNP dosage) in the surrogate models, as they explain the majority of response variance within the experimental design space.

Taken together, Fig. 11 supports three important mechanistic conclusions: the substitution of cement by a balanced mixture of FA and GGBS positively influences the late-age strengths and durability; coir fibre increases the tensile response slightly, but negatively influences the compressive strength and flow; the GNP is an omnipresent performance enhancer, positively correlated with the results of strength and durability. These correlations support the preservation of all these predictors in later machine-learning models, even though the multicollinearity between them is partial since each corresponds to physically meaningful effects on the multi-scale behaviour of the material[24,175].

Model-driven feature importance and interpretability

Figure 12 contrasts the ranking of the input variables generated by the three regressors on the three target properties and then uses SHAP to visualize the direction of the impact of the regressors. Despite the differences between the employed algorithms as to the variables they consider most informative, the patterns obtained are physically consistent and concurring with the previously described trends in the experiment. Figure 12a–c shows the relative feature importance of the CNN-LSTM, Random Forest, and XGBoost models trained on 28-day compressive strength, 28-day split tensile strength, and RCPT, whereas Fig. 12d provides the SHAP summary plots, which illustrate the direction and magnitude of each feature contribution to the model outputs (red = high feature value, blue = low). In the CNN-LM, fresh consolidation measures occupy first place in the tree; in the tree-based ensembles, TTCB and GNP take the first place in ranks; in SHAP, TTCB strengthens tensile strength but also weaken compressive strength at high dose levels, and GNP strengthens and densifies microstructures to increase strength and decrease RCPT.

The strongest predictors in the CNN -LTSA (Fig. 12a) include the fresh-state variables, which are compaction factor, fresh density, and slump, then the binder fractions (GGBS and FA). This is expected of a network that discovers relationships between co-varying inputs: at constant water-to-binder ratio, these fresh measures are

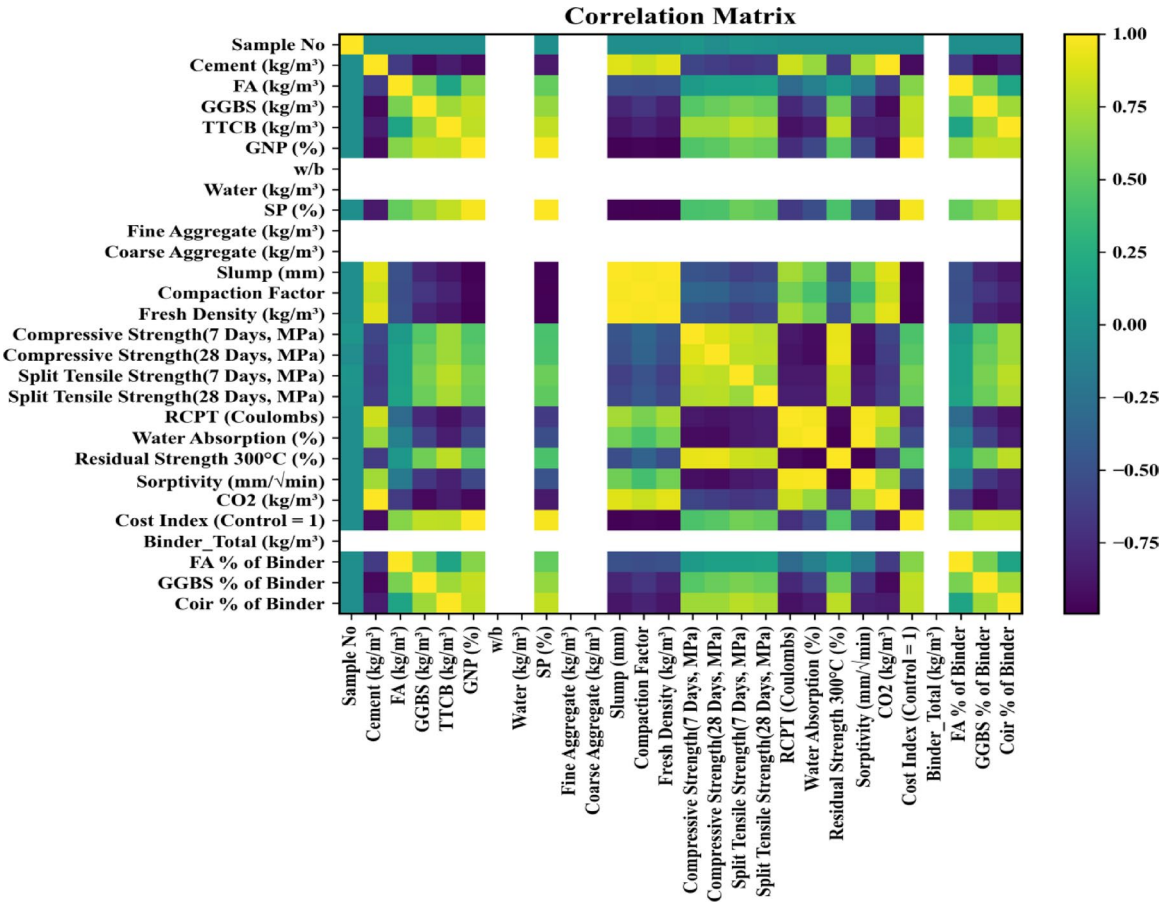

Fig. 11. Correlation matrix of all compositional, fresh, mechanical, and durability parameters for the experimental data set. Yellow indicates strong positive correlation (+1), violet indicates strong negative correlation (–1).

good proxies of paste packing and entrained air hence controlling compressive strength and permeability. Consolidation (elevated compaction factor and fresh density, diminished slump at a given water/binder proportion) in mixes that achieved higher predicted strengths and reduced RCPT values through the CNNLSTM therefore suggested the empirical correlations.

The tree based ensembles draw the focus less on the response proxies and more on the specific composition. In the Random Forecast (Fig. 12b) coir-derived micro-carbon (TTCB) is leading in the ranking on all three targets. It is most critical to split tensile strength, in which fiber bridging is the dominant mechanism, as well as compressive strength and RCPT, since TTCB has a concomitant effect on crack initiation, pore connectivity, and compaction. The second level of predictors includes FA, GGBS, superplasticizer dosage, and slump thus representing their impact on subsequent hydration and workability at old age. XGBoost (Fig. 12c) has a parallel story but places the dual-scale carbon system in a more pronounced light: TTCB does not change the location of the leading variable but instead, GNPs emerge at the highest value of the compressive strength and RCPT.

This ranking is in line with laboratory results that suggested that extremely tiny GNP dosage provides nucleation sites and crack bridging in the nanoscale, therefore, strengthening and hindering charge movement, especially when used alongside additional cementitious materials.

The directionality of feature effects is determined by SHAP summary plots (Fig. 12d). In the left panel, relating to compressive strength, high TTCB values are concentrated to the negative side of the SHAP axis indicating a net penalty at 28 days when the fiber content is high enough to render the matrix continuity ineffective or entrain air. Conversely, the trend in middle panel is the converse of that of split tensile strength: here, there is consistent positive SHAP contribution, which is the anticipated crack-bridging benefit. GNP also gives positive SHAP values with compressive strength and split tensile strength, but gives negative values with RCPT, which also supports a nucleation-and-densification mechanism that increases mechanical performance and reduces ionic transport. The SCM variables show heterogeneous interpretable patterns: intermediate replacement levels place numerous points a little too far on the positive side of compressive strength (pozzolanic or latent-hydraulic benefit of high age), but high replacement levels cause the values to become negative (dilution and a decreased hydration rate by 28 days). In the right panel, covering RCPT, the signals are unambiguous, increased values of TTCB, GGBS, FA, and compaction factor push SHAP values toward the negative direction (lower coulombs),

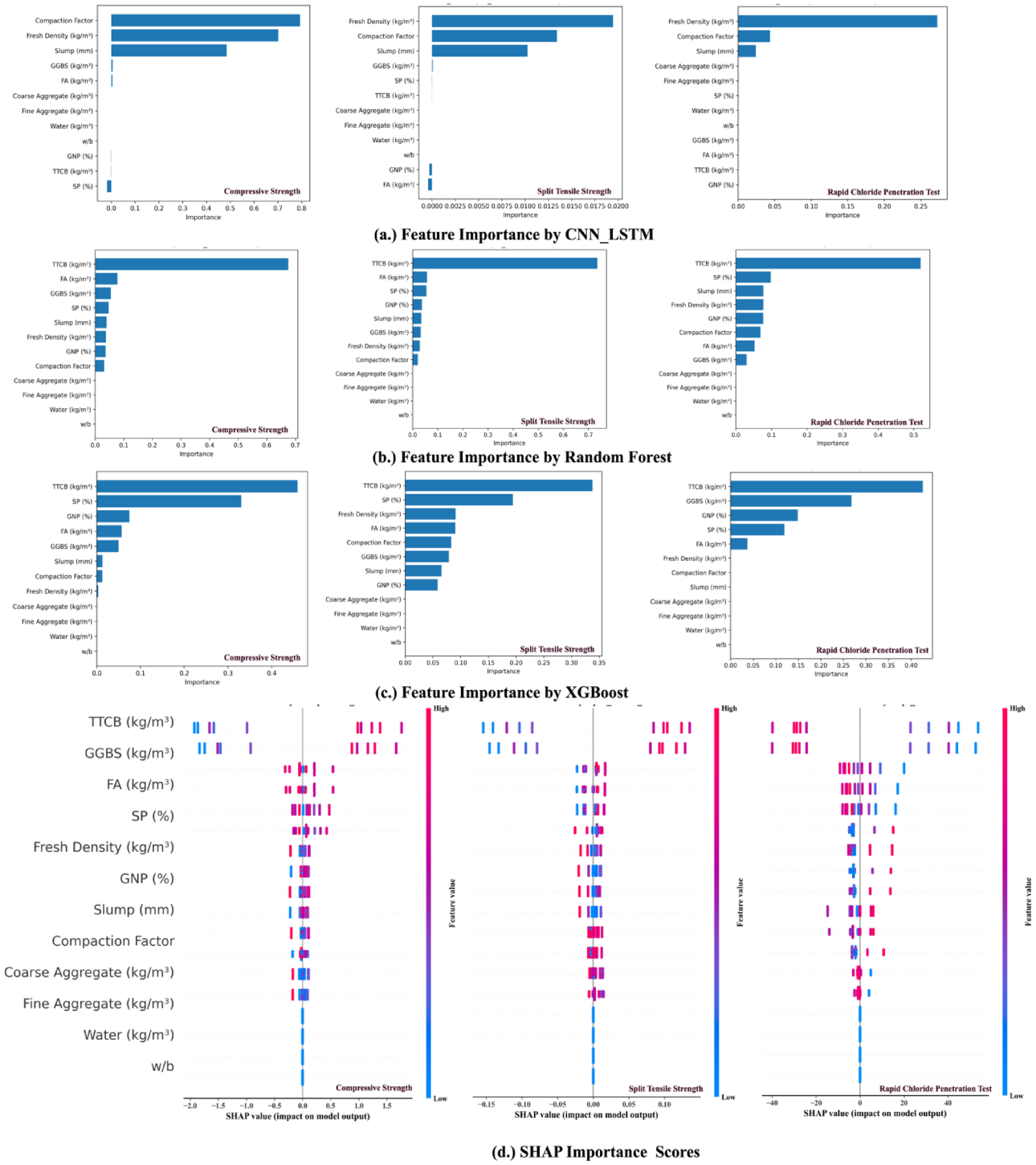

Fig. 12. (**a**, **b**, **c**) Comparative feature significance of the CNN LSTM, Random Forest, and XGBoost models trained on compressive strength at 28 days, split tensile strength at 28 days, and RCPT. (**d**) SHAP summary plots representing the direction and magnitude of individual feature contributions to the model outputs (red = high feature value, blue = low).

and higher slump values drive them towards the positive direction (higher coulombs). The fresh density acts as expected: the dense mixes produce negative values of SHAP of RCPT and positive values of strength.

The models therefore converge to a common physical meaning: consolidation quality can explain a significant percentage of the variation of the neural network, but composition, specifically fiber (TTCB), nano-reinforcement (GNP), is the most important thing to control the tree-based ensembles. The SHAP analysis proves the trade-off nature of fibers, which are known to increase tensile capacity and durability, but should be

balanced to avoid compressive strength loss. Additions of minute GNPs, which cause dense networks of hydrates and an interfacial transition zone, enhance all the three targets concomitantly.

In the current experimental programme, the major sources of variation in performance were deliberately introduced into the binder matrix, and not in aggregate grading or volumetric proportions. The aggregate skeleton was held constant across the ten mixes (M1–M10) to provide similar packing density and isolate the effects of binder on this, and GGBS and TTCB contents were varied systematically to provide insight into hydration kinetics, pore refinement, and transport resistance.

This design decision is proportional to the experimental observations: mixes containing increased reactive supplementary cementitious material contribution had a denser micro-structure and increased indicators of durability, TTCB provided further micro-filler action and pozzolanic activity, which changed the pore connectivity and refinement. Therefore, the surrogate models perceived TTCB and GGBS to be the most informative variables since they describe the highest proportion of variability among outputs (compressive and tensile strengths and RCPT) in the tested space. Therefore, the massive preponderance of TTCB and GGBS in SHAP is not inconsistent with concrete physics, but instead, it indicates that the space of factor in the experiments was binder-driven, and the highest performance gradient in the data was generated by binder chemistry and micro-structural densification.

SHAP contribution of water-related variables (water content, w/b) and aggregate parameters is relatively low, which is predetermined mainly by the controlled experimental ranges and the limitations of the design. Water and aggregate proportions were not investigated as independent design variables in the mixes, but kept within a small range to maintain desired fresh properties and batch-to-batch consistency. In cases where a predictor has a small amount of variation as compared to other variables, SHAP will automatically assign it a low value since it cannot explain a lot of the variance in the output observed in such a dataset. Furthermore, the covariation of practical batching can be as follows: small changes in water (or superplasticiser) can be occasionally made in reaction to changes in binder fineness/surface area (especially with TTCB and SCMs), and the model can tend to predict the shared predictive signal as TTCB or GGBS. This separate attribution pattern is a familiar property of the proxy learning in data-mediated models that collinearity causes and does not suggest that the influence of water and aggregates in the data is physically insignificant; rather, it suggests that in the data, much of the effect was captured in the constraints of the mix design and the collinearity-induced adjustments.

Based on this, SHAP results and optimisation performance can be viewed as interpolation-based within the experimentally validated range of M1-M10, with binder composition making up the major exploratory axis. The models are not meant to claim that there is universal feature dominance in larger concrete classes or in regimes where there is a range over w/b ratio, aggregate grading or admixture dosage that are varied orthogonally. In order to prevent over-interpretation, the trained models are directly described as surrogate approximators to decision-making in the studied design space. The addition of orthogonal variation of water content/w-b and aggregate proportions to the dataset would represent the correct direction towards enhancing generalisability and decreasing the importance redistribution in future studies due to collinearity.

Predictive accuracy and comparative evaluation

Figure 13 illustrates the parity plots between predicted and measured values for compressive strength, split tensile strength, and rapid chloride penetration test (RCPT) results across the Random Forest, XGBoost, and CNN–LSTM models. The numerical performance indices corresponding to these plots are summarised in Table 5, which consolidates the coefficient of determination (R^2), root mean square error (RMSE), and mean absolute error (MAE) for all dataset splits.

Compressive strength prediction Among the assessed algorithms, it is XGBoost, which showed the best predictive accuracy with an R^2 of 0.949 and RMSE of 0.89 MPa on the evaluation set and the nearest competitor of the Random Forest, which achieved an R^2 of 0.942 and RMSE of 0.95 MPa (see Table 5). The nonlinear correlation between 28-day compressive strength and the variables of binder composition and fibre content, as well as between 28-day compressive strength and nano-additive dosage, was developed using the two models. The prediction bands in Fig. 13a,b are close to the 45° line, and show no significant systematic error throughout the whole range of strength (43–56 MPa).

The CNN-LSTM model, in turn, performed worse with an R^2 of 0.52–0.57 and RMSE of around 3MPa and predicts that are flattened at both low and high strength levels (Fig. 13c). This can be typical of deep sequence models trained on limited tabular data with no time-dependent signal; the recurrent layers of the model are likely to overfit intermediate values and not represent the variability at the extreme values.

The excellence of the tree-based ensemble models agrees with the past studies. As an example, the Random Forest model reached an R^2 of 0.93 in estimating the compressive strength of sustainable concretes with SCMs, and XGBoost achieved an R^2 of over 0.95 in mixes with GGBS and silica-fume. These results support the observation that boosting and bagging are superior to deep neural networks in nonlinear and interdependent mix variables, especially with a sample size of less than a few hundred.

Split tensile strength prediction Once more, both ensemble models worked relatively similarly when predicting tensile-strength and XGBoost ($R^2 = 0.741$) slightly outperformed the predictive power of the Random Forest ($R^2 = 0.724$). The high density of the points around the diagonal in Fig. 13d,e shows that the fibre-dominated behaviour is learned stably. CNNLSTM fit a moderate $R^2 = 0.64$, but with regress toward the mean (Fig. 13f): low tensile values were over-fitted, and high tensile values were under-fitted. This is in line with the variability of experiments that is part and parcel of fibre reinforcement, in which micro-dispersion and interfacial bond strength add noise that cannot be reflected in the neural model that was trained on scalar mix data. The same

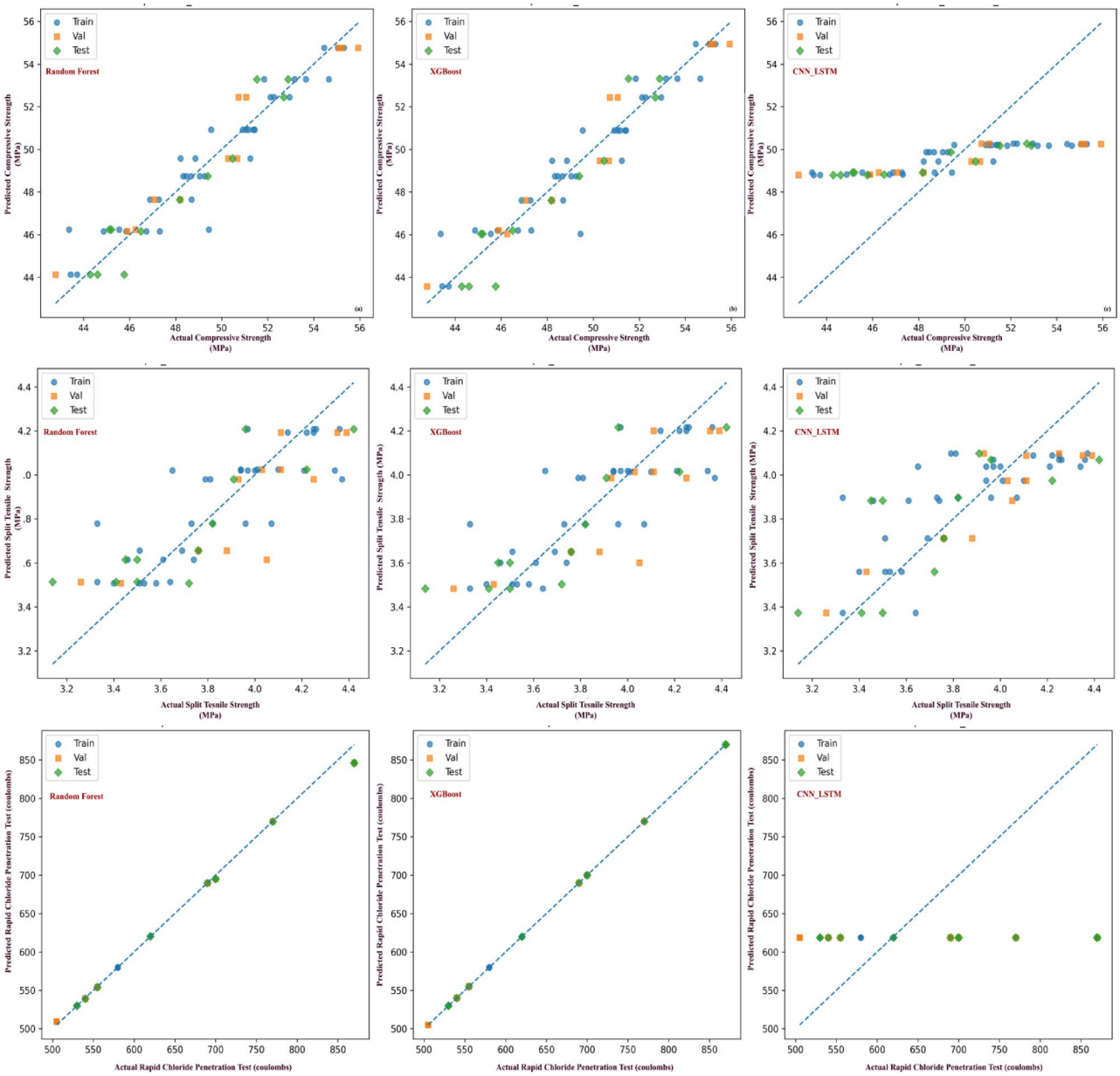

Fig. 13. Predicted versus actual results for (**a**–**c**) 28-day compressive strength, (**d**–**f**) 28-day split tensile strength, and (**g**–**i**) RCPT using Random Forest, XGBoost, and CNN–LSTM models.

trends have been reported, with CNNLSTM models of natural-fibre concretes failing to perform well compared with ensemble learners because of cases of random fibre orientation.

Rapid chloride penetration test (RCPT) prediction

In the case of RCPT, both of the ensemble models showed great accuracy. XGBoost had almost perfect prediction with $R^2 = 1.00$ in all splits and sub-Coulomb RMSE values (Table 5), whereas random forest came second ($R^2 = 0.99$, RMSE = 12 C on the test set). The high R^2 values observed for certain models, particularly XGBoost in RCPT prediction, reflect the structured nature of the experimental dataset and the bounded parameter space investigated. RCPT values in the present study exhibited strong monotonic relationships with binder composition, especially GGBS and TTCB content, which facilitated accurate nonlinear mapping by ensemble tree-based methods. However, given the limited number of distinct mix designs, such near-perfect R^2 values should be interpreted as evidence of effective interpolation within the studied domain rather than proof of broad generalisation. Ensemble models such as XGBoost can closely approximate deterministic trends in small, low-noise datasets, particularly when the experimental variables are systematically varied. To mitigate overfitting risk, model complexity was controlled through hyperparameter tuning, validation monitoring, and test-set evaluation. Nevertheless, the modelling framework remains constrained to the investigated design space, and extrapolation beyond the tested parameter ranges is not recommended.

Target property	Model type	Dataset split	Coefficient of determination (R^2)	Root mean square error	Mean absolute error
Compressive strength (28 Days, MPa)	Random Forest	Train	0.901	1.03	0.75
		Validation	0.942	0.95	0.80
		Test	0.912	0.92	0.77
	XGBoost	Train	0.903	1.02	0.71
		Validation	0.949	0.89	0.75
		Test	0.886	1.05	0.89
	CNN-LSTM	Train	0.547	2.77	2.29
		Validation	0.569	3.40	2.75
		Test	0.516	2.85	2.53
Split tensile strength (28 Days, MPa)	Random Forest	Train	0.778	0.17	0.13
		Validation	0.735	0.20	0.16
		Test	0.724	0.18	0.15
	XGBoost	Train	0.779	0.17	0.13
		Validation	0.738	0.20	0.16
		Test	0.741	0.18	0.15
	CNN-LSTM	Train	0.626	0.21	0.17
		Validation	0.752	0.16	0.14
		Test	0.636	0.24	0.20
Rapid chloride penetration test (Coulombs)	Random Forest	Train	0.997	5.92	2.35
		Validation	0.996	7.35	3.80
		Test	0.991	12.04	6.99
	XGBoost	Train	1.000	0.0009	0.0008
		Validation	1.000	0.0009	0.0007
		Test	1.000	0.0012	0.0012
	CNN-LSTM	Train	0.517	100.41	81.32
		Validation	0.598	116.23	104.37
		Test	0.512	146.23	121.67

Table 5. Performance metrics for Random Forest, XGBoost, and CNN-LSTM models predicting 28-day compressive strength, 28-day split tensile strength, and RCPT.

Reference study	Material system	Algorithm	Target property	R^2 (best model)	Remarks
[49]	Fly-ash blended concrete	Random Forest	Compressive strength	0.93	Ensemble models generalize well on small data
[187]	GGBS-silica fume concrete	XGBoost	Compressive strength	0.96	Boosted trees capture nonlinear SCM effects
[188]	Fiber-reinforced concrete	XGBoost	Chloride permeability	0.99	Outperforms deep CNN for durability indices
[189]	Natural-fiber concrete	CNN–LSTM	Tensile strength	0.60	Sequence models less effective for static inputs
Present study (2025)	FA–GGBS–Coir–GNP concrete	XGBoost	All targets (Compressive Strength 28 days, Split tensile strength 28 days and RCPT)	0.74–1.00	Superior balance of accuracy and interpretability

Table 6. Comparative summary of machine learning models for predicting mechanical and durability properties of sustainable concretes in previous literature and the present study.

Figure 13g,h indicate that both ensembles had the entire range of permeability between 500 and 850 C without any significant outliers. CNNLSTM, however, did not show any significant convergence ($R^2 = 0.51–0.60$), being excessively high in projecting the charge passed to low permeability mixes (Fig. 13i). This is once again due to the improper generalisation of this model by the features of the inputs that do not have time or space hierarchies. Such results are consistent with earlier research, in which gradient-boosting models were competitive and outperformed deep CNN architectures in predicting chloride diffusivity because they can subdivide the feature space efficiently and decrease variance without the need to have large datasets.

Comparative evaluation with previous studies Table 6 compares the model performances reported in the literature with the results of the current research to put them in context. Ensemble-based methods are systematically better than deep neural networks with the limitation of small experimental data (less than 200 samples), which supports the abovementioned hierarchy of performance: XGBoost > Random Forest > CNN–LSTM in both mechanical and durability forecasts.

All in all, ensemble learning and in particular, XGBoost proved to have the highest level of effectiveness in the prediction of the nonlinear, coupled influences of binder composition, SCM ratio, fiber dosage and nano-additive concentration on mechanical and durability properties. The relatively poor results of CNNLSTM highlight the idea that deep models require richer sequential or high-dimensional inputs to learn to make generalisations. The findings are therefore affirmative that tree-based ensembles offer a convenient and interpretable predictive framework of sustainable concrete systems, according to the current research directions of data-driven materials engineering. Compared to previous studies, the paper broadens the use of machine learning methods by simultaneously forecasting mechanical strength and durability indices in one surrogate modelling framework, avoiding the common emphasis on individual target properties. Whereas literature values of R^2 may sometimes be larger when isolated strength predictions are done, our values are always robust and multi-target, with a range of between 0.74 and 1.00, even though the size of the experimental data is small. The main improvement is not in the increased predictive accuracy, but the integration of interpretability via permutation importance and the implementation of multi-objective optimisation within a constrained design space. As a result, this work stands out from the earlier studies that treat prediction and optimisation as distinct processes. Ensemble tree-based models are proven to be more effective than deep neural architectures that require higher-dimensional or sequential inputs when applied to small and structured tabular datasets with fewer than 200 observations.

Model comparison based on independent test-set R^2 and RMSE was performed to achieve methodological transparency, and was further supported by permutation importance analysis to increase interpretability. The resultant ranking (XGBoost > Random Forest > CNN–LSTM) indicates a consistently higher performance of XGBoost in all the performance results, especially in 28-day compressive strength and durability indicators. The improved predictive power of XGBoost can be explained by the fact that it is based on the gradient-boosting architecture, and it gradually corrects the residual errors and effectively captures nonlinear relationships between binder composition and performance responses. Random Forest yielded consistent results with low variance but with a little less precision compared to XGBoost, as expected of its bagging-based averaging process.

The relatively poor performance of CNN-LSTM seems to be caused by the incompatibility between the architecture and the data. The data set is 60 observations based on ten different mix combinations, which are structured tabular inputs as opposed to time or space series. The large datasets needed to train deep neural architectures like CNN-LSTM are generally necessary to take advantage of hierarchical feature extraction and temporal memory processes. The ensemble tree-based models are more consistent with the data structure and scale within the current limited experimental domain. The feature contributions are further explained by the permutation importance analysis of 28-day compressive strength. The mean change in model score is greatest in TTCB content (kg/m^3) and coir percentage of the binder (approximately 0.33 and 0.30, respectively), which means that they have the strongest predictive power. The fly ash variables have small but significant effects, and GGBS, water content, water-binder ratio, and aggregate proportions have insignificant or almost zero permutation effect within the parameter ranges of the study. This preeminence ought to be viewed in the framework of experimental design. Binder-related variables (TTCB and SCMs proportions) were systematically controlled to investigate microstructural refinement and pozzolanic reactivity, but water, w/b, and aggregate proportions were kept within a small range to maintain workability and volumetric stability. Ensemble models, therefore, place more emphasis on binder chemistry since it explains most of the output variance in the data set. The resulting ranking and dominance of features are therefore indicative of algorithm-data compatibility and experimental form as opposed to a material hierarchy in general. The surrogate models are used as interpolation aids in the validated design space, and extrapolation outside the ranges investigated is not advisable. The predictive models are based on a small set of experimentally generated mix designs. Although systematic partitioning into training, validation and test sets was adopted and cross-validation was performed to enhance robustness, the limited size of the dataset limits statistical generalizability. Such models should therefore be viewed as surrogate approximators that are only strictly within the bounds of empirically validated parameters. It is probable that adding more orthogonally diverse mix configurations to the dataset would increase the model's robustness and external validity in future studies.

Multi-objective optimisation results and comparative analysis

Figure 14 shows the Pareto projections of the optimisation process, and Tables 7 and 8 are a summary of the performance comparison between the experimental mix and the optimised mix and the benchmark values reported in the literature. Together, they show that the surrogate and multi-objective optimisation framework based on the Random Forest (RF) is useful to balance mechanical strength, durability, carbon footprint, and cost-effectiveness of a product in a range of trade-off surfaces. Figure 14 uses the four core optimisation objectives as four axes, with each axis representing a continuous output of the optimising models, which are the trained Random Forest surrogate models. The variable f_(1_"neg_comp28") is equal to the negative of the 28-day compressive strength (MPa), a formula which enables the objective of all objectives to be minimised simultaneously during the optimisation process. This parameter is minimised, and this is the maximisation of the actual compressive strength. The second variable, f_(2_"rcpt") is an indicator of the Rapid Chloride Penetration Test (RCPT) result in Coulombs, which is a direct measure of concrete durability—the lower the result of the RCPT, the better the resistance to chloride ingress and, consequently, long-term performance. The third goal, f_(3_"CO_2"), measures the cradle-to-gate emissions of carbon dioxide per mix ($kg\ m^{-3}$), which is an environmental footprint of binder and additive selection. Lastly, f_(4_"cost") is a normalised cost index, in which the OPC control mix will be given a reference value of 1.00 in order to provide a direct comparison of relative material costs in cubic metres. Figure 14 displays the Pareto-optimal curves between pairs of these criteria, and illustrates relationships between trade-offs in sustainable concrete construction in a systematic manner. Subplot (a) examines the relationship between compressive strength and durability, reducing negative strength and RCPT to find strong-low-permeability mixtures.

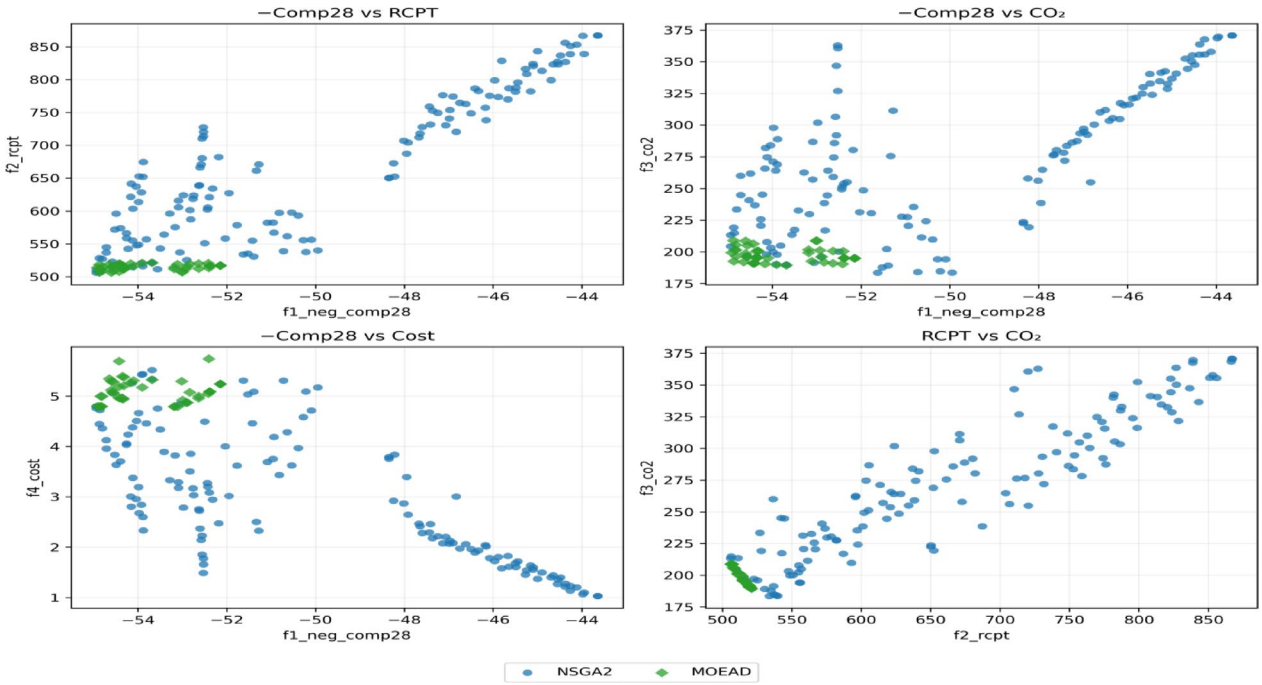

Fig. 14. Pareto projections showing the trade-offs among 28-day compressive strength (−Comp28), Rapid Chloride Penetration (RCPT), embodied CO_2 (kg m^{-3}), and cost index (control = 1.00) for NSGA-II and MOEA/D optimisation results. Each subplot represents a bi-objective front highlighting the balance between performance, durability, economy, and sustainability.

Subplot (b) plots negative strength versus embodied CO_2, and subplot (c) portrays the strength-sustainability frontier, taking the cost-mechanical performance tradeoff: cost can increase with mechanical performance. Subplot (d) discusses the RCPT—CO_2 correlation, which demonstrates the impact that binder optimisation has on the durability and environmental effects. Blue circles and green diamonds are used to represent NSGA-II solutions and MOEA/D results, respectively, in all subplots. The fact that the two datasets are almost identical when using all four views implies that both algorithms came to an almost similar set of Pareto fronts and only differ in the local weighting of each objective. Tables 7 and 8 also keep the same notations and report 28-day compressive strength, RCPT, embodied CO_2 and normalised cost index. The consistency through figures and tables provides direct quantitative cross-comparison of the experimental validation, the predictions of the surrogate model, and the optimisation results- a unified foundation of the multi-objective behaviour interpretation of the designed mixes.

Table 7 shows the most significant findings of the experimental control mix, machine-learning-predicted optimum, and compromising solutions with the use of NSGA-II and MOEA/D. The experimental control (baseline) had compressive strength of 52.21 MPa with 554.9 C and embedded CO_2 of 204.4 kg m^{-3}, and the cost index of 4.42. These are the laboratory-tested values, which serve as the reference value upon which the results of computational optimisation are compared.

Referring to the RF-surrogate and NSGA-II- optimised combination (54.39 MPa, 573.82 C, 236.73 kg CO_2 m^{-3}, cost 3.70) showed a greater mechanical strength and cost-efficiency, though with a relatively high increment of carbon emissions. This increment can be explained by a slightly increased cement fraction used to uphold cohesion and workability at the optimum water-to-binder ratio (w/b = 0.35) and lower dosage of superplasticiser of about (~ 3.5%) and 800 kg m^{-3} fine aggregate.

MOEA/D solution produced the most balanced sustainability profile with a compressive strength of 54.86 MPa, an RCPT of 518.23 C, 192.46 kg CO_2 m^{-3}, and an index cost of 4.79. The synergistic loss of the ternary binder system, which is FA (approximately 71.5 kg m^{-3}), GGBS (approximately 68. kg m^{-3}), and TTCB (approximately kg m^{-3}), together with about 0.14% addition of GNPs, makes it more resistant to chloride. The small increment in the cost is compensated with significant decreases in the permeability and embodied carbon.

The non-linear and competitive nature of these objectives is highlighted by the Pareto fronts in Fig. 14. The correlation between the compressive strength and the negative component of the compressive strength is negative, indicating that, at a specific point, the increase of compressive strength can lead to a decrease in chloride resistance and the RCPT–CO_2 plane demonstrates the definite positive dependence the mixes with lower RCPT values have lower CO_2 emissions and binder fineness is a strong determinant. The Comp28 versus Cost projection shows that there is a practical constraint of cost minimisation, beyond which structural performance must start to decline, which means that optimisation should be multi-objective and not single-objective.

Table 8 puts the current optimisation results in comparison with existing literature. A DNN + MOPSO hybrid was used in Tipu et al.[49] to attain compressive strengths up to 50 MPa using 25% less cement at a cost of 15% lower. Wu et al.[188] claimed the CO_2 and cost-saving of 23–60% and 16–36%, respectively, in geopolymer concretes

GNP (%)	TTCB (kg/m^3)	FA (kg/m^3)	GGBS (kg/m^3)	w/b	Water (kg/m^3)	SP (%)	Fine aggregate (kg/m^3)	Coarse aggregate (kg/m^3)	Slump (mm)	Compaction factor	Fresh density (kg/m^3)	Compressive28_pred	RCPT_pred	CO2_pred	CostIndex_pred
0.139	94.382	71.468	68.343	0.350	157.500	3.521	800.000	1000.000	58.579	0.952	2463.718	54.391	573.817	236.734	3.703
0.200	85.000	45.000	90.000	0.350	157.500	3.200	800.000	1000.000	49.000	0.900	2430.000	52.209	554.917	204.436	4.421

Table 7. Experimental and optimised results from NSGA-II and MOEA/D for sustainable concrete mixes.

Mix type/reference	28 d strength (MPa)	RCPT (Coulombs)	CO_2 (kg/m^3)	Cost Index (Control = 1)	Remarks
Present Study—Experimental (Control)	52.21	554.92	204.44	4.42	Laboratory-verified control mix (baseline)
Present study—ML-Optimized	54.39	573.82	236.73	3.70	ML-predicted optimum mix (balanced objectives)
Present study—NSGA-II	54.39	573.82	236.73	3.70	NSGA-II compromise solution (near-optimal strength)
Present study—MOEA/D	54.86	518.23	192.46	4.79	MOEA/D compromise (best durability and CO_2 trade-off)
Tipu et al. [49]	≥ 50.0	–	–	0.85 (–15% vs. control)	DNN + MOPSO: > 50 MPa via 25% cement↓, cost–15%
Gu et al.[187]	–	–	–	–	NSGA-II for recycled concrete (multi-objective: strength, cost, carbon)
Wu et al.[188]	–	–	– 23 to – 60%↓	– 16 to – 36%↓	AutoML + Pareto (geopolymer concrete): balanced strength, cost, CO_2
Wang et al.[189]	–	–	–	–	NSGA-III/MOEA for UHPC: Pareto trade-offs (strength, flow, cost, sustainability)

Table 8. Comparative analysis of optimised concrete performance against recent literature on multi-objective optimisation of cementitious systems.

using Pareto optima, and Gu et al.[187] and Wang et al.[189] established that the NSGA-II and MOEA models could efficiently trade-off performance and sustainability in recycled and ultra-high-performance concretes. Comparatively, the MOEA/D solution of the present study (192 kg CO_2 m^{-3}, 518 C, 54.9 MPa) demonstrates similar performance, with about 6% reduction in the CO_2 concentration, and improved chloride resistance at a relatively low increment in cost when compared to the control. The NSGA II mix confirms the results of Gu et al.[187], which certifies its reliability to determine low-cost, high-strength solutions with feasible mix constraints. The main difference between the present work, though, lies in combining experimental validation, AI-based surrogate modelling, and evolutionary optimisation into a full iterative cycle, which strengthens the predictive accuracy as well as physical verifiability. The strong match between optimised predictions and measured data confirms the strength of the surrogate-based optimisation framework.

The combined results validate the fact that hybrid binder systems made using FA, GGBS and thermally-treated coir biomass can significantly reduce embodied carbon, which is usually less than 200 kg m^{-3} but, nevertheless, strength and durability are not compromised or reduced. This is a saving of about half of the usual OPC-based concrete. However, the cost and material complexity of such decarbonisation is bound to be added. Both NSGA-II and MOEA/D algorithms study this balance in the following manner: NSGA-II is cost-efficient and buildable, and MOEA/D is environmentally and durability performance focused. The corresponding measures of normalised distances (0.66 and 0.80) verify that both result in Pareto-optimal solutions in the design space, which are close to equilibrium.

Practically, these findings explain that an approach to sustainable and high-performance concrete design should not aim to achieve just the best but must act within a multi-objective performance range that optimises mechanical integrity, service life, and embodied carbon. The combined predictive-optimisation content that is justified in this paper offers a reproducible and evidence-based framework with which to design next-generation concretes at both structural and sustainability requirements without the necessity of conducting extensive laboratory experimentation.

Conclusion

This study develops a combined experimental-computational model of the sustainable high-performance concrete design, using a hybrid low-carbon binder, which includes fly ash (FA), ground granulated blast-furnace slag (GGBS), thermally treated coir biomass (TTCB) and graphene nanoplatelets (GNPs). Instead of considering material development, modelling and optimisation as separate activities, the work connects multiscale material engineering with interpretable surrogate modelling and constrained multi-objective optimisation in a strictly defined laboratory design space. The results indicate that sustainability goals, compressive strength, durability, embodied CO_2 and cost can be explored systematically using data-driven exploration without losing mechanistic foundations. The major contributions and findings are:

- *Hybrid binder innovation* Multifaceted system of industrial by-products, bio-derived pozzolan and nanomaterials experimental validation. The optimised mixture achieved a compressive strength of about 55 MPa, RCPT value of about 505 C and a decrease of about 45% of embodied CO_2 in comparison with ordinary Portland cement, which was supported by microstructural densification and increased calcium-silicate-hydrate networks.
- *Functional bio-pozzolan development* Evidence that thermally treated coir biomass can serve simultaneously as an active supplementary cementitious material and as a dispersion-enhancing modifier in hybrid binders to enhance pore refinement and interfacial enhancement.
- *Interpretable surrogate modelling* Tree-based ensemble models, especially XGBoost, provided strong multi-target predictions of 28-day compressive strength, tensile strength, and RCPT on a small experimental dataset. The importance of features analysis showed that the binder chemistry is the most important determinant of performance, which reflects the experimental control used.

- *Constrained multi-objective optimisation* The integration of surrogate models with NSGA-II and MOEA/D allowed exploration of explicit trade-offs between strength, durability, carbon footprint, and cost. The framework shows that sustainable mix design can be developed beyond empirical iteration and proceed towards structured optimisation.

The modelling framework has been narrowed down intentionally to a validated exploration tool in the experimentally constrained domain. Future studies ought to move the validation to independent data, explore long-term durability processes, and conduct pilot-scale implementation to augment external generalizability.

Limitations

Although the current study has promising results, there are a number of limitations that are worth mentioning. In the first place, 60 observations were used to model, which is equal to ten different mix designs; therefore, the statistical generalisability of the studies on the composition range, which is tested, is limited. Second, the durability test was limited to the accelerated indicators, namely, RCPT, water absorption, sorptivity, and residual strength at 300 °C, and it does not consider the long-term degradation processes. Third, the surrogate models are limited to the design space that is defined in the experiments and thus ought to be viewed as interpolation instruments, but not as predictors that are applicable across the board. Lastly, even though the quality of nanoparticle dispersion was experimentally regulated, it was not measured with the help of sophisticated dispersion characterisation methods.

Future research directions

The framework should be expanded in future studies to include long-term durability processes, such as carbonation, sulfate attack, freeze–thaw resistance, and chloride diffusion modelling under realistic exposure environments. An increase in the number of experiments using orthogonally varied water-to-binder ratios and aggregate parameters would improve statistical strength and generalisability of the model. Mechanistic insight can be further reinforced by integration of quantitative pore-structure characterisation, i.e. MIP or micro-CT. Lastly, the optimisation framework would be more practically applicable with validation using independent external datasets or field-scale tests.

Data availability

Data are not publicly available but are available from the corresponding author on reasonable request.

Received: 15 January 2026; Accepted: 16 March 2026
Published online: 30 March 2026

References

1. Olsson, J. A., Miller, S. A. & Alexander, M. Near-term pathways for decarbonizing global concrete production. *Nat. Commun.* https://doi.org/10.1038/s41467-023-40302-0 (2023).
2. Nilimaa, J. Smart materials and technologies for sustainable concrete construction. *Dev. Built Environ.* **15**, 100177. https://doi.org/10.1016/j.dibe.2023.100177 (2023).
3. Shanks, W. et al. How much cement can we do without? Lessons from cement material flows in the UK. *Resour. Conserv. Recycl.* **141**, 441. https://doi.org/10.1016/j.resconrec.2018.11.002 (2018).
4. Ahmad, J. et al. A comprehensive review on the ground granulated blast furnace slag (GGBS) in concrete production. *Sustainability* **14**, 8783. https://doi.org/10.3390/su14148783 (2022).
5. Rahman, M. A. & Lu, Y. EcoBlendNet: A physics-informed neural network for optimizing supplementary material replacement to reduce the carbon footprint during cement hydration. *J. Clean. Prod.* **464**, 142777. https://doi.org/10.1016/j.jclepro.2024.142777 (2024).
6. Juenger, M., Snellings, R. & Bernal, S. A. Supplementary cementitious materials: New sources, characterization, and performance insights. *Cem. Concr. Res.* **122**, 257. https://doi.org/10.1016/j.cemconres.2019.05.008 (2019).
7. Aylas-Paredes, B. K., Bhat, R., Neithalath, N. & Kumar, A. Advancing the use of supplementary cementitious materials: A novel framework for quantitative reactivity estimation. (2025). https://doi.org/10.5703/1288284317960
8. Aziz, A. et al. Enhancing sustainability in self-compacting concrete by optimizing blended supplementary cementitious materials. *Sci. Rep.* https://doi.org/10.1038/s41598-024-62499-w (2024).
9. Shubbar, A. et al. The development of a low carbon binder produced from the ternary blending of cement, ground granulated blast furnace slag and high calcium fly ash: An experimental and statistical approach. *Constr. Build. Mater.* **187**, 1051. https://doi.org/10.1016/j.conbuildmat.2018.08.021 (2018).
10. Sanjuán, M. Á., Menéndez, E. & Recino, H. Mechanical performance of Portland cement, coarse silica fume, and limestone (PC-SF-LS) ternary Portland cements. *Materials* **15**, 2933. https://doi.org/10.3390/ma15082933 (2022).
11. Rolandi, A. C. et al. Unlocking sustainable power: Advances in aqueous processing and water-soluble binders for NMC cathodes in high-voltage Li-ion batteries. *RSC Sustain.* **2**, 2125. https://doi.org/10.1039/d4su00098f (2024).
12. Tian, Q., Yang, H., Li, Q., Yu, X. & Li, H. Design of functional binders for high-specific-energy lithium-ion batteries: From molecular structure to electrode properties. *Ind. Chem. Mater.* **2**, 191. https://doi.org/10.1039/d3im00089c (2023).
13. Dobryden, I., Montanari, C., Bhattacharjya, D., Aydin, J. & Ahniyaz, A. Bio-based binder development for lithium-ion batteries. *Materials* **16**, 5553. https://doi.org/10.3390/ma16165553 (2023).
14. Barbhuiya, S., Das, B. B., Adak, D., Kapoor, K. & Tabish, M. Low carbon concrete: Advancements, challenges and future directions in sustainable construction. *Discov. Concr. Cement* https://doi.org/10.1007/s44416-025-00002-y (2025).
15. Barros, L. B., Knockaert, M. & Filho, J. R. T. Towards a more sustainable construction industry: Bridging the gap between technical progress and commercialization of self-healing concrete. *Constr. Build. Mater.* **403**, 133094. https://doi.org/10.1016/j.conbuildmat.2023.133094 (2023).
16. Ottosen, L. M. *Innovations in Building and Bridge Engineering Associated with Circular Economy* (CRC Press, 2024). https://doi.org/10.1201/9781003483755-8.
17. Kashyap, V. S., Sancheti, G., Yadav, J. S. & Agrawal, U. S. Smart sustainable concrete: Enhancing the strength and durability with nano silica. *Smart Constr. Sustain. Cities* https://doi.org/10.1007/s44268-023-00023-1 (2023).
18. Maries, A., Hills, C. D. & Carey, P. J. Low-carbon CO_2-activated self-pulverizing cement for sustainable concrete construction. *J. Mater. Civ. Eng.* https://doi.org/10.1061/(asce)mt.1943-5533.0003370 (2020).

19. Chousidis, N. Impact of steel fibers and carbon nanotubes on the strength and quality of cementitious composites. *Constr. Mater.* **5**, 23. https://doi.org/10.3390/constrmater5020023 (2025).
20. Du, S., Wu, J., AlShareedah, O. & Shi, X. Nanotechnology in cement-based materials: A review of durability, modeling, and advanced characterization. *Nanomaterials* **9**, 1213. https://doi.org/10.3390/nano9091213 (2019).
21. Murthi, P., Poongodi, K., Gobinath, R. & Saravanan, R. Evaluation of material performance of coir fibre reinforced quaternary blended concrete. *IOP Conf. Ser. Mater. Sci. Eng.* https://doi.org/10.1088/1757-899x/872/1/012133 (2020).
22. Ali, T. et al. Optimizing recycled aggregate concrete performance with chemically and mechanically activated fly ash in combination with coconut fiber. *Sci. Rep.* https://doi.org/10.1038/s41598-025-92227-x (2025).
23. Boston-Osoteo, M. R., Pontillo, A. J. B. & Apdohan, A. G. Utilization and evaluation of rice husk ash and coconut shell ash as partial cement replacement for concrete hollow blocks production. in *Proceedings of International Exchange and Innovation Conference on Engineering & Sciences (IEICES)*, Kyushu University, 2022: p. 360. https://doi.org/10.5109/5909117.
24. Margas, M., Danoglidis, P. A. & Konsta-Gdoutos, M. S. The role of graphene-based nanomaterials in enhancing resiliency and ductility in engineered. *Concrete* https://doi.org/10.5703/1288284318029 (2025).
25. Lamastra, F. R. et al. Toward a better understanding of multifunctional cement-based materials: The impact of graphite nanoplatelets (GNPs). *Ceram. Int.* **47**, 20019. https://doi.org/10.1016/j.ceramint.2021.04.012 (2021).
26. Gao, Y. et al. High-performance cementitious composites containing nanostructured carbon additives made from charred coal fines. *Res. Square* https://doi.org/10.21203/rs.3.rs-3693852/v1 (2023).
27. Bhojaraju, C., Mousavi, S. S., Brial, V., Mare, M. D. & Ouellet-Plamondon, C. Fresh and hardened properties of GGBS-contained cementitious composites using graphene and graphene oxide. *Constr. Build. Mater.* **300**, 123902. https://doi.org/10.1016/j.conbuildmat.2021.123902 (2021).
28. Li, Z., Fei, M., Huyan, C. & Shi, X. Nano-engineered, fly ash-based geopolymer composites: An overview. *Resour. Conserv. Recycl.* **168**, 105334. https://doi.org/10.1016/j.resconrec.2020.105334 (2020).
29. Lamastra, F. R. et al. An insight into durability, electrical properties and thermal behavior of cementitious materials engineered with graphene oxide: Does the oxidation degree matter?. *Nanomaterials* **13**, 726. https://doi.org/10.3390/nano13040726 (2023).
30. Ying, J. & Xi, X. Microstructure and chloride diffusion properties of hardened fly ash cement paste with three-dimensional graphene. *Int. J. Concr. Struct. Mater.* https://doi.org/10.1186/s40069-021-00494-5 (2022).
31. Kumar, R. P., Ganesh, B., Bai, S., Narendra, B. K. & Venkateswaran, N. Industrial wastes as alternative materials to fine aggregates in triple blend self compacting concrete—A sustainable technological solution. *IOP Conf. Ser. Earth Environ. Sci.* https://doi.org/10.1088/1755-1315/268/1/012133 (2019).
32. Sua-iam, G., Sokrai, P. & Makul, N. Novel ternary blends of Type 1 Portland cement, residual rice husk ash, and limestone powder to improve the properties of self-compacting concrete. *Constr. Build. Mater.* **125**, 1028. https://doi.org/10.1016/j.conbuildmat.2016.09.002 (2016).
33. Mirindi, D. et al. Prediction of flexural and split tensile strength of waste glass-concrete composite using machine learning algorithms. *Green Technol. Sustain.* **4**, 100275. https://doi.org/10.1016/j.grets.2025.100275 (2025).
34. Tak, M., Feng, Y. & Mahgoub, M. Advanced machine learning techniques for predicting concrete compressive strength. *Infrastructures* **10**, 26. https://doi.org/10.3390/infrastructures10020026 (2025).
35. Poudel, S. et al. Artificial intelligence-based ensemble models with GUI for predicting the compressive strength of waste glass concrete. *Green Technol. Sustain.* **4**, 100307. https://doi.org/10.1016/j.grets.2025.100307 (2025).
36. Poudel, S. et al. Prediction of compressive strength of sustainable concrete incorporating waste glass powder using machine learning algorithms. *Sustainability* **17**, 4624. https://doi.org/10.3390/su17104624 (2025).
37. Fawad, M. et al. Indirect prediction of graphene nanoplatelets-reinforced cementitious composites compressive strength by using machine learning approaches. *Sci. Rep.* **14**, 14252. https://doi.org/10.1038/s41598-024-64204-3 (2024).
38. Zhang, Y., Kim, T., Castel, A. & Xu, T. Thermal cracking in high volume of fly ash and GGBFS concrete. *Int. J. Concr. Struct. Mater.* https://doi.org/10.1186/s40069-023-00626-z (2023).
39. Mehta, A., Siddique, R., Ozbakkaloglu, T., Shaikh, F. U. A. & Belarbi, R. Fly ash and ground granulated blast furnace slag-based alkali-activated concrete: Mechanical, transport and microstructural properties. *Constr. Build. Mater.* **257**, 119548. https://doi.org/10.1016/j.conbuildmat.2020.119548 (2020).
40. Mostofinejad, D., Nasrollahi, M., Bahmani, H., Zajshoor, Z. & Sadeghi, M. Enhancing concrete strength and durability of normal and high-strength concrete: Exploring combined effects of optimized silica fume and slag. *Iran. J. Sci. Technol. Trans. Civ. Eng.* **49**, 2309. https://doi.org/10.1007/s40996-024-01573-9 (2024).
41. Ashokan, A., Rajendran, S. & Dhairiyasamy, R. A comprehensive study on enhancing of the mechanical properties of steel fiber-reinforced concrete through nano-silica integration. *Sci. Rep.* https://doi.org/10.1038/s41598-023-47475-0 (2023).
42. He, F., Biolzi, L. & Carvelli, V. Effects of elevated temperature and water re-curing on fracture process of hybrid fiber reinforced concretes. *Eng. Fract. Mech.* **276**, 108885. https://doi.org/10.1016/j.engfracmech.2022.108885 (2022).
43. Dziomdziora, P. & Smarzewski, P. Effect of hybrid fiber compositions on mechanical properties and durability of ultra-high-performance concrete: A comprehensive review. *Materials* **18**, 2426. https://doi.org/10.3390/ma18112426 (2025).
44. Tahwia, A. M., Mokhles, M. & Elemam, W. E. Optimizing characteristics of high-performance concrete incorporating hybrid polypropylene fibers. *Innov. Infrastruct. Solut.* https://doi.org/10.1007/s41062-023-01268-6 (2023).
45. Sahani, A. K., Samanta, A. K. & Singharoy, D. K. Mechanical behaviour of fire-exposed fibre-reinforced sustainable concrete. *J. Struct. Fire Eng.* https://doi.org/10.1108/jsfe-11-2018-0035 (2019).
46. Amin, M. N. & Khan, K. Mechanical performance of high-strength sustainable concrete under fire incorporating locally available volcanic ash in Central Harrat Rahat, Saudi Arabia. *Materials* **14**, 21. https://doi.org/10.3390/ma14010021 (2020).
47. Vedrtnam, A., Bedon, C. & Barluenga, G. Study on the compressive behaviour of sustainable cement-based composites under one-hour of direct flame exposure. *Sustainability* **12**, 10548. https://doi.org/10.3390/su122410548 (2020).
48. Nguyen, K. L., Uddin, M. & Pham, T. M. Generative artificial intelligence and optimisation framework for concrete mixture design with low cost and embodied carbon dioxide. *Constr. Build. Mater.* **451**, 138836. https://doi.org/10.1016/j.conbuildmat.2024.138836 (2024).
49. Tipu, R. K., Rathi, P., Pandya, K. S. & Panchal, V. R. Optimizing sustainable blended concrete mixes using deep learning and multi-objective optimization. *Sci. Rep.* https://doi.org/10.1038/s41598-025-00943-1 (2025).
50. Rajczakowska, M., Szeląg, M., Habermehl-Cwirzen, K., Hedlund, H. & Ćwirzeń, A. Interpretable machine learning for prediction of post-fire self-healing of concrete. *Materials* **16**, 1273. https://doi.org/10.3390/ma16031273 (2023).
51. Aylas-Paredes, B. K. et al. Data driven design of ultra high performance concrete prospects and application. *Sci. Rep.* https://doi.org/10.1038/s41598-025-94484-2 (2025).
52. Gerhard, D., Wolf, M., Huxoll, J. & Vogt, O. Digital twin representations of concrete modules in an interdisciplinary context of construction and manufacturing industry. in: *IFIP Advances in Information and Communication Technology*, Springer Science+Business Media, 2020: p. 101. https://doi.org/10.1007/978-3-030-62807-9_9.
53. Dahlan, A. S. Impact of nanotechnology on high performance cement and concrete. *J. Mol. Struct.* **1223**, 128896. https://doi.org/10.1016/j.molstruc.2020.128896 (2020).
54. Saleem, H., Zaidi, S. J. & Alnuaimi, N. A. Recent advancements in the nanomaterial application in concrete and its ecological impact. *Materials* **14**, 6387. https://doi.org/10.3390/ma14216387 (2021).

55. Tanimola, J. O. & Efe, S. Recent advances in nano-modified concrete: Enhancing durability, strength, and sustainability through nano silica (nS) and nano titanium (nT) incorporation. *Appl. Eng. Sci.* **19**, 100189. https://doi.org/10.1016/j.apples.2024.100189 (2024).
56. Feng, G. et al. Physical chemical characterization of thermally and aqueous solution treated maize stalk stem ash and its potential use in a cementing system. *Energy Sour. A. Util. Environ. Eff.* **42**, 930. https://doi.org/10.1080/15567036.2019.1602206 (2019).
57. Šupić, S., Malešev, M., Радоњанин, B., Bulatović, V. & Milović, T. Reactivity and pozzolanic properties of biomass ashes generated by Wheat and Soybean straw combustion. *Materials* **14**, 1004. https://doi.org/10.3390/ma14041004 (2021).
58. Chindaprasirt, P. & Rattanasak, U. Eco-production of silica from sugarcane bagasse ash for use as a photochromic pigment filler. *Sci. Rep.* https://doi.org/10.1038/s41598-020-66885-y (2020).
59. Wijesekara, D. A., Sargent, P., Hughes, D. & Ennis, C. J. Sintered bottom and vitrified silica ashes derived from incinerated municipal solid waste as circular economy-friendly partial replacements for cement in mortars. *Waste Biomass Valor.* **15**, 2735. https://doi.org/10.1007/s12649-023-02347-6 (2023).
60. Vinnichenko, V., Riazanov, A. A. & Riazanov, A. Influence of organic matters on the calcium carbonate decarbonization process. *Mater. Sci. Forum.* **968**, 35. https://doi.org/10.4028/www.scientific.net/msf.968.35 (2019).
61. Delgado-Moreno, L. et al. New insights into the efficient removal of emerging contaminants by biochars and hydrochars derived from olive oil wastes. *Sci. Total Environ.* **752**, 141838. https://doi.org/10.1016/j.scitotenv.2020.141838 (2020).
62. Maneechakr, P. & Karnjanakom, S. Environmental surface chemistries and adsorption behaviors of metal cations (Fe^{3+}, Fe^{2+}, Ca^{2+} and Zn^{2+}) on manganese dioxide-modified green biochar. *RSC Adv.* **9**, 24074. https://doi.org/10.1039/c9ra03112j (2019).
63. Sētiņa, J., Gabrene, A., Juhņeviča, I. & Ose, I. Effect of siliceous pozzolanic additives on the hydration process of cement. *Key Eng. Mater.* **604**, 110. https://doi.org/10.4028/www.scientific.net/kem.604.110 (2014).
64. Kramar, S. & Ducman, V. Evaluation of ash pozzolanic activity by means of the strength activity index test, Frattini test and DTA/TG analysis. *Tehnicki Vjesnik Tech. Gazette* https://doi.org/10.17559/tv-20171203193229 (2018).
65. Baki, V. A., Ke, X., Heath, A., Calabria-Holley, J. & Terzi, C. Improving the pozzolanic reactivity of clay, marl and obsidian through mechanochemical or thermal activation. *Mater. Struct.* https://doi.org/10.1617/s11527-023-02280-z (2023).
66. Sturm, P., Gluth, G. J. G., Jäger, C., Brouwers, H. J. H. & Kühne, H. Sulfuric acid resistance of one-part alkali-activated mortars. *Cem. Concr. Res.* **109**, 54. https://doi.org/10.1016/j.cemconres.2018.04.009 (2018).
67. León-Jiménez, A. et al. Compositional and structural analysis of engineered stones and inorganic particles in silicotic nodules of exposed workers. *Particle Fibre Toxicol.* https://doi.org/10.1186/s12989-021-00434-x (2021).
68. Jamwal, A. et al. Sustainable concrete production: Utilizing cow dung ash and corn stalk ash as eco-friendly alternatives. *Civ. Eng. J.* **10**, 21. https://doi.org/10.28991/cej-sp2024-010-02 (2024).
69. Pinheiro, V. D. et al. Pozzolanic potential of calcined clays at medium temperature as supplementary cementitious material. *Sustainability* **16**, 7508. https://doi.org/10.3390/su16177508 (2024).
70. Brial, V., Tran, H., Sorelli, L., Conciatori, D. & Ouellet-Plamondon, C. Improvement of treated spent pot lining reactivity in cementitious material by calcination. *Dev. Built Environ.* **12**, 100098. https://doi.org/10.1016/j.dibe.2022.100098 (2022).
71. Lindgreen, H., Geiker, M. R., Krøyer, H., Springer, N. & Skibsted, J. Microstructure engineering of Portland cement pastes and mortars through addition of ultrafine layer silicates. *Cem. Concr. Compos.* **30**, 686. https://doi.org/10.1016/j.cemconcomp.2008.05.003 (2008).
72. Zhao, Y.-C. et al. Investigation on roles of packing density and water film thickness in synergistic effects of slag and silica fume. *Materials* **15**, 8978. https://doi.org/10.3390/ma15248978 (2022).
73. Ibrahim, R., Ahmad, S. S. E., Ghazal, A. I., Al-kroom, H. & Elrahman, M. A. Studying the role of fine materials characteristics on the packing density and rheological properties of blended cement pastes. *Appl. Rheol.* https://doi.org/10.1515/arh-2025-0035 (2025).
74. Xiao, H. et al. Graphene-iron ore tailings-based cementitious composites with high early flexural strength. *Materials* **16**, 327. https://doi.org/10.3390/ma16010327 (2022).
75. Chintalapudi, K. & Pannem, R. M. R. Enhanced strength, microstructure, and thermal properties of Portland Pozzolana fly ash-based cement composites by reinforcing graphene oxide nanosheets. *J. Build. Eng.* **42**, 102521. https://doi.org/10.1016/j.jobe.2021.102521 (2021).
76. Ranjbar, N., Mehrali, M., Mehrali, M., Alengaram, U. J. & Jumaat, M. Z. Graphene nanoplatelet-fly ash based geopolymer composites. *Cem. Concr. Res.* **76**, 222. https://doi.org/10.1016/j.cemconres.2015.06.003 (2015).
77. Monasterio-Guillot, L. et al. CO2 sequestration and simultaneous zeolite production by carbonation of coal fly ash: Impact on the trapping of toxic elements. *J. CO2 Util.* **40**, 101263. https://doi.org/10.1016/j.jcou.2020.101263 (2020).
78. Zhou, N. Shield-dried soil prepared as a highly active admixture. *Ceram. Silik.* https://doi.org/10.13168/cs.2024.0051 (2024).
79. Kahilu, G. M., Bada, S. & Mulopo, J. Physicochemical, structural analysis of coal discards (and sewage sludge) (co)-HTC derived biochar for a sustainable carbon economy and evaluation of the liquid by-product. *Sci. Rep.* https://doi.org/10.1038/s41598-022-22528-y (2022).
80. Tian, Z. et al. Ultrasonication-assisted controllable self-assembly of graphene oxide. *J. Nanosci. Nanotechnol.* **15**, 2015. https://doi.org/10.1166/jnn.2015.10276 (2014).
81. Mohammedture, M. et al. Impact of probe sonication and sulfuric acid pretreatment on graphene exfoliation in water. *Sci. Rep.* https://doi.org/10.1038/s41598-023-45874-x (2023).
82. Abedi, M., Fangueiro, R., Camões, A. & Correia, A. G. Evaluation of CNT/GNP's synergic effects on the mechanical, microstructural, and durability properties of a cementitious composite by the novel dispersion method. *Constr. Build. Mater.* **260**, 120486. https://doi.org/10.1016/j.conbuildmat.2020.120486 (2020).
83. Abedi, M., Fangueiro, R. & Correia, A. G. An effective method for hybrid CNT/GNP dispersion and its effects on the mechanical, microstructural, thermal, and electrical properties of multifunctional cementitious composites. *J. Nanomater.* **2020**, 1. https://doi.org/10.1155/2020/6749150 (2020).
84. Wan, L. et al. Graphene nanosheets based on controlled exfoliation process for enhanced lithium storage in lithium-ion battery. *Diam. Relat. Mater.* **20**, 756. https://doi.org/10.1016/j.diamond.2011.03.027 (2011).
85. Ding, J., Zhao, H. & Yu, H. A water-based green approach to large-scale production of aqueous compatible graphene nanoplatelets. *Sci. Rep.* https://doi.org/10.1038/s41598-018-23859-5 (2018).
86. de Souza, F. B., Shamsaei, E., Chen, S.-J., Sagoe-Crentsil, K. & Duan, W. Controlled growth and ordering of poorly-crystalline calcium-silicate-hydrate nanosheets. *Commun. Mater.* https://doi.org/10.1038/s43246-021-00191-6 (2021).
87. Jafer, H., Atherton, W., Sadique, M., Ruddock, F. & Loffill, E. Development of a new ternary blended cementitious binder produced from waste materials for use in soft soil stabilisation. *J. Clean. Prod.* **172**, 516. https://doi.org/10.1016/j.jclepro.2017.10.233 (2017).
88. Lu, D., Wang, Y., Leng, Z. & Zhong, J. Influence of ternary blended cementitious fillers in a cold mix asphalt mixture. *J. Clean. Prod.* **318**, 128421. https://doi.org/10.1016/j.jclepro.2021.128421 (2021).
89. Dũng, N. T., Hooper, T. J. N. & Unluer, C. Enhancing the performance of MgO-activated slag-fly ash mixes by accelerated carbonation. *J. CO2 Util.* **42**, 101356. https://doi.org/10.1016/j.jcou.2020.101356 (2020).
90. Benavente, C. et al. The influence of graphene oxide on the performance of concrete: A quantitative analysis of mechanical and microstructural properties. *Buildings* **15**, 1082. https://doi.org/10.3390/buildings15071082 (2025).
91. Vallurupalli, K., Meng, W., Liu, J. & Khayat, K. H. Effect of graphene oxide on rheology, hydration and strength development of cement paste. *Constr. Build. Mater.* **265**, 120311. https://doi.org/10.1016/j.conbuildmat.2020.120311 (2020).

92. Afarani, H. T., Carroll, W. R., Garboczi, E. J. & Biernacki, J. J. Designing 3D printable cementitious materials with gel-forming polymers. *Constr. Build. Mater.* **268**, 121709. https://doi.org/10.1016/j.conbuildmat.2020.121709 (2020).
93. Taborda-Barraza, M., Padilha, F., Silvestro, L., de Azevedo, A. R. G. & Gleize, P. J. P. Evaluation of CNTs and SiC whiskers effect on the rheology and mechanical performance of metakaolin-based geopolymers. *Materials* **15**, 6099. https://doi.org/10.3390/ma15176099 (2022).
94. Ioannou, S., Chowdhury, M. S. & Badr, A. Rheological, hydration and mechanical characteristics of microsilica fibre reinforced cement combinations with incremental fly ash contents. *Constr. Build. Mater.* **191**, 423. https://doi.org/10.1016/j.conbuildmat.2018.10.039 (2018).
95. Nguyen, H. D., Zhang, Q., Sagoe-Crentsil, K. & Duan, W. Graphene oxide-coated sand for improving performance of cement composites. *Cem. Concr. Compos.* **124**, 104279. https://doi.org/10.1016/j.cemconcomp.2021.104279 (2021).
96. Huang, B. et al. Influence of sugar beetroot microsheets on the hydration kinetics of cementitious composites: Electrochemical characterization. *Cem. Concr. Compos.* **144**, 105314. https://doi.org/10.1016/j.cemconcomp.2023.105314 (2023).
97. Stephens, C. S., Brown, L. & Sanchez, F. Quantification of the re-agglomeration of carbon nanofiber aqueous dispersion in cement pastes and effect on the early age flexural response. *Carbon* **107**, 482. https://doi.org/10.1016/j.carbon.2016.05.076 (2016).
98. Paul, S. C., van Zijl, G. & Šavija, B. Effect of fibers on durability of concrete: A practical review. *Materials* **13**, 4562. https://doi.org/10.3390/ma13204562 (2020).
99. Wang, M. & Yao, H. A novel organic–inorganic hybrid admixture for increasing flowability and reducing viscosity of ultra-high performance paste. *Materials* **13**, 3385. https://doi.org/10.3390/ma13153385 (2020).
100. Ebert, B. L., Kirkelund, G. M., Steenari, B., Geiker, M. R. Valorization of MSWI fly ash for use in cement-based materials, research portal denmark (2021) 280. Retrieved Aug 2025. https://local.forskningsportal.dk/local/dki-cgi/ws/cris-link?src=dtu&id=dtu-72c4b803-6837-4a27-83d7-736bcd15bae3&ti=Valorization%20of%20MSWI%20Fly%20Ash%20for%20Use%20in%20Cement-Based%20Materials
101. Tang, Z., Litina, C. & Al-Tabbaa, A. Optimisation of rheological parameters and mechanical properties of engineered cementitious composites (ECC) using regression-based models. *Constr. Build. Mater.* **310**, 125281. https://doi.org/10.1016/j.conbuildmat.2021.125281 (2021).
102. Sonebi, M., Abdalqader, A., Fayyad, T. M., Perrot, A. & Bai, Y. Optimisation of rheological parameters, induced bleeding, permeability and mechanical properties of supersulfated cement grouts. *Constr. Build. Mater.* **262**, 120078. https://doi.org/10.1016/j.conbuildmat.2020.120078 (2020).
103. Ortiz, J. A., de la Fuente, A., Sebastiá, F. M., Segura, I. & Aguado, A. Steel-fibre-reinforced self-compacting concrete with 100% recycled mixed aggregates suitable for structural applications. *Constr. Build. Mater.* **156**, 230. https://doi.org/10.1016/j.conbuildmat.2017.08.188 (2017).
104. Coppola, L., Coffetti, D., Crotti, E. & Pastore, T. CSA-based Portland-free binders to manufacture sustainable concretes for jointless slabs on ground. *Constr. Build. Mater.* **187**, 691. https://doi.org/10.1016/j.conbuildmat.2018.07.221 (2018).
105. Cho, S., van Rooyen, A., Kearsley, E. P. & van Zijl, G. Foam stability of 3D printable foamed concrete. *J. Build. Eng.* **47**, 103884. https://doi.org/10.1016/j.jobe.2021.103884 (2021).
106. Li, D., Xu, G., Deng, W., He, L. & Hu, Y. The influence of mineral powder dosage on the mechanical properties and microstructure of self-compacting concrete. *J. Compos. Sci.* **9**, 258. https://doi.org/10.3390/jcs9060258 (2025).
107. Revilla-Cuesta, V., Manso-Morato, J., Hurtado-Alonso, N., Skaf, M. & Ortega-López, V. Mechanical and environmental advantages of the revaluation of raw-crushed wind-turbine blades as a concrete component. *J. Build. Eng.* **82**, 108383. https://doi.org/10.1016/j.jobe.2023.108383 (2023).
108. Revilla-Cuesta, V., Hurtado-Alonso, N., Manso-Morato, J., Serrano-López, R. & Manso, J. M. Effects of temperature and moisture fluctuations for suitable use of raw-crushed wind-turbine blade in concrete. *Environ. Sci. Pollut. Res.* **31**, 37757. https://doi.org/10.1007/s11356-024-33720-0 (2024).
109. Bhojaraju, C., Mare, M. D. & Ouellet-Plamondon, C. The impact of carbon-based nanomaterial additions on the hydration reactions and kinetics of GGBS-modified cements. *Constr. Build. Mater.* **303**, 124366. https://doi.org/10.1016/j.conbuildmat.2021.124366 (2021).
110. Snehal, K., Das, B. B. & Matta, A. Early age, hydration, mechanical and microstructure properties of nano-silica blended cementitious composites. *Constr. Build. Mater.* **233**, 117212. https://doi.org/10.1016/j.conbuildmat.2019.117212 (2019).
111. Lavergne, F., Belhadi, R., Carriat, J. & Fraj, A. B. Effect of nano-silica particles on the hydration, the rheology and the strength development of a blended cement paste. *Cem. Concr. Compos.* **95**, 42. https://doi.org/10.1016/j.cemconcomp.2018.10.007 (2018).
112. Mashaly, A. A., Mahdy, M. G. & Elemam, W. E. Optimal design and characteristics of sustainable eco-friendly ultra-high-performance concrete. *Innov. Infrastruct. Solut.* https://doi.org/10.1007/s41062-023-01277-5 (2023).
113. Naqi, A., Delsaute, B., Königsberger, M. & Staquet, S. Monitoring early age elastic and viscoelastic properties of alkali-activated slag mortar by means of repeated minute-long loadings. *Dev. Built Environ.* **16**, 100275. https://doi.org/10.1016/j.dibe.2023.100275 (2023).
114. D'Alessandro, A. et al. Self-sensing properties of green alkali-activated binders with carbon-based nanoinclusions. *Sustainability* **12**, 9916. https://doi.org/10.3390/su12239916 (2020).
115. Ma, L., Cheng, Z., Zeng, Q. & Li, B. Experimental investigation on the mechanical properties of geopolymer recycled aggregate concrete reinforced with steel-polypropylene hybrid fiber. *Buildings* **15**, 1723. https://doi.org/10.3390/buildings15101723 (2025).
116. Nassiri, S. et al. Comparison of unique effects of two contrasting types of cellulose nanomaterials on setting time, rheology, and compressive strength of cement paste. *Cem. Concr. Compos.* **123**, 104201. https://doi.org/10.1016/j.cemconcomp.2021.104201 (2021).
117. Hogancamp, J. & Grasley, Z. Dispersion of high concentrations of carbon nanofibers in Portland cement mortars. *J. Nanomater.* **2017**, 1. https://doi.org/10.1155/2017/9375293 (2017).
118. Muñoz-Ferreiro, C. et al. Microstructure, interfaces and properties of 3YTZP ceramic composites with 10 and 20 vol% different graphene-based nanostructures as fillers. *J. Alloys Compd.* **777**, 213. https://doi.org/10.1016/j.jallcom.2018.10.336 (2018).
119. Yeung, J. S. K., Yam, M. C. H. & Wong, Y. L. 1-Year development trend of concrete compressive strength using Calcium Sulfoaluminate cement blended with OPC, PFA and GGBS. *Constr. Build. Mater.* **198**, 527. https://doi.org/10.1016/j.conbuildmat.2018.11.182 (2018).
120. Thapa, V. B., Waldmann, D. & Simon, C. Gravel wash mud, a quarry waste material as supplementary cementitious material (SCM). *Cem. Concr. Res.* **124**, 105833. https://doi.org/10.1016/j.cemconres.2019.105833 (2019).
121. Dũng, N. T., Hooper, T. J. N. & Unluer, C. Improving the carbonation resistance of Na_2CO_3-activated slag mixes via the use of reactive MgO and nucleation seeding. *Cem. Concr. Compos.* **115**, 103832. https://doi.org/10.1016/j.cemconcomp.2020.103832 (2020).
122. Pizoń, J., Konečný, P., Mynarz, M. & Bílek, V. Properties of fine graded perlite-based lightweight cement mortars subjected to elevated temperatures. *Buildings* **13**, 2969. https://doi.org/10.3390/buildings13122969 (2023).
123. Kushnir, A. et al. The fire resistance of high-strength concrete containing natural zeolites. *Cem. Concr. Compos.* **116**, 103897. https://doi.org/10.1016/j.cemconcomp.2020.103897 (2020).
124. Li, C. et al. Understanding the sulfate attack of Portland cement–based materials exposed to applied electric fields: Mineralogical alteration and migration behavior of ionic species. *Cem. Concr. Compos.* **111**, 103630. https://doi.org/10.1016/j.cemconcomp.2020.103630 (2020).

125. Adu-Amankwah, S. et al. Combined influence of carbonation and leaching on freeze-thaw resistance of limestone ternary cement concrete. *Constr. Build. Mater.* **307**, 125087. https://doi.org/10.1016/j.conbuildmat.2021.125087 (2021).
126. Matar, P. & Barhoun, J. Effects of waterproofing admixture on the compressive strength and permeability of recycled aggregate concrete. *J. Build. Eng.* **32**, 101521. https://doi.org/10.1016/j.jobe.2020.101521 (2020).
127. Sambucci, M., Nouri, S. M., Tayebi, S. T. & Valente, M. Synergic effect of recycled carbon fibers and microfibrillated cellulose gel for enhancing the mechanical properties of cement-based materials. *Gels* **9**, 981. https://doi.org/10.3390/gels9120981 (2023).
128. Nalon, G. H. et al. Residual mechanical properties of mortars containing carbon nanomaterials exposed to high temperatures. *Constr. Build. Mater.* **275**, 122123. https://doi.org/10.1016/j.conbuildmat.2020.122123 (2021).
129. Muthu, M., Yang, E. & Unluer, C. Effect of graphene oxide on the deterioration of cement pastes exposed to citric and sulfuric acids. *Cement Concr. Compos.* **124**, 104252. https://doi.org/10.1016/j.cemconcomp.2021.104252 (2021).
130. Jiang, Y., Sun, M., Gao, X. & Yang, Y. Mechanistic insights into graphene oxide-induced early hydration and curing optimization in cementitious materials. *Constr. Build. Mater.* **495**, 143741. https://doi.org/10.1016/j.conbuildmat.2025.143741 (2025).
131. Wang, J., Jin, T., Li, L., Zhou, C. & Zeng, Q. Thinner fillers, coarser pores? A comparative study of the pore structure alterations of cement composites by graphene oxides and graphene nanoplatelets. *Compos. Part A Appl. Sci. Manuf.* **130**, 105750. https://doi.org/10.1016/j.compositesa.2019.105750 (2019).
132. Tong, T. et al. Investigation of the effects of graphene and graphene oxide nanoplatelets on the micro- and macro-properties of cementitious materials. *Constr. Build. Mater.* **106**, 102. https://doi.org/10.1016/j.conbuildmat.2015.12.092 (2015).
133. Wang, Q. et al. The influence of the addition of multi-scale zirconia on the properties of ultra-high-performance concretes. *Buildings* **15**, 1207. https://doi.org/10.3390/buildings15071207 (2025).
134. Ozersky, A., Khomyakov, A. K. & Peterson, K. Novel ultra high performance concrete mixing technology with preliminary dry forced packing. *Constr. Build. Mater.* **267**, 120934. https://doi.org/10.1016/j.conbuildmat.2020.120934 (2020).
135. Paredes, J., Gálvez, J. C., Enfedaque, A. & Alberti, M. G. Matrix optimization of ultra high performance concrete for improving strength and durability. *Materials* **14**, 6944. https://doi.org/10.3390/ma14226944 (2021).
136. García-Lodeiro, I. et al. Studying the dosage-dependent influence of hydrophobic alkoxysilane/siloxane admixtures on the performance of repair micromortars. *J. Build. Eng.* **48**, 103905. https://doi.org/10.1016/j.jobe.2021.103905 (2021).
137. Dhandapani, Y. et al. Performance of cementitious systems containing calcined clay in a chloride-rich environment: A review by TC-282 CCL. *Mater. Struct.* https://doi.org/10.1617/s11527-024-02426-7 (2024).
138. Gopalakrishnan, R. & Jeyalakshmi, R. The effects on durability and mechanical properties of multiple nano and micro additive OPC mortar exposed to combined chloride and sulfate attack. *Mater. Sci. Semicond. Process.* **106**, 104772. https://doi.org/10.1016/j.mssp.2019.104772 (2019).
139. Miah, M. J., Huaping, R., Paul, S. C., Babafemi, A. J. & Li, Y. Long-term strength and durability performance of eco-friendly concrete with supplementary cementitious materials. *Innov. Infrast. Solut.* https://doi.org/10.1007/s41062-023-01225-3 (2023).
140. Mohsen, M. O. et al. Fly ash and natural pozzolana impacts on sustainable concrete permeability and mechanical properties. *Buildings* **13**, 1927. https://doi.org/10.3390/buildings13081927 (2023).
141. Banerjee, P., Raj, R., Kumar, S. & Bose, S. Tuneable chemistry at the interface and self-healing towards improving structural properties of carbon fiber laminates: A critical review. *Nanosc. Adv.* **3**, 5745. https://doi.org/10.1039/d1na00294e (2021).
142. Yao, X., Kinloch, I. A. & Bissett, M. A. Fabrication and mechanical performance of Graphene Nanoplatelet/glass fiber reinforced polymer hybrid composites. *Front. Mater.* https://doi.org/10.3389/fmats.2021.773343 (2021).
143. Guo, Y. et al. Evaluating the chloride diffusion coefficient of cement mortars based on the tortuosity of pore structurally-designed cement pastes. *Micropor. Mesopor. Mater.* **317**, 111018. https://doi.org/10.1016/j.micromeso.2021.111018 (2021).
144. Yu, J., Li, M. & Jin, Z. Exploration of saturated transport of ion concentration differences in C–S–H channels. *Mater. Struct.* https://doi.org/10.1617/s11527-023-02272-z (2023).
145. Zhang, Y., Yang, Z. & Ye, G. Dependence of unsaturated chloride diffusion on the pore structure in cementitious materials. *Cem. Concr. Res.* **127**, 105919. https://doi.org/10.1016/j.cemconres.2019.105919 (2019).
146. Xiaoting, C., Caratini, G., Davy, C., Troadec, D. & Skoczylas, F. Coupled transport and poro-mechanical properties of a heat-treated mortar under confinement. *Cem. Concr. Res.* **49**, 10. https://doi.org/10.1016/j.cemconres.2013.03.006 (2013).
147. Devi, K., Saini, B. & Aggarwal, P. Impact of high temperature on mortar mixes containing additives. *J. Eng. Res.* https://doi.org/10.36909/jer.10477 (2021).
148. Kumar, S. et al. Effect of graphene oxide on mechanical, deformation and drying shrinkage properties of concrete reinforced with fly ash as cementitious material by using RSM modelling. *Sci. Rep.* https://doi.org/10.1038/s41598-024-69601-2 (2024).
149. Advincula, P. A. et al. Flash graphene from rubber waste. *Carbon* **178**, 649. https://doi.org/10.1016/j.carbon.2021.03.020 (2021).
150. Abdulfattah, O. et al. Experimental evaluation of using pyrolyzed carbon black derived from waste tires as additive towards sustainable concrete. *Case Stud. Constr. Mater.* **16**, e00938. https://doi.org/10.1016/j.cscm.2022.e00938 (2022).
151. Wang, X. & Petrů, M. Degradation of bending properties of flax fiber reinforced polymer after natural aging and accelerated aging. *Constr. Build. Mater.* **240**, 117909. https://doi.org/10.1016/j.conbuildmat.2019.117909 (2020).
152. Klyuev, S. et al. Fine-grained concrete properties in depending on carbon black additive introducing methods. *J. Market. Res.* **32**, 1996. https://doi.org/10.1016/j.jmrt.2024.08.052 (2024).
153. Ramana, I. & Parthasarathi, N. Synergistic effects of fly ash and graphene oxide composites at high temperatures and prediction using ANN and RSM approach. *Sci. Rep.* https://doi.org/10.1038/s41598-024-83778-6 (2025).
154. Liu, D., Zepper, J. C. O., Yuan, B., Chen, Y. & Yu, Q. Self-cleaning performance of autoclaved photocatalytic cement pastes: Insights into phase composition, microstructure and aluminum incorporation in C-S–H. *Ceram. Int.* **50**, 5835. https://doi.org/10.1016/j.ceramint.2023.11.394 (2023).
155. Bae, S. et al. Soft X-ray ptychographic imaging and morphological quantification of calcium silicate hydrates (C–S–H). *J. Am. Ceram. Soc.* **98**, 4090. https://doi.org/10.1111/jace.13808 (2015).
156. Sadok, A. H. & Courard, L. Chloride diffusion and oxygen permeability of mortars with low active blast furnace slag. *Constr. Build. Mater.* **181**, 319. https://doi.org/10.1016/j.conbuildmat.2018.06.036 (2018).
157. Abdellatief, M., Alanazi, H., Radwan, M. K. H. & Tahwia, A. M. Multiscale characterization at early ages of ultra-high performance geopolymer concrete. *Polymers* **14**, 5504. https://doi.org/10.3390/polym14245504 (2022).
158. da S. Andrade, D., da S. Rêgo, J. H., Morais, P. C., de M. Lopes, A. N. & Frías, M. Investigation of C-S-H in ternary cement pastes containing nanosilica and highly-reactive supplementary cementitious materials (SCMs): Microstructure and strength. *Constr. Build. Mater.* **198**, 445. https://doi.org/10.1016/j.conbuildmat.2018.10.235 (2018).
159. Calvo, J. L. G. et al. Expansive concretes with photocatalytic activity for pavements: Enhanced performance and modifications of the expansive hydrates composition. *Constr. Build. Mater.* **218**, 394. https://doi.org/10.1016/j.conbuildmat.2019.05.135 (2019).
160. Wyrzykowski, M., Assmann, A., Hesse, C. & Lura, P. Microstructure development and autogenous shrinkage of mortars with C-S-H seeding and internal curing. *Cem. Concr. Res.* **129**, 105967. https://doi.org/10.1016/j.cemconres.2019.105967 (2020).
161. Zhou, H. et al. Effect of nano C-A–S–H seeds on the early-stage hydration and pore structure of Portland cement pastes. *Adv. Cem. Res.* **33**, 295. https://doi.org/10.1680/jadcr.19.00134 (2020).
162. Sharma, A. et al. Characterization of paste microstructure for durability properties of concrete. *Constr. Build. Mater.* **248**, 118570. https://doi.org/10.1016/j.conbuildmat.2020.118570 (2020).
163. Fernandez-Sanchez, J. et al. Mix and measure II: Joint high-energy laboratory powder diffraction and microtomography for cement hydration studies. *J. Appl. Crystallogr.* **57**, 1067. https://doi.org/10.1107/s1600576724004527 (2024).

164. Moshiri, A. et al. Structure and morphology of calcium-silicate-hydrates cross-linked with dipodal organosilanes. *Cem. Concr. Res.* **133**, 106076. https://doi.org/10.1016/j.cemconres.2020.106076 (2020).
165. Cui, K., Chang, J., Sabri, M. M. S. & Huang, J. Study of dispersion, hydration, and microstructure of graphene nanoplates-modified sulfoaluminate cement paste. *Nanomaterials* **12**, 2708. https://doi.org/10.3390/nano12152708 (2022).
166. Li, L. et al. Relationships between microstructure and transport properties in mortar containing recycled ceramic powder. *J. Clean. Prod.* **263**, 121384. https://doi.org/10.1016/j.jclepro.2020.121384 (2020).
167. Bilgil, A., Şimşek, O., Sevim, Ö. & Demîr, İ. Development of lightweight and thermally efficient clay bricks using expansion additives: Effects of firing temperature and additive ratios on physicomechanical properties. *J. Aust. Ceram. Soc.* https://doi.org/10.1007/s41779-025-01170-7 (2025).
168. Cristelo, N. et al. Development of highly porous alkaline cements from industrial waste for thermal insulation of building envelops. *Constr. Build. Mater.* **409**, 134068. https://doi.org/10.1016/j.conbuildmat.2023.134068 (2023).
169. Maraghechi, H., Avet, F., Wong, H. S., Kamyab, H. & Scrivener, K. Performance of Limestone Calcined Clay Cement (LC3) with various kaolinite contents with respect to chloride transport. *Mater. Struct.* https://doi.org/10.1617/s11527-018-1255-3 (2018).
170. Mousavinezhad, S., Garcia, J. M., Toledo, W. K. & Newtson, C. M. A locally available natural pozzolan as a supplementary cementitious material in Portland cement concrete. *Buildings* **13**, 2364. https://doi.org/10.3390/buildings13092364 (2023).
171. Alzaza, A., Ohenoja, K. & Illikainen, M. Improved strength development and frost resistance of Portland cement ground-granulated blast furnace slag binary binder cured at 0 °C with the addition of calcium silicate hydrate seeds. *J. Build. Eng.* **48**, 103904. https://doi.org/10.1016/j.jobe.2021.103904 (2021).
172. Abdelzaher, M. A., Farghali, A. A. & Hamouda, A. S. Effective impact of nano-plastic-waste incorporated with nanotitina on the physical, mechanical and microstructural properties of white cement pastes composites for progressing towards sustainability. *Sci. Rep.* https://doi.org/10.1038/s41598-024-62661-4 (2024).
173. Faridmehr, I., Azarsa, M., Varjavand, I. & Valerievich, K. A. Artificial intelligence-driven optimization of ready-mix concrete for enhanced strength, cost efficiency, and carbon dioxide emission reduction. *Res. Square* https://doi.org/10.21203/rs.3.rs-4817801/v1 (2024).
174. Onn, C. C. et al. Strength, carbon footprint and cost considerations of mortar blends with high volume ground granulated blast furnace slag. *Sustainability* **11**, 7194. https://doi.org/10.3390/su11247194 (2019).
175. Stelte, W., Reddy, N., Barsberg, S. & Sanadi, A. R. Coir from coconut processing waste as a raw material for applications beyond traditional uses. *BioResources* https://doi.org/10.15376/biores.18.1.stelte (2022).
176. Amirtharaj, J. Strength enhancement of concrete using coir fiber. *Int. J. Res. Appl. Sci. Eng. Technol.* **7**, 1176. https://doi.org/10.22214/ijraset.2019.4210 (2019).
177. Kumaraswamy, G. et al. Coir fibre-reinforced concrete for enhanced compressive strength and sustainability in construction applications. *Heliyon* https://doi.org/10.1016/j.heliyon.2024.e39773 (2024).
178. Bhat, K. M. U. D. & Khan, M. Z. Effect of steel fibre reinforcement on early strength of concrete. *Int. J. Trend Sci. Res. Dev.* https://doi.org/10.31142/ijtsrd15781 (2018).
179. Zhao, W., Liu, Z. & Wang, R. Effect of fibers on the mechanical properties and mechanism of cast-in-situ foamed concrete. *Adv. Mater. Sci. Eng.* **2022**, 1. https://doi.org/10.1155/2022/2238187 (2022).
180. Záleská, M. et al. MOC doped with graphene nanoplatelets: The influence of the mixture preparation technology on its properties. *Materials* **14**, 1450. https://doi.org/10.3390/ma14061450 (2021).
181. Chen, Y. et al. Improvement of flexural and compressive strength of cement mortar by graphene nanoplatelets. *Open Civ. Eng. J.* **15**, 165. https://doi.org/10.2174/1874149502115010165 (2021).
182. Tariq, H. et al. Mechanical performance of polymeric ARGF-based fly ash-concrete composites: A study for eco-friendly circular economy application. *Polymers* **14**, 1774. https://doi.org/10.3390/polym14091774 (2022).
183. Mouawad, F., Homsi, F., Geara, F. & Mina, R. Predicting compressive strength of sustainable concrete using machine learning and artificial neural networks. *Constr. Mater.* **5**, 56. https://doi.org/10.3390/constrmater5030056 (2025).
184. Al-Naghi, A. A. A., Ahmad, A., Amin, M. N., Algassem, O. & Alnawmasi, N. Sustainable optimisation of GGBS-based concrete: De-risking mix design through predictive machine learning models. *Case Stud. Constr. Mater.* https://doi.org/10.1016/j.cscm.2025.e04900 (2025).
185. Hasan, M. R., Shuvo, A. K., Pranto, E. B., Hasan, M. & Miah, M. M. Data-driven prediction of concrete strength by machine learning: Hybrid-fiber-reinforced recycled aggregate concrete. *World J. Eng.* https://doi.org/10.1108/wje-01-2025-0038 (2025).
186. Çakıroğlu, C., Ahadian, F., Bekdaş, G. & Geem, Z. W. Tensile strength predictive modeling of natural-fiber-reinforced recycled aggregate concrete using explainable gradient boosting models. *J. Compos. Sci.* **9**, 119. https://doi.org/10.3390/jcs9030119 (2025).
187. Gu, Y. et al. Multi-objective optimization for nano-silica-modified concrete based on explainable machine learning. *Nanomaterials* **15**, 1423. https://doi.org/10.3390/nano15181423 (2025).
188. Wu, S., Liu, X. H. & Fu, B. Explainable automl and multi-objective optimization for sustainable high-performance geopolymer concrete. *Sci. Rep.* https://doi.org/10.1038/s41598-025-18666-8 (2025).
189. Wang, M. et al. Multi-objective optimization of ultra-high performance concrete based on life-cycle assessment and machine learning methods. *Front. Struct. Civ. Eng.* https://doi.org/10.1007/s11709-025-1152-0 (2025).

Author contributions

P.A: Conceptualization, Methodology, Writing, Original draft, Review and Editing, Data Curation; S.D.S: Review and Editing; S.P: Data Curation, Supervision, Review and Editing; P.A: Review and Editing; F.B: Review and Editing.

Declarations

Competing interests

The authors declare no competing interests.

Ethical approval

This work did not involve human participants or animals; hence, ethical approval was not required.

Additional information

Correspondence and requests for materials should be addressed to S.P. or F.B.

Reprints and permissions information is available at www.nature.com/reprints.

Publisher's note Springer Nature remains neutral with regard to jurisdictional claims in published maps and institutional affiliations.